Titre: Title:	Numerical Modelling of Gas-Phase Turbulent Combustion Phenomena from Li-Ion Battery Module Undergoing Thermal Runaway
Auteur: Author:	Arona Sottas
Date:	2025
Type:	Mémoire ou thèse / Dissertation or Thesis
Référence: Citation:	Sottas, A. (2025). Numerical Modelling of Gas-Phase Turbulent Combustion Phenomena from Li-Ion Battery Module Undergoing Thermal Runaway [Mémoire de maîtrise, Polytechnique Montréal]. PolyPublie. https://publications.polymtl.ca/65703/

POLYTECHNIQUE MONTRÉAL
affiliée à l'Université de Montréal

Numerical Modelling of Gas-Phase Turbulent Combustion Phenomena from Li-Ion Battery Module Undergoing Thermal Runaway

ARONA SOTTAS
Département de génie mécanique

Mémoire présenté en vue de l'obtention du diplôme de *Maîtrise ès sciences appliquées*
Génie aérospatial

Mai 2025

POLYTECHNIQUE MONTRÉAL
affiliée à l'Université de Montréal

Ce mémoire intitulé :

Numerical Modelling of Gas-Phase Turbulent Combustion Phenomena from Li-Ion Battery Module Undergoing Thermal Runaway

présenté par **Arona SOTTAS**
en vue de l'obtention du diplôme de *Maîtrise ès sciences appliquées*
a été dûment accepté par le jury d'examen constitué de :

Fabian DENNER, président
Étienne ROBERT, membre et directeur de recherche
Bruno SAVARD, membre et codirecteur de recherche
Roberto PAOLI, membre

DEDICATION

À Kyra, mes parents et mes grands-parents,

ACKNOWLEDGEMENTS

I would like to express my deepest gratitude to my two research directors, Professors Étienne Robert and Bruno Savard. Your continuous support and advices throughout the research project were kindly appreciated. Your regular feedback on my results enabled me to make progress and present the best of my work. Thank you for the various cohesion activities proposed for the research laboratory over these two years.

I would like to sincerely thank Dr. Philippe Versailles for his availability, patience in answering my questions and his valuable guidance in numerical modelling throughout the research project.

I am so grateful to Blue Solutions Canada for making this research project possible, especially to Sébastien Geoffroy for his constructive help with the geometry used at our regular meetings. I also express my gratitude for financial support from the Ministry of the Economy, Innovation and Energy (INNOVÉÉ Program) and the Natural Science and Engineering Research Council of Canada (Alliance Program).

I would also like to thank all the members of the FriBaCo research team: Mathieu, Marc-André, Marie-Laure, Nammuni and Alexis, with whom we were able to exchange ideas and support each other throughout the project. I would like to thank them for their hard work, which would not have been possible without them. Special thanks to Marc-André, it was always a nice surprise to see how the Li-ion batteries exploded.

I would also like to thank all my LeMuR labmates who supported me throughout this research project: Olivier J., Mathieu CP, William, Xavier, Luisa, Marie-Laure, Gabriel, Martin, Marc-André, Alexis, Olivier C., Zisen, Gabriel, Lucas, Taylor, Frédéric and François. Thank you again for your passionate exchanges and your availability during coffee breaks in the laboratory. I hope to see you again to continue our discussions.

My thanks also go to my roommates and harpists, Kyra and Juliette, for encouraging me to pursue my scientific research project and a musicology master at UdeM at the same time. Thank you for your generosity and patience over the last two years. It has been a pleasure to be able to share the Montreal adventure in music during concerts over these two years. I would also like to thank all those who supported me at the Montreal Conservatory and the Faculty of Music (Amandine, Adélaide, Paul, Laurence, Kévin, Émilie, Anais, Simon, Sacha, Joseph, Daniel) for your warm welcome, your kindness and your constant availability.

A warm thank you to my parents and my grandparents for their endless support and their regular monitoring of my progress during the two years I've spent on the other side of the Atlantic.

Résumé

La prévention du risque d'emballement thermique par les batteries Li-ion est un enjeu de sécurité actuel avec l'essor des transports électriques. Le phénomène d'emballement thermique entraîne une libération par la cellule d'une quantité de chaleur significative résultant des réactions chimiques internes. La cellule éjecte alors un mélange turbulent de gaz et de particules toxiques et inflammables au contact de l'air créant ainsi un risque d'incendie majeur. Une analyse en profondeur de ce phénomène notamment des conditions d'allumage du mélange gazeux émis par la cellule est menée. Pour ce projet de recherche, la géométrie étudiée consiste en un module de batterie.

Dans ce mémoire, trois modèles de combustion (Eddy Dissipation Concept, Non Premixed Combustion et Partially Premixed Combustion) sont comparés sur le solveur commercial ANSYS Fluent. Une méthodologie de modélisation numérique est développée pour chaque modèle en couplant la phase de venting, la turbulence et les réactions de combustion en phase gazeuse. Différents outils, comme la moyenne de température axiale extérieure, sont employés pour étudier les conditions d'allumage du mélange émis par la cellule. Les modèles Non Premixed Combustion (NPC) et Partially Premixed Combustion (PPC) permettent d'étudier la région d'allumage sans pouvoir prédire un délai d'auto-allumage pour chaque température de mélange. Le modèle Eddy Dissipation Concept (EDC) permet également d'étudier la région d'allumage tout en permettant une estimation du délai d'auto-allumage du mélange. En termes de performance de calculs, les modèles NPC et PPC permettent de réduire les coûts comparés au modèle EDC. Cette comparaison est poursuivie par une analyse de sensibilité réalisée sur le modèle EDC afin d'observer l'effet de quelques paramètres d'influence sur les conditions d'auto-allumage du mélange gazeux. Une pression d'ouverture de l'évent plus élevée (50 PSI) a un faible impact sur les conditions d'auto-allumage, tandis que le nombre de sources de dégazage dans le module a une influence significative sur les conditions d'auto-inflammation du mélange empêchant la stabilisation de la région d'allumage dans le domaine

Abstract

Preventing the risk of thermal runaway from Li-ion batteries is a current safety issue with the rapid expansion of electric transport. Thermal runaway results in the release by the cell of a significant amount of heat resulting from internal chemical reactions. The cell then ejects a turbulent mixture of flammable and toxic gases and particles into the air, thus creating a major fire hazard. An in-depth analysis of this phenomenon, and in particular of the ignition conditions for the gas mixture emitted by the cell is presented. For this research project, the geometry studied consists of a battery module containing solid electrolyte cells.

In this thesis, three combustion models (Eddy Dissipation Concept (EDC), Non Premixed Combustion (NPC) and Partially Premixed Combustion (PPC)) are compared on the ANSYS Fluent commercial solver. A modelling methodology is developed for each model, coupling the venting phase, turbulence, and combustion reactions in the gas phase. Different techniques, including the analysis of mean axial temperature, are used to study the ignition conditions of the mixture emitted by the cell. The Non Premixed Combustion and Partially Premixed Combustion models can be used to study the ignition region without being able to predict an auto-ignition delay for each mixture temperature. The Eddy Dissipation Concept model can also be used to study the ignition region while providing an estimation of the mixture auto-ignition delay. In terms of calculation performance, the NPC and PPC models reduce costs compared with the EDC model. This comparison is followed by a sensitivity analysis of one of the numerical models in order to identify some of the parameters influencing the auto-ignition conditions of a gas mixture. Higher vent opening pressure (50 PSI) minimally impacts auto-ignition conditions, while the number of degassing sources within the module has a more significant influence on the mixture's auto-ignition conditions preventing stabilisation of the ignition region.

TABLE OF CONTENTS

LIST OF TABLES

LIST OF FIGURES

LIST OF SYMBOLS AND ACRONYMS

CAD	Computer-Aided Design
CFD	Computational Fluid Dynamics
EDC	Eddy Dissipation Concept
EV	Electric Vehicle
DNS	Direct Numerical Simulation
FAA	Federal Aviation Administration
HRR	Heat Release Rate
ISAT	In-Situ Adaptative Tabulation
K	SI Unit of temperature (Kelvins)
Li-ion	Lithium-ion
LIB	Lithium-ion Battery
LiM-SSB	Lithium Metal - Solid State Battery
LES	Large Eddy Simulation
LFP	Lithium Iron Phosphate
LMP	Lithium Metal Polymer
LCO	Lithium Cobalt Oxide
LMO	Lithium Manganese
Ma	Mach number
NCA	Nickel Cobalt Aluminium
NMC	Nickel Manganese Cobalt
NPC	Non Premixed Combustion
ODE	Ordinary Differential Equation
Pa	SI Unit of pressure (Pascal)
PDF	Probability Density Function
PE	Polyethylene
PPC	Partially Premixed Combustion
PSI	Unit of pressure (Pound per Square Inch)
RANS	Reynold Averaged Navier-Stokes
SOC	State Of Charge
TCI	Turbulence-Chemistry Interaction
TR	Thermal Runaway
TSS	Time Step Size

LIST OF APPENDICES

CHAPTER 1 INTRODUCTION

With the goal of mitigating climate change and reducing the dependence to fossil fuels, innovation in the transportation sector is now turning to alternative resources such as solar, hydrogen, and electric batteries [1]. While Lithium ion batteries (LIB) are used primarily in electronic devices, they are also used in automotive applications [2, 3] as an efficient means of energy storage and are increasingly used in the aerospace industry [4–6]. The transition towards electric transport will help meet the recommendations for carbon neutrality by 2050 [7–9].

Firstly, the principles of Li-ion battery functioning will be described as well as their implementation in modules. They represent a safety concern because of their potential risk of thermal runaway. This phenomenon can lead to the release of flammable gases, which can potentially result in fires. After examining these safety issues, the perspectives of using a solid-state Li-ion cell will be discussed, considering its potential to mitigate these combustion-related hazards.

1.1 General background on lithium-ion batteries

A lithium-ion battery is an electrochemical storage system that employs a chemical reaction to transform chemical energy into electrical work and vice-versa. The battery is composed of four main components: a cathode (positive electrode), an anode (negative electrode), a separator, and an electrolyte [10–12].

For cell chemistries commonly available as of this writing, the **cathode** is usually composed of a transition metal oxide having a structure capable of intercalating lithium ions Li^+, such as $LiCoO_2$ (LCO), $Li(Ni_xMn_yCo_z)O_2$ (NMC), $LiMnO_2$ (LMO), $Li(Ni_xCo_yAl_z)O_2$ (NCA) and $LiFePO_4$ (LFP)[1]. The **anode** is often made of graphite Li_xC_6 with insertion sites for lithium ions Li^+. The **electrolyte** is an organic carbonate-based liquid solvent like dimethyl carbonate (DMC) in which a lithium salt is dissolved to facilitate lithium-ion transport. The **separator** consists of a porous membrane like polyethylene (PE) which allows Li^+ ions to move in both directions during charge-discharge cycles.

[1]LCO: Lithium Cobalt Oxide, NMC: Nickel Manganese Cobalt, LMO: Lithium Manganese, NCA: Nickel Cobalt Aluminium, LFP: Lithium-Iron Phosphate

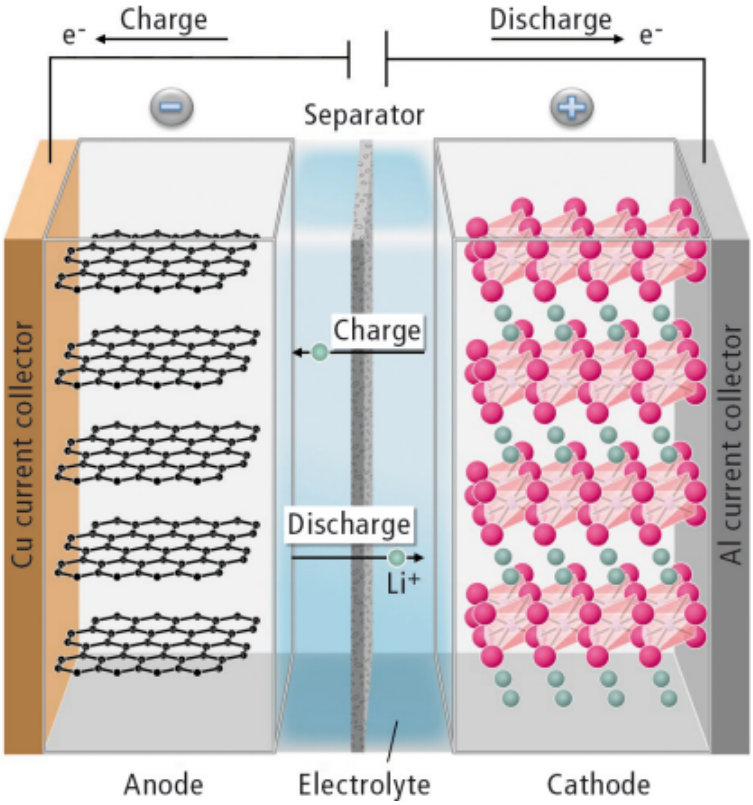

Figure 1.1 Illustration showing a Li-ion during charge-discharge cycles, reprinted from [13] with permissions of Spectroscopy Europe

Figure 1.1 shows how a Li-ion battery works in a charge/discharge cycle. During the discharge cycle, lithium ions are transported from the anode to the cathode through the liquid electrolyte. In the context of discharge, the cathode is the site of the reduction reaction while the anode is the site of the oxidation reaction as illustrated in Figure 1.1. Meanwhile, electrons migrate towards the cathode within the external circuit, thereby ensuring the electrical neutrality of the electrodes. As the reactions are reversible, the entire operation takes place in the opposite direction during the charging process hence the term "rocking chair battery" for the back-and-forth movement of Li^+ during charge/discharge cycles [14].

Thanks to their properties of high energy density, reliable recharging cycles, and high-voltage operation, Li-ion batteries are a fast-growing energy storage in high demand in many fields [15]. In fact, they can be used in different geometries, depending on their field of application. Each individual cell can be stacked into a module, then each module is arranged into a battery pack as shown in Figure 1.2. Electric vehicles (EV) or energy storage centres use different cells grouped together and connected in battery packs.

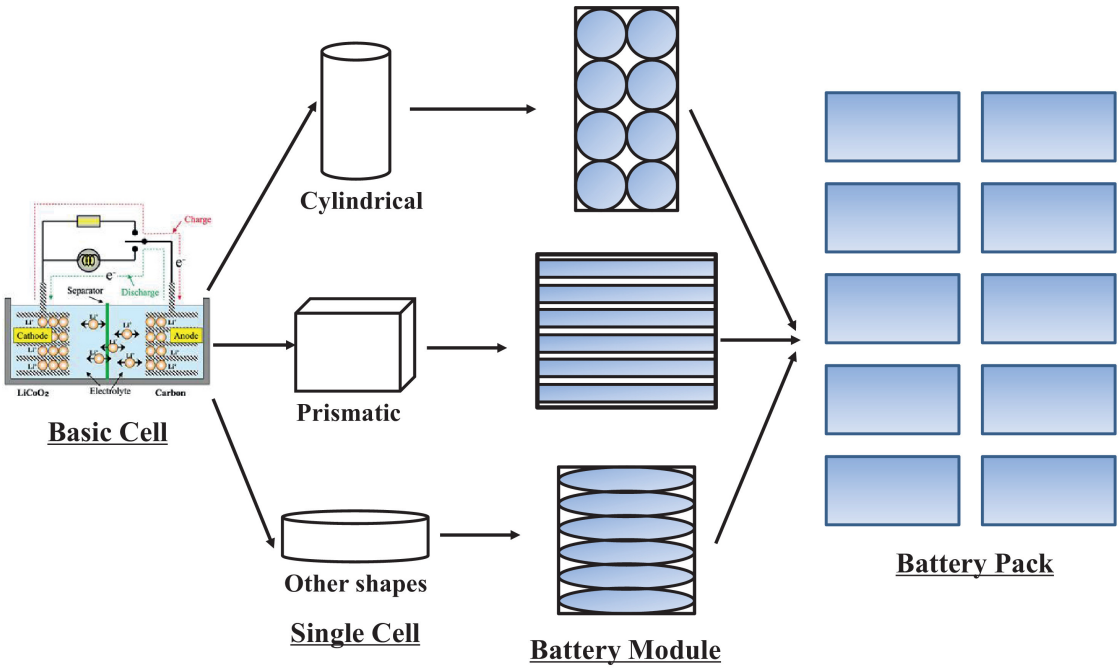

Figure 1.2 From single cells to battery packs for different geometries, reprinted from [14] with Elsevier authorisations

The **cylindrical** cell format is one of the most accessible on the market [16]. These cells are often referred to by their characteristic dimensions, especially the 18650 format (18 mm circular diameter and 65 mm height). They have a wide range of applications, from portable consumer devices (*e.g.*, electronic cigarettes, laser pointers) and medical devices to EVs.

The **prismatic** or **rectangular** format is frequently employed in the design of battery packs, largely due to its compact size and adaptability. The cells are packaged in a robust metallic envelope, frequently made of aluminium, within which the electrodes and electrolyte are arranged in a stacked configuration. These cells are integrated to form battery packs for EVs or for electrical storage systems.

The **pouch** format cells offers a multitude of dimensions. There is no metal case surrounding the cell compared to the prismatic format, so the cell must be handled with care to avoid damage. Renowned for their lightweight format, pouch cells are used in various technologies (*e.g.*, smartphones, laptop batteries, EVs and energy storage).

1.2 Thermal Runaway and gas-phase combustion

A current issue with Li-ion batteries remains the use of a flammable organic liquid electrolyte, which raises health and safety concerns. If subjected to external conditions of abuse such as mechanical deformation, contact with a hot surface, overcharging or internal short circuits, a Li-ion cell will overheat and possibly undergo thermal runaway (TR) [17]. The TR process involves a rapid increase in the internal temperature and pressure of the cell, which triggers a series of exothermic chemical reactions releasing more heat. These chemical reactions lead to a significant damage to the active internal components. Beyond the critical pressure threshold allowed by cells with a vent, a safety vent opens, releasing solid particles, volatile liquids, and flammable gases at high velocity [14]. High-temperature flames can form as a result of the combustion of these gases, leading to potential fire hazards.

In the case of battery packs, there is a risk of fire and TR propagation between neighbouring cells. Figure 1.3 illustrates the various mechanisms leading to TR propagation within a module. Convective heat transfer due to venting of gases can contribute to the propagation of damage between cells or across modules. The recirculation of gas vented within the module can generate hot spots which could cause TR in adjacent cells. Moreover, heat conduction across solid interfaces can propagate TR from cell to cell inside a module [18, 19]. Therefore factors including the layout of the cells and their spacing within a module, must be taken into account to prevent the propagation of thermal runaway.

These risks are the main obstacles to the safe use of Li-ion cells in the transport sector, and particularly in aviation. In fact, a report published by the Federal Aviation Administration (FAA) [21, 22] has identified the various risks associated with fires caused by Li-ion batteries in the aviation industry. These types of accidents have shown that there is a pressing need to anticipate these risks, particularly by studying the thermal runaway mechanism of Li-ion cells both experimentally and numerically.

Thermal runaway remains a complex phenomenon to study and model, especially on the coupling between the different phases of TR. Numerous studies have numerically modelled thermal runaway and the combustion of flammable gases vented by liquid-electrolyte Li-ion cells [20, 23]. The ejection of the gas mixture during the venting phase[2] takes place at high velocity under the build-up of internal pressure. The flow of the gas mixture is turbulent, which increases the complexity of CFD simulation during thermal runaway and requires a more sophisticated approach compared to laminar flow modelling.

[2]TR phase when the safety vent is opened under the pressure build-up and the cell emits a gas mixture.

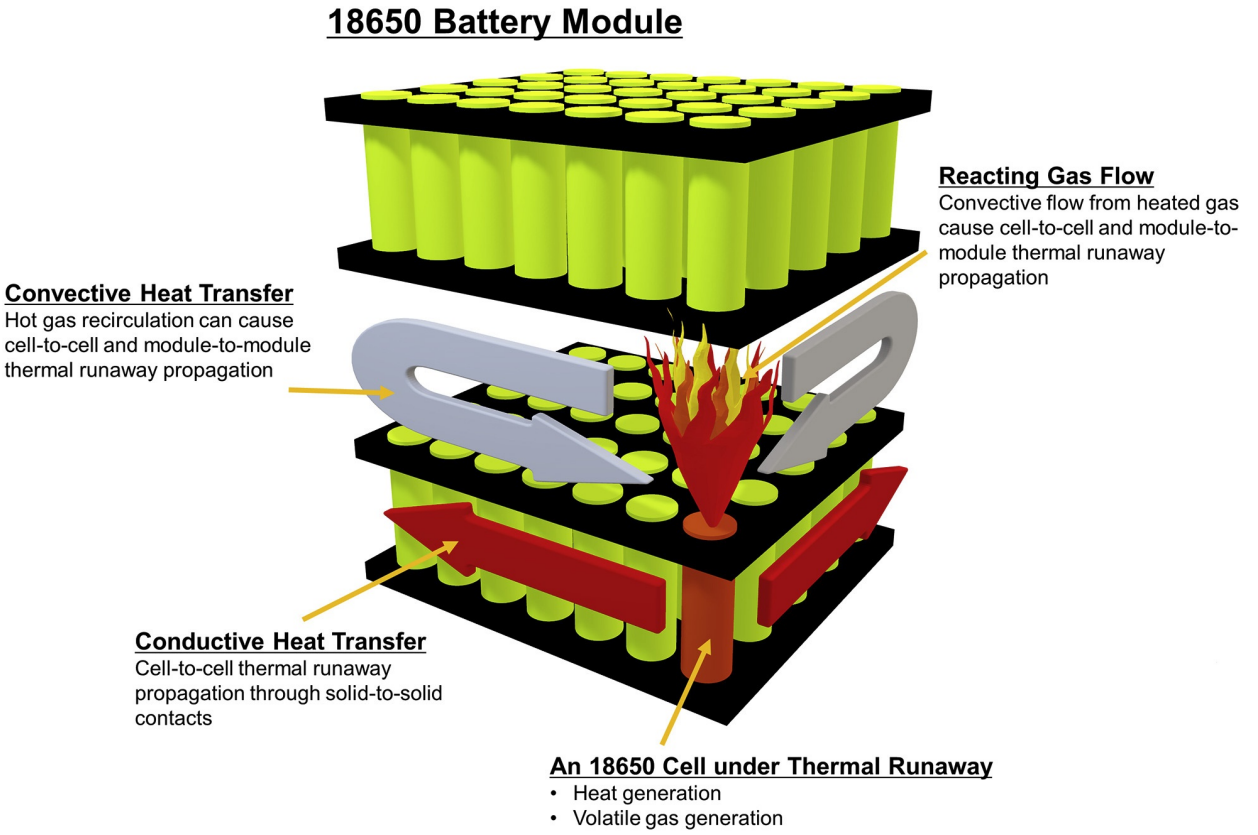

Figure 1.3 Various mechanisms of thermal runaway propagation illustrated in a module containing 18650 cylindrical Li-ion cells, adapted from [20] with Elsevier permissions

Computational Fluid Dynamics (CFD) models are commonly used to simulate turbulent jet flows and the formation of flames in the gas phase [20, 24]. Numerical modelling represents a significant challenge in terms of the interaction between flow turbulence scales and the kinetics of chemical reactions in the gas phase, named Turbulence Chemistry Interaction (TCI). If this interaction is not considered correctly, it leads to a prediction error in the heat release rate [25, 26]. Other issues add complexity to the modelling, such as the configuration of the flow of flammable gases emitted from the cell or the chemical composition of the gas mixture [20]. Although thermal runaway modelling is documented for cylindrical cells, few studies have been carried out on the venting phase and the effects of gas-phase combustion process within a module for other cell geometries. Understanding the gas phase reactions leading to the TR propagation in modules is required for the safe design of future battery packs.

While these safety issues persist with cells with liquid electrolyte, recent advances in solid electrolyte Li-ion batteries offer promising alternatives. However, the transition to all-solid-state batteries presents its own set of challenges.

1.3 Challenges for the development of new solid-electrolyte Li-ion cells

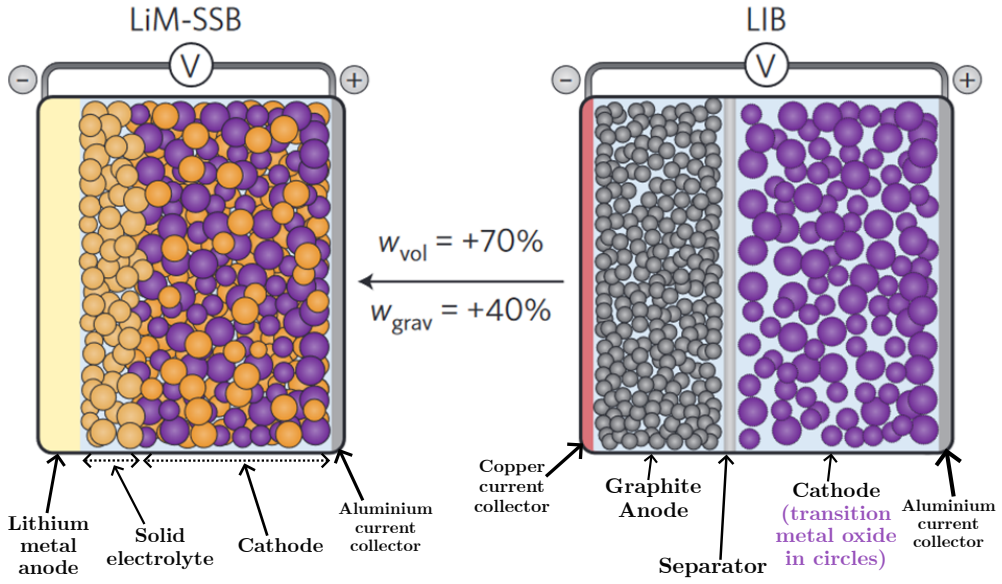

Figure 1.4 Comparison of the architecture of liquid-electrolyte Li-ion cells (LIB) and a solid-electrolyte cell using a lithium metal anode (LiM-SSB) in yellow improving the specific energy of the standard Li-ion cell adapted from [27]

A battery using a solid electrolyte can deliver high energy densities while providing greater safety against the risk of fire than cells with liquid electrolyte [27]. Although the use of a solid electrolyte has the disadvantage of slower kinetics and lower conductivity for internal chemical reactions, it can deliver high energy output for transport applications [28]. This type of electrolyte has the advantage of being stable over a wider range of temperatures than liquid electrolytes [29]. Solid inorganic or organic electrolytes like polymers, enable lithium ions to be transmitted and act as separators within the cell [30]. One promising strategy behind this technology is to use a lithium metal anode to increase energy density [27].

Nevertheless, there are technological challenges to the large-scale production of this new type of solid electrolyte battery. The interfaces between the electrodes and the electrolyte must be controlled in the absence of humidity [30]. Lithium metal exhibits spontaneous reactivity in contact with water, resulting in exothermic reactions that generate H_2. It displays reactivity when it comes into contact with dioxygen and nitrogen, requiring careful handling [11, 31]. Therefore, an inert gas must be used to fill the inside of lithium metal battery modules to avoid any contact with humidity [32].

Similar to Li-ion cells, all solid-state batteries can also suffer thermal runaway under mechanical failure or overheating conditions [29]. However, numerical modelling of thermal runaway, solid-phase degradation reactions within solid-electrolyte batteries are missing in the literature compared to liquid-electrolyte cells.

1.4 Research context

This research work is part of a broader project addressing safety challenges in aeronautical and aerospace applications, where understanding and mitigating risks are critical. This study aims to investigate and model gas release and combustion processes during thermal runaway in battery modules through numerical simulations. Numerical modelling serves as a tool to analyze the physical and chemical mechanisms underlying thermal runaway. By providing predictive insights into battery cell behaviour under extreme conditions, this approach complements experimental investigations.

Therefore, this work presents a numerical modelling approach in ANSYS Fluent to study the turbulent combustion of vented gas mixtures in a specific battery module geometry. The model integrates existing sub-models from the literature into the Fluent software. Since no experimental data are available for all-solid-state battery modules, numerical simulations rely on data from LiB cells with liquid electrolytes. Additionally, an inert gas mixture filling the battery module is considered to replicate the operating conditions of an all-solid-state battery module.

1.5 Thesis outline

Firstly, a literature review on self-ignition conditions leading to flame formation and the state of the art of numerical models of turbulent combustion of Li-ion cells will be carried out. Secondly, the methodology and modelling strategy adapted to the battery module geometry will be considered. A discussion of the numerical models available on the commercial CFD software ANSYS® Fluent will be shown to choose a model that most appropriately represents auto-ignition conditions of the gas mixture. Finally, a presentation of the main results of various combustion models will be given, followed by a discussion of the sensitivity of the model to physical parameters. A conclusion and perspectives will be drawn on the numerical modelling criteria to validate it experimentally, with a perspective view to combine it with solid-phase reaction models.

CHAPTER 2 LITERATURE REVIEW

This chapter describes the behaviour of the mixture of flammable gases emitted by a Li-ion cell during thermal runaway. The state of the art in numerical modelling of turbulent gas-phase combustion applied to the venting of a Li-ion cell is detailed. In particular, the importance of numerical models will be discussed for predicting the ignition conditions of a gas mixture as a function of its temperature and chemical composition.

2.1 Fire behaviour of Li-ion cells

Subjected to the conditions of abuse leading to thermal runaway, Li-ion cylindrical batteries emit a flammable gaseous mixture accompanied by hot solid particles at high velocity. They also release heat from exothermic chemical reactions under the build-up of internal pressure. Therefore they are responsible for numerous explosion and fire hazards. Table A.1 in Appendix A lists the various recent incidents involving Li-ion batteries, showing that this is still a current issue.

The influence of the battery's chemical composition on the auto-ignition conditions of the gaseous mixture emitted will be discussed, leading to the formation of a flame and the resulting heat release.

2.1.1 Auto-ignition and flame conditions for gas mixtures

To initiate the combustion reaction, at least 3 elements must be present at the same time, as illustrated by the "fire triangle" in Figure 2.1: an oxidiser, a fuel, and an activation energy source. The ambient air provides the oxidant (oxygen) and the gaseous mixture ejected into the external environment plays the role of the fuel [33].

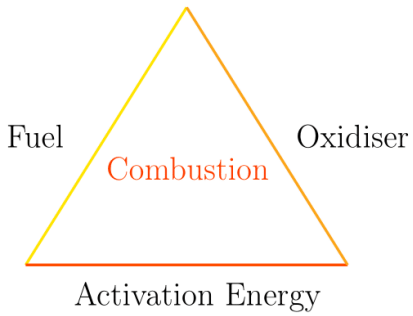

Figure 2.1 Diagram of the three conditions to be met to obtain a flame, inspired from Wang *et al.* [33]

A fourth element involves chain reactions in the gas phase, which can influence auto-ignition processes. These reactions represent a key domain where the interactions between turbulence and chemical kinetics become particularly pronounced.

Gas compositions

As mentioned in the introduction, several Li-ion cell chemistries exist each with specific chemical composition linked to its components. The gaseous mixture resulting from the internal decomposition reactions of the active elements depend strongly on the battery chemistry [17].

In a study carried out on three types of cathodes (NMC, LCO/NMC and LFP) for cylindrical Li-ion batteries, Golubkov *et al.* [34, 35] measured the chemical composition and quantity of the gas mixture emitted during thermal runaway. Figure 2.2 shows the chemical composition of the gas mixture emitted during venting associated with the three types of cathode chemistry for a battery state of charge of 100% [34]. The experimental measurements focused on the detection of the gases N_2, H_2, CO_2, CO, CH_4, C_2H_4 and C_2H_6 using gas chromatography with argon and helium as carrier gases. The chemical composition of the gas mixture varies between the different types of cell chemistry. Carbon dioxide CO_2 and dihydrogen H_2 are produced in majority by the three cells, followed by carbon monoxide CO and hydrocarbons (CH_4 and C_2H_4) in decreasing order of emission. In all three types of cathode chemistry, it should be noted that most of the gases emitted during venting are flammable in contact with ambient air [14, 34].

The amount and composition of gas released from a Li-ion battery depend on its state of charge (SOC) [35]. Gas release is typically highest when the cell is at its maximum charge level. Golubkov *et al.* [35] showed the SOC influence on cylindrical NCA (3.35 Ah nominal capacity) and LFP cell (1.1 Ah nominal capacity) during thermal runaway. According to Figure 2.3, the quantity of gas increases significantly depending on the load level of the cell between 0 and 100% SOC. In addition, the maximum cell temperature increases as a function of the battery state of charge for both cell types. For both types of cathode, the composition of the gas mixture emitted by the cell varies according to its state of charge, as can be seen from the evolution of the curves for the main gases detected. The composition of CO_2 decreases in favour of CO and H_2 as the SOC increases. The main difference between the two types of cell is the quantity of gas produced, where it can be seen that the quantity of gas emitted by an LFP cell (between 5 and 16 mmol/Wh) is less than that from an NCA cell (between 3 and 21 mmol/Wh) for the same SOC. The mmol/Wh unit is used to normalize the quantity of gas emitted in relation to the energy stored in the cell. Although these ranges overlap, the general trend shows that LFP cells produce less gas on average than NCA cells during thermal runaway for the same SOC. Higher gas production in NCA cells could mean a greater risk of serious incidents during a thermal runaway. This is due to the greater chemical stability of the $LiFePO_4$ cathode, especially the high energy of the $P-O$ covalent bond present in the polyanion PO_4^{2-} [36].

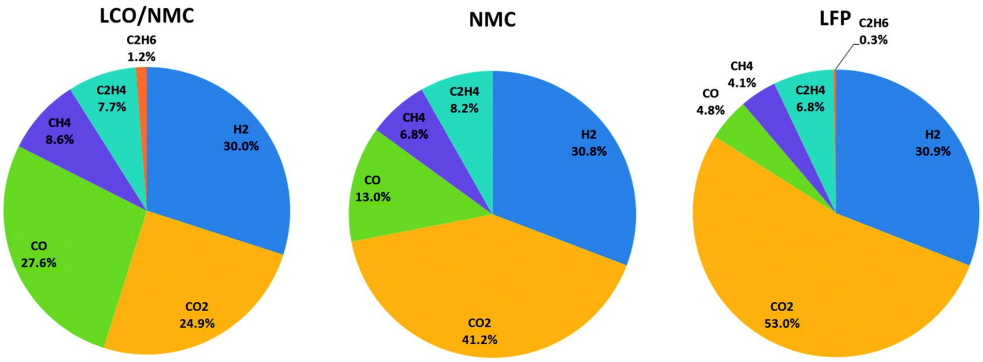

Figure 2.2 Gas detection for each type of Li-ion cell cathode at 100% SOC, adapted from [34] with permission from the Royal Society of Chemistry

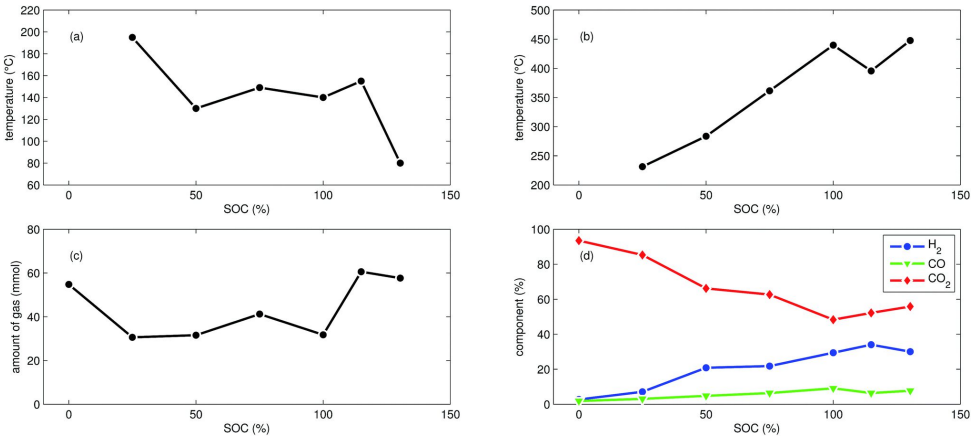

(a) LFP cell

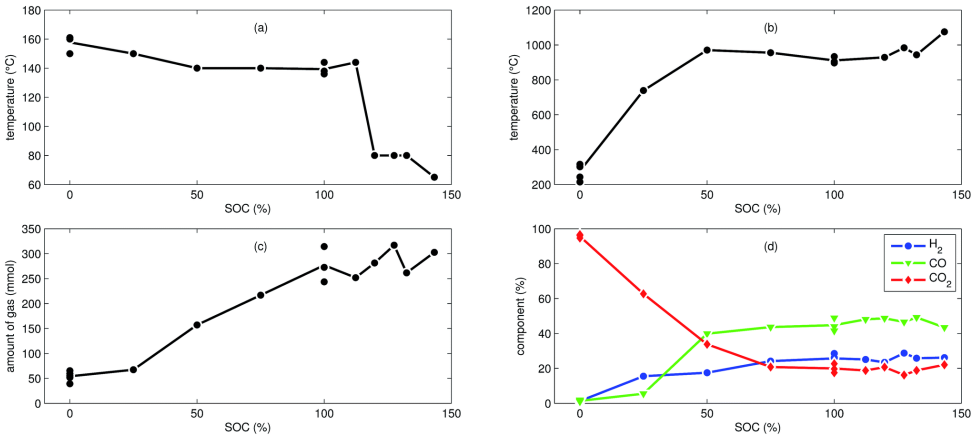

(b) NCA cell

Figure 2.3 LFP and NCA cell thermal runaway parameters as a function of SOC: (**a**) Onset temperature, (**b**) Maximum cell temperature, (**c**) Amount of vented gas, (**d**) Detection of the main gases emitted by the cell, reproduced from [35] with permission from the Royal Society of Chemistry

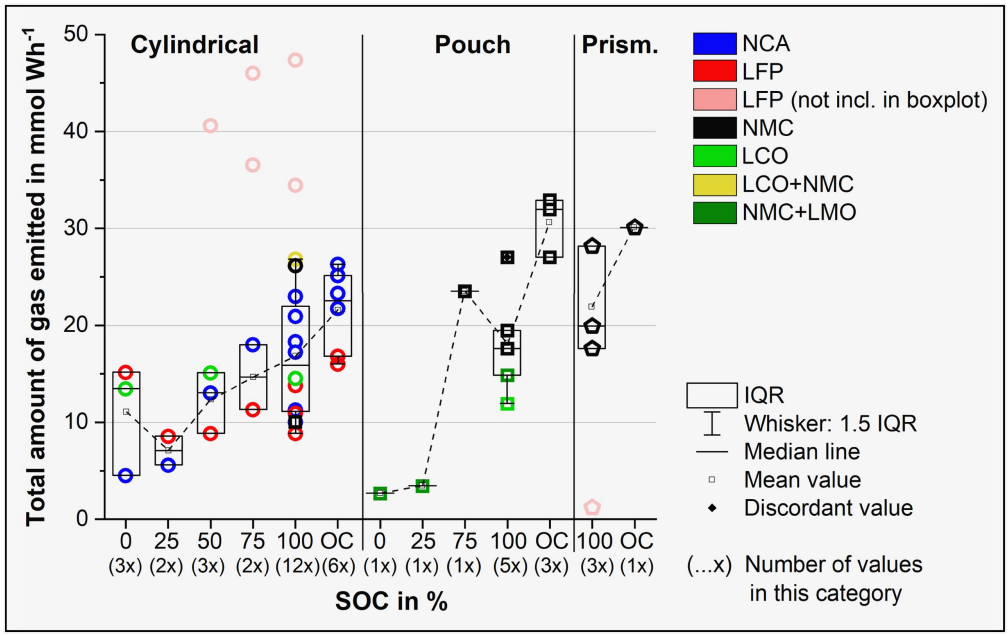

Figure 2.4 Total amount of gas vented during thermal runaway as a function of SOC for each Li-ion cell type across various articles, reproduced from [37] with permission of Elsevier

Figure 2.4 illustrates the amount of gas emitted for 42 experimental tests for different types of geometry across a meta-analysis of 8 papers [37]. According to this analysis, it can be seen that the data for the cylindrical geometry shows an increasing trend in the amount of gas emitted as a function of the SOC of the cell, excluding the data in the pink circles which is too far from the other values. No explanations were provided in the study for the discrepancies observed in these data circles. It shows also that the material used for the cathode has an influence on the amount of gas emitted into the external domain for the same state of charge. In fact, a NCA cell will emit more gas during venting compared with other cathode materials; a LFP cell will emit the least. The research conducted by Golubkov *et al.* [35] reveals comparable trends.

For other geometries, including prismatic and pouch cells, the link between rising SOC and increased gas emissions has been observed according to Figure 2.4, but this observation requires further scientific validation [37]. In addition, there is too much uncertainty about the values due to a lack of experimental data on these two types of geometries [37]. In fact, cylindrical cells, because of their commercial predominance in technological applications, are the most studied in the literature compared with other cell geometries. Rappsilber *et al.* [37] highlight the knowledge gap about the accuracy of measurements of the quantity of gas emitted and its chemical composition for other types of geometry. Moreover, only the total emission of the quantity of gas is measured in the study, whereas the risk of a fire starting is also influenced by the mass flow rate of gas in the cell.

Flame conditions

The degradation reactions occurring within LIB materials, such as the electrolyte, lead to the emission of aerosols in the form of fine liquid and solid particles, accompanied by flammable gases that can burn on contact with the outside air [38].

When the flammability thresholds of the gas mixture are reached, the presence of sparks or a hot source can ignite the mixture and lead to the formation of flames [33]. In addition, the gas mixture can also self-ignite on contact with air if its temperature is sufficiently high [14].

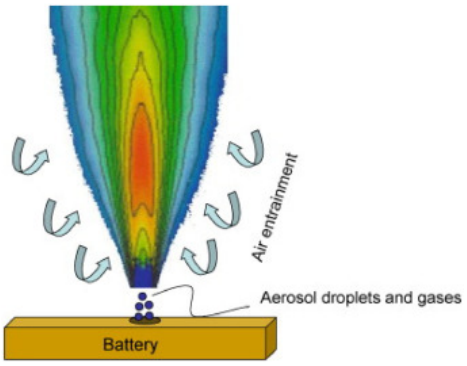

Figure 2.5 Illustration of the flame formation from the gas mixture, aerosol droplets and the electrolyte evaporation. The curved lines of the flame correspond to the temperature iso-contours. Figure reproduced from [38] with the Elsevier permission

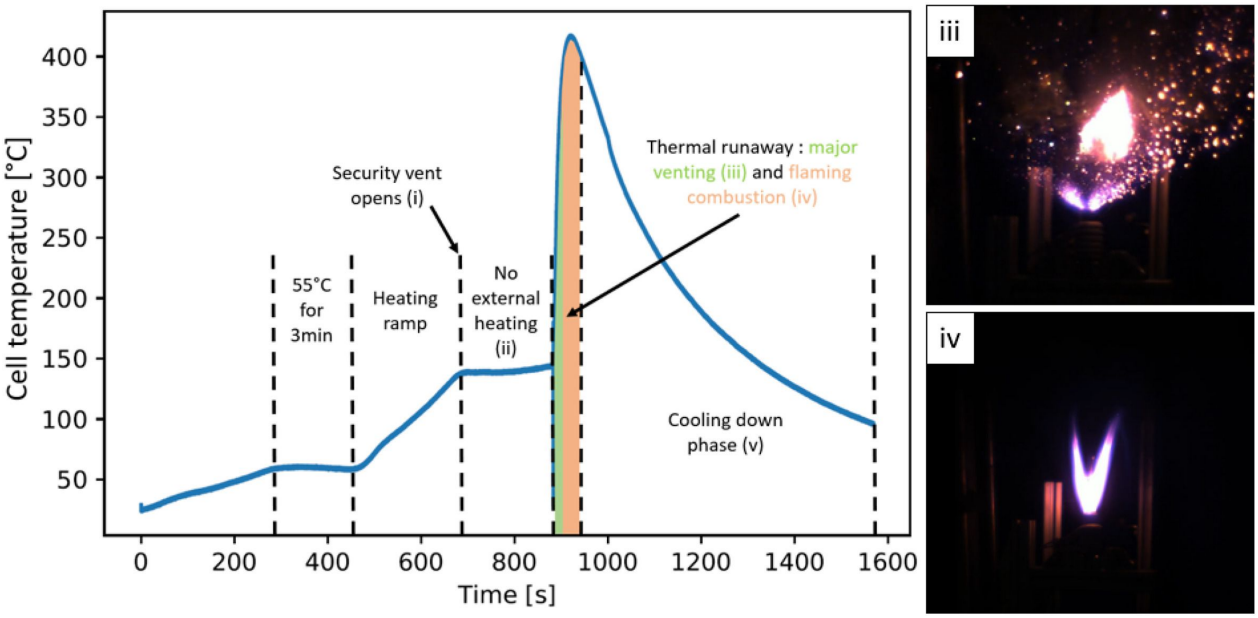

Figure 2.6 Main steps of thermal runaway in a fully charged (100% SOC) cylindrical cell under overheating conditions with experimental images, adapted from [39] with Elsevier permission

Several studies [39–43] have shown that the behaviour of Li-ion cells can be divided into different stages of TR leading to the formation of flames. Goupil *et al.* [39] investigated the thermal resistance of a 18650 NMC/graphite cylindrical cell, and documented the sequential stages of thermal runaway. The authors designed a heating system around the cell casing to simulate overheating conditions like heating ramp on LiB cells. Figure 2.6 describes the main stages in the thermal runaway of a cylindrical cell, with two experimental images showing the

formation of flames. After the opening of the vent, the cell temperature slowly increases and gas is emitted from the cell. Once the major venting phase is reached, there is an emission of smoke and solid particles at high temperature during venting phase (phase **iii**) followed by the formation of a stable flame (phase **iv**) accompanied by the release of heat as shown in Figure 2.6. Finally, the decrease in gas mixture emissions leads to flame extinction and the cooling of the cell (phase **v**).

The flame formed can be considered as non-premixed or partially premixed depending on how the fuel and oxidant regions are mixed. The definitions of these two types of flame are given below.

A non-premixed or diffusion flame is formed following the separate injection of fuel and oxidant into a chamber. Chemical reactions take place in a defined region where the reactants (oxidant and fuel) are in stoichiometric proportions. The fuel and oxidant diffuse into the reaction zone where they burn, generating heat. The temperature in this region is at its highest and spreads away from the flame front towards the oxidant and fuel stream [25, 26]. It differs from premixed flames where the reactants are initially mixed in the chamber before the combustion reactions take place. The reactants must mix fast enough in the reaction zone for the combustion process to take place.

In the majority of experimental studies of battery flames, a partially premixed flame is observed [20, 23]. A partially premixed flame features characteristics of both non-premixed and premixed flames. In battery flames, a partially premixed flame is formed when the reaction zone stabilizes at a certain height from the vent outlet, such that the oxidant and the fuel can partially mix upstream of the stabilization point.

Many strategies on diffusion and partially premixed flames rely on simplified assumptions, which will be detailed in the numerical models in the *Methodology* part.

2.2 Numerical modelling of gas phase turbulent combustion for Li-ion cells

This section covers the state of the art on numerical modelling of turbulent combustion in the gas phase during the venting of Li-ion cells. First, the modelling of jet turbulence during venting will be discussed. Then, a state-of-the-art of the various numerical models used for turbulent combustion of vented gas mixtures will be presented.

Table 2.1 lists the numerical models for the venting and turbulent combustion of gases emitted by a LiB cell. Researchers selected these models specifically for their ability to model one or both phenomena simultaneously. The main characteristics and assumptions of the models in each study are given in the table. Terms in the solver row such as "MATLAB" and "ANSYS Fluent" refer to the associated programming language and the CFD commercial software while "AVBP" corresponds to the solver developed by CERFACS [44]. Recent articles typically adopt a Reynolds-Average Navier Stokes (RANS) formulation to solve the flow field outside the Li-ion cell with ANSYS Fluent as the main CFD solver as it can handle jet turbulence and combustion reactions. This statistical method is used to resolve the mean values of the flow properties, and modelling is carried out to take account of the turbulence effect on the mean quantities. This numerical approach has the advantage of low computational cost but has some limitations in terms of accuracy for modelling turbulent structures. Other approaches, such as Large Eddy Simulations (LES), used by Cellier *et al.* [45], take a more accurate method to turbulence modelling. This numerical approach consists of filtering the governing equations of turbulent flows. It provides more information about the large turbulent structures that are computed explicitly while modelling only the smaller scales [26]. It gives greater precision on turbulent combustion and the formation of a flame. Therefore, the cost of numerical calculation is greater than with the RANS approach.

Table 2.1 Recent numerical models used to study the turbulent combustion of the gas mixture from Li-ion cells in the literature

Numerical models	Ostanek *et al.* (2020) [46]	Li *et al.* (2021) [24]	Kim *et al.* (2021) [20]	Mishra *et al.* (2022) [47]	Zhao *et al.* (2023) [23]	Cellier *et al.* (2023) [45]
Numerical Approach	ODE solver with 0D model	RANS	RANS	RANS	RANS	LES
Solver or Software used	MATLAB	ANSYS Fluent R19	ANSYS Fluent R19	ANSYS Fluent	ANSYS Fluent	AVBP code
Venting phenomenon	Compressible flow through a sharp-edged orifice	Compressible flow through a sharp-edged orifice	Porous media	Isentropic flow equation for a gas passing through a nozzle	Pressure difference	Not given
Combustion mechanism	Not given	Not given	6 species and 5 reactions	32 species and 206 reactions	5 species and 10 reactions	24 species and 93 reactions (Analytically Reduced Chemistry)
Combustion model	Not given	Not given	Laminar Finite-Rate/Eddy-Dissipation	Non-Premixed Combustion	Partially-Premixed Combustion	Laminar Finite-Rate

2.2.1 State of the art of venting flow modelling

In this section, numerical modelling of the behaviour of the turbulent ejection of the gas mixture from Li-ion cells during venting is presented.

Each cylindrical cell or battery module is fitted with a safety vent to prevent the risks of explosion. The safety vent aims to release the gases produced inside the cell as mentioned in the previous section [48–50]. It is basically a security pressure relief valve, which opens when the internal pressure exceeds a threshold value ranging from a few bars to approximately ten bars [48, 51].

In a study published by Li *et al.* [24], RANS CFD simulations based on a finite volume method were conducted using Ansys Fluent 19R2 on cylindrical Li-ion cells to visualize the non-reactive flow through the venting holes. Various commercially available 18650 battery

caps were studied: MTI, LG MJ1, K2, and LG M36. Each cap was scanned using computed tomography to extract a CAD model. Mach number[1] (Ma) and turbulent mixing distributions were calculated by Fluent for an internal to ambient pressure ratio ranging from 1.2 to 8. Figure 2.7 shows the results of Mach number distribution around the vent outlet area in a cross-sectional plane including the battery cap. It can be seen, for each cap, that the flow velocity is supersonic, with a Mach number equal or superior to 1 close to the vent outlet. Figure 2.7 displays results for a pressure ratio of seven, revealing Reynolds numbers for the MTI, LG MJ1, K2, and LG M36 caps as $1,06 \times 10^5$, $1,12 \times 10^5$, $7,75 \times 10^4$, and $1,27 \times 10^5$ respectively, which confirms a fully turbulent jet flow. For this study, the authors used the Realizable $k - \epsilon$ two-equation model, which is widely used for modelling turbulent jets and for turbulent combustion prediction [52]. The venting flow is asymmetric due to the burst disk blocking some venting holes, which may influence the combustion of the vented gas.

Kong *et al.* [53] studied, using the OpenFOAM solver [54], the venting conditions and pressure evolution for Li-ion cylindrical cells at various SOC (25%, 50%, and 75%). The authors analysed the vent opening threshold due to the internal build-up of gas pressure within the cell and calculated the dynamic properties of the flow around the vent region. Figure 2.8 shows the distribution of Mach number (Ma) and gas flow velocity calculated at the vent outlet region for each SOC of the Li-ion cells. In the velocity profiles, the first venting peak corresponds to the moment when the safety valve is opened, while the second peak corresponds to the onset of thermal runaway in the cell accompanied by the release of the gas mixture. The higher the SOC, the shorter the delay to the first venting peak, as can be seen from the velocity profiles in Figure 2.8. In fact, cells subjected to extreme abuse conditions with a higher SOC can release more energy and generate more gas, leading to a more rapid rise in internal pressure and a shorter delay in the venting phase. According to the curves in Figure 2.8, it can be noted that the jet emitted during the second venting for the 25% SOC is subsonic with Ma below 1, whereas the other two SOC indicate choked flow when Ma is equal to 1.

The models presented above mainly analysed the non-reactive and turbulent venting of gas mixtures. However, due to their high temperature and chemical reactivity, it is likely as observed experimentally that a flame will ignite. The flame can stabilize on the cell resulting in a risk of TR propagation to neighbouring cells. Therefore numerical modelling of turbulent combustion in the surrounding environment has been attempted to quantify its heat release.

[1]Dimensionless number; corresponds to the ratio of local flow velocity v to the local speed of sound c noted $Ma = \frac{v}{c}$

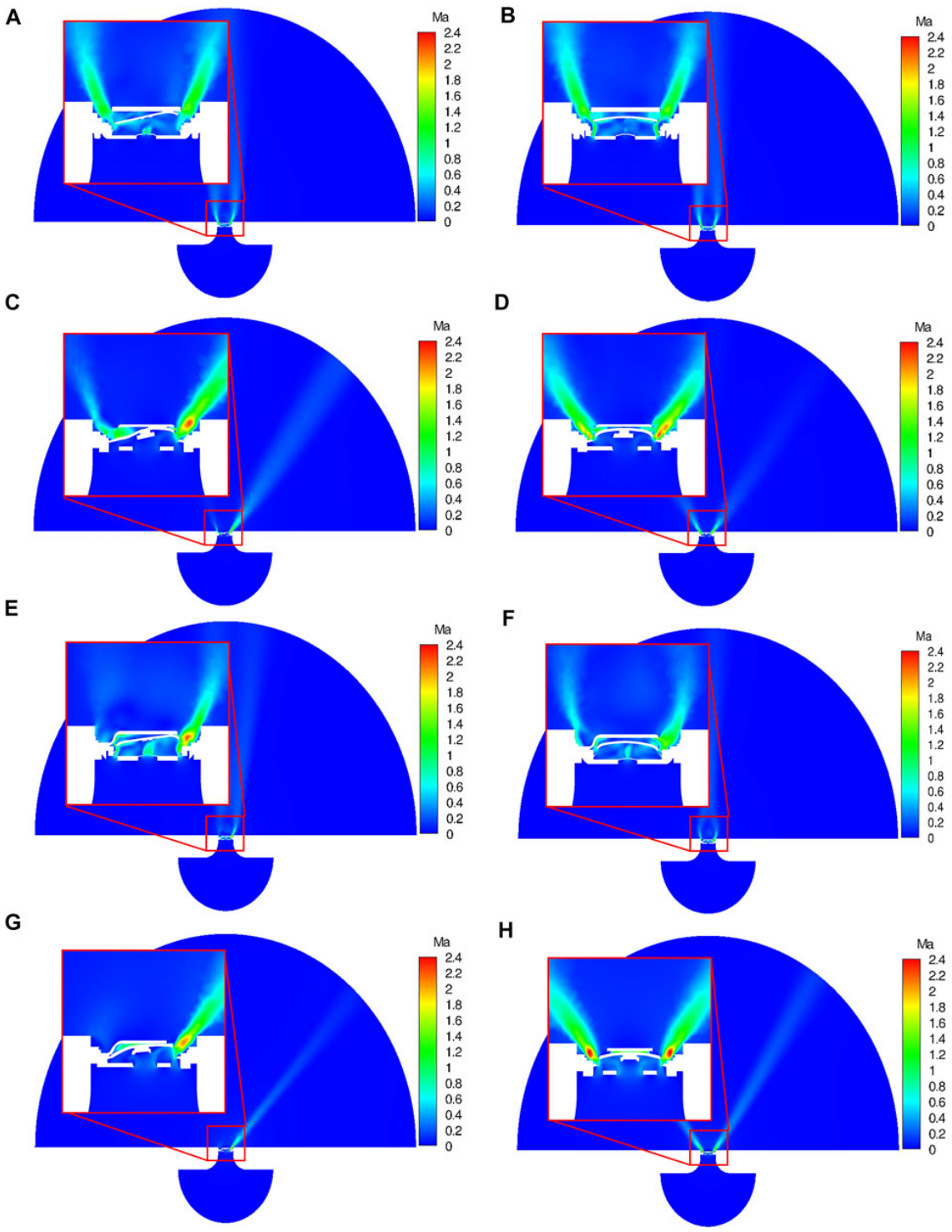

Figure 2.7 Mach number distribution for the MTI (A, B), LG MJ1 (C, D), K2 (E, F) and LG M36 (G, H) cells for a pressure ratio of seven. Left column is the normal plane along the X axis and right column is normal plane along the Z axis, reprinted from [24] with Frontiers permission

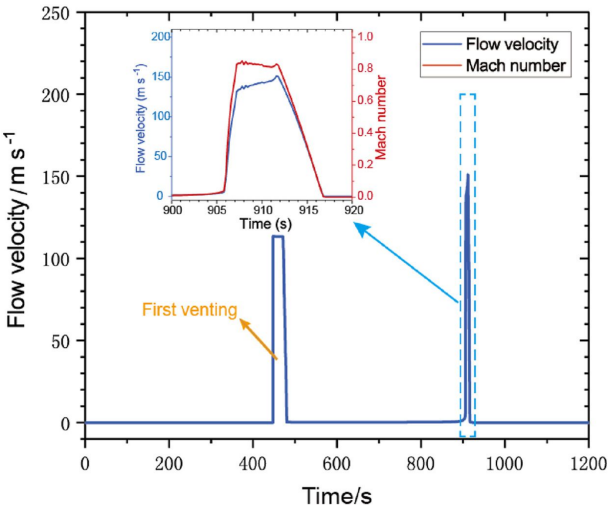

(a) The flow velocity and Mach number variations for the cell at 25% SOC

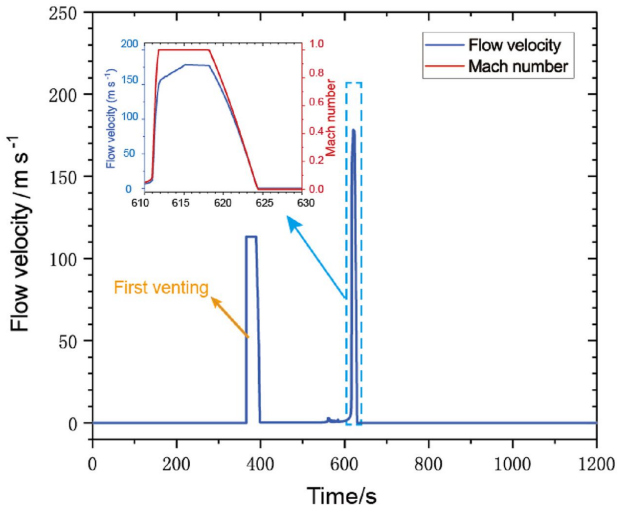

(b) The flow velocity and Mach number variations for the cell at 50% SOC

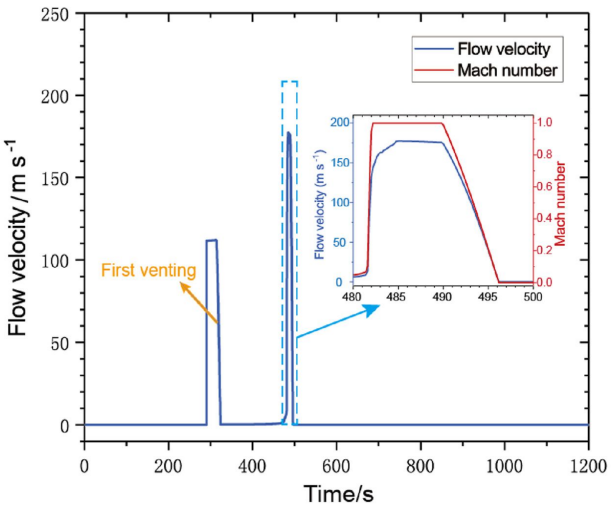

(c) The flow velocity and Mach number variations for the cell at 75% SOC

Figure 2.8 Temporal variations in Mach number and velocity profiles at the vent outlet region for 3 cylindrical Li-ion cells with 25% SOC (curve **a**), 50% SOC (curve **b**) and 75% SOC (curve **c**), adapted with Elsevier permissions from [53]

2.2.2 Gas phase turbulent combustion modelling

This section reviews the combustion models for gas mixtures released during the thermal runaway. The gas mixtures ejected by the cell is highly turbulent making the combustion modelling more complex. The wide range of combustion models and chemical reaction mechanisms requires a proper validation process to select the most accurate for each application.

Four types of combustion models have been used in CFD to approach turbulent combustion in the gas phase to describe LIB flames. A first model assumes non-premixed combustion, with the flame properties tabulated in the mixture fraction space using simple precursor 0D or 1D models. A second model assumes premixed combustion, with the properties tabulated in the reaction progress variable space [25]. This model is rarely used as the cell emits a fuel mixture rather than a fuel/oxidizer mixture [34, 35]. A third type of combustion model called partially premixed combustion combines the first two approaches. This type of model is preferred when the situation does not really represent pure non premixed or premixed combustion as discussed in Section 2.1.1. A fourth model called Species Transport, involves solving the transport equations for each chemical species in the gas phase.

Various chemical mechanisms can be used to model combustion reactions, taking into account the kinetics of reactions in the gas phase. The choice of chemical mechanism into a 3D solver is crucial to ensure both accuracy and low computational cost. Given the large number of existing chemical mechanisms, the validation of kinetic scheme for the combustion of gases released by a cell are discussed later.

Kim *et al.* [20] developed a numerical model of the venting and gas phase reactions of 18650 NCA batteries by using a RANS formulation to describe external flows. The authors conducted simulations using Ansys Fluent, incorporating experimental data obtained from Golubkov *et al.* [35] for the gas composition vented from Li-ion cells. The turbulent combustion of the vented gases is modelled with the Eddy-Dissipation/Finite-rate approach provided by the Fluent Species Transport combustion model. The gas-phase chemical mechanism is based on five reactions for the six species measured by Golubkov *et al.* [35]. In the study, the authors show that a flame is predicted to stabilize near the cell vent for approximately 5 seconds for 100% SOC. The model was also run for different SOCs, which affected the temperature field as shown in Figure 2.9. A flame is only observed in the 50% SOC and 100% SOC cases, with a different maximum flame height and duration. This study shows that high SOC plays a key role on the amount of gas released and the formation of flames.

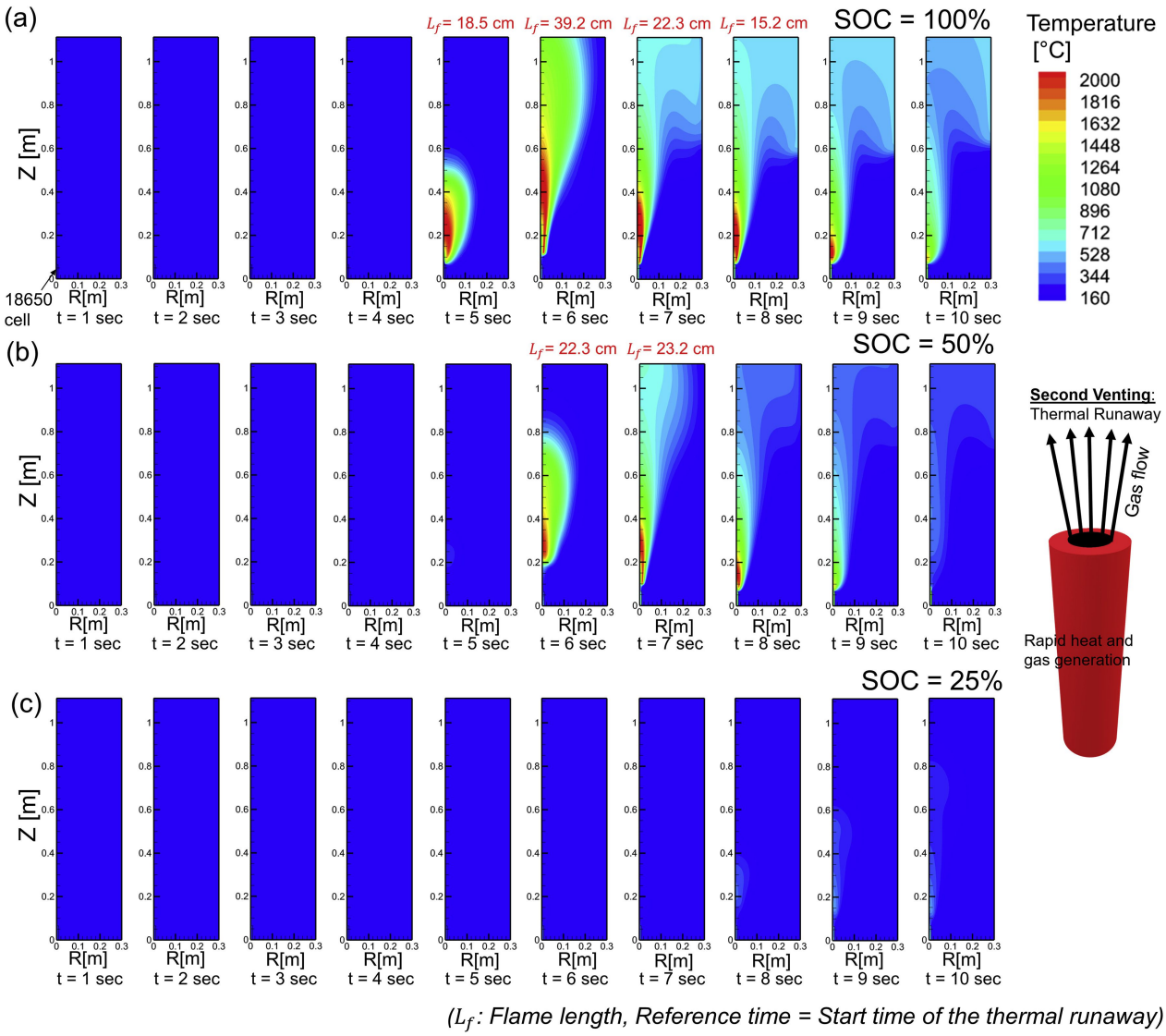

Figure 2.9 Temporal evolution of the temperature field after the onset of the second venting for various SOC: 100% (contour **a**), 50% (contour **b**), 25% (contour **c**), reproduced from [20] with Elsevier permission

Zhao *et al.* [23] have developed a similar model in Ansys Fluent, including the heat generated by the combustion. A 2D CFD model was used for the flow field complemented by a 0D model that simulated the coupling between the heat generation, gas production, and venting. For the venting sub-model, the internal pressure of the cell is computed using the ideal gas law and the jet velocity using the isentropic flow equations. The vent opening is determined by the pressure difference. The injection velocity obtained in this sub-model is then used as the boundary condition in the 2D CFD model. The domain is defined as 2D axisymmetric to reduce computational costs. Gas combustion is solved using a partially premixed combustion model assuming that the vented gases are a mixture of fuel and oxygen generated by the cathode decomposition. Numerical simulations and experiments conducted by the authors

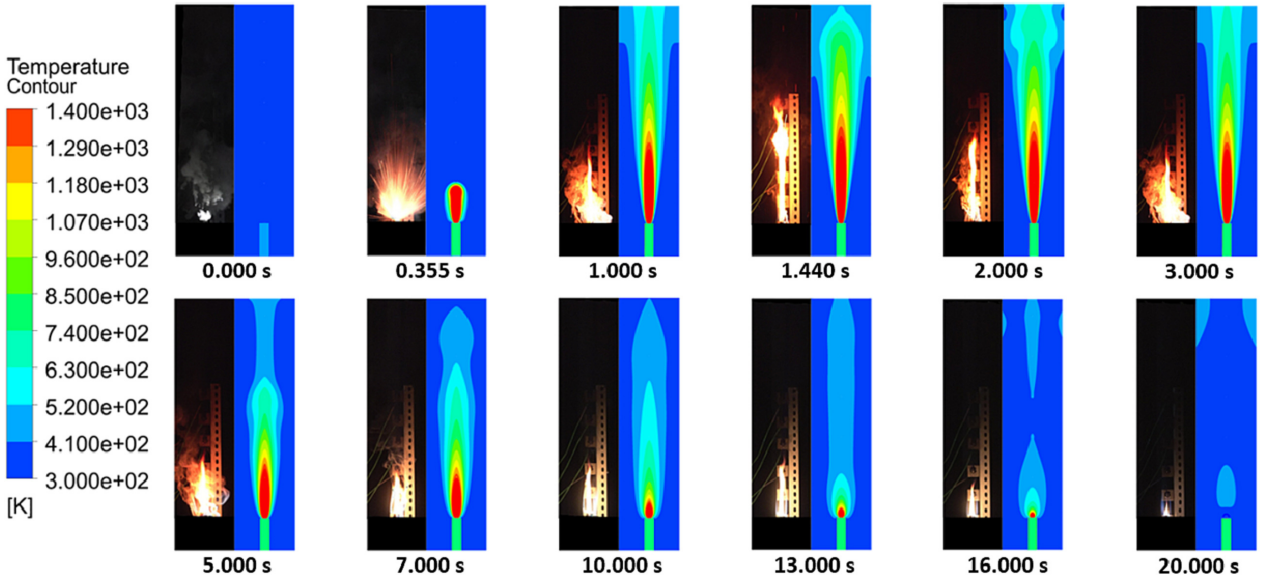

(a) Chronology of the venting phase and combustion reactions compared with experimental images

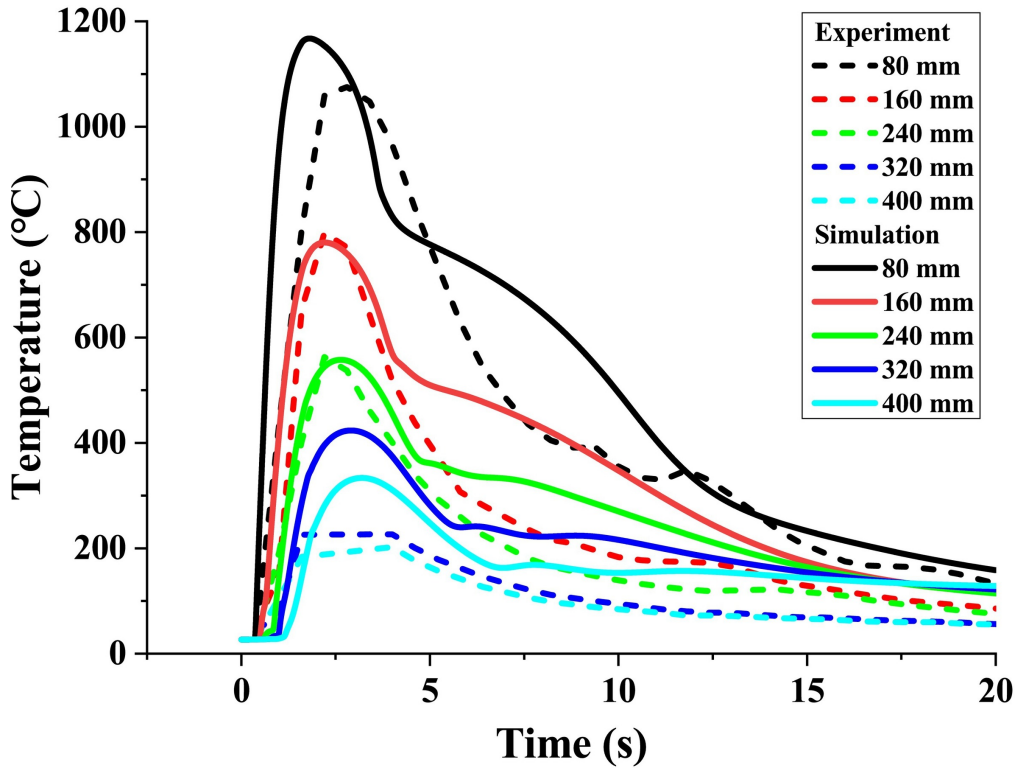

(b) Comparison of the temporal evolution of the temperature of the gas mixture as a function of height

Figure 2.10 Comparison between the experiment and the simulation based on (fig. **a**) the gas temperature at different heights and (fig. **b**) the flame height fire images and temperature distribution, reproduced from [23] with Elsevier permissions

are compared in Figure 2.10. Figure 2.10a illustrates a synchronized comparison between the computed temperature distributions and experimental images of the flame, which gives good agreements between actual and predicted flame heights. Figure 2.10b shows the temperature at a few locations along the streamwise direction. It is noted that the signal from the thermocouples at 320 and 400 mm was lost from t = 2s to 5s, explaining the differences between simulated and experimental result curves. While real-time measurement of temperature evolution remains experimentally challenging, it is important to view the overlaid curves with appropriate caution in Figure 2.10b.

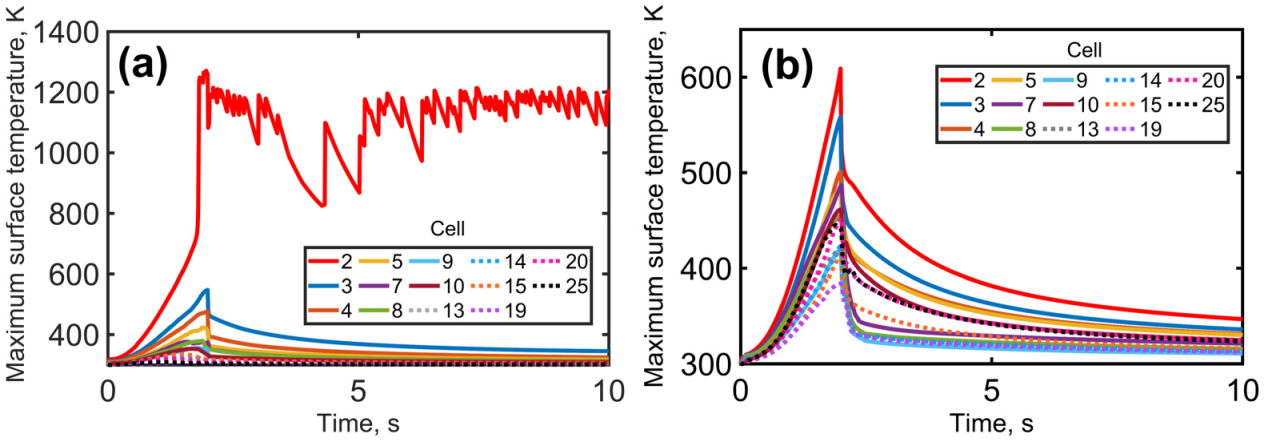

Figure 2.11 Time evolution of the cell maximum surface temperature to see the influence of the combustion model and TR propagation: (a) both venting and combustion models active, (b) venting process only (combustion model disabled), reprinted from [47] with IOP Publishing permissions

Mishra *et al.* [47] studied the impact of vented gases on the thermal runaway propagation in a pack of 18650 cylindrical cells with reactive fluid models. The cells are enclosed in a module filled with air. In the simulation, one cell is designated as "trigger cell" which releases hot gases for two seconds. The reactive simulation uses a non-premixed combustion model. The vented gas composition is taken from Golubkov *et al.* [34] for a LCO 18650 battery. The maximum temperature as a function of time is plotted for every cell except the triggered one (cell n°1) in Figure 2.11. TR spreads to neighbouring cells like cell 2 when the combustion model is active, but no propagation occurs when combustion model is disabled in the simulation. A key conclusion reveals that case failure in one cell, resulting in gas release, significantly increases thermal runaway risk in neighbouring cells due to direct exposure to hot vented gases. Furthermore, the temperatures reached by many cells are sufficient to trigger thermal runaway, but they are rather predicted to rapidly cool down. Further studies are needed to investigate these inconsistencies and to fill the knowledge of the risks of fire propagation.

In order to maintain reasonable computational costs while including more chemical reactions and chemical species, Cellier *et al.* [45] developed an analytically reduced chemical mechanism. The San Diego Mechanism [55] (57 chemical species and 268 reactions) was chosen as the base mechanism. Five reduction cases are chosen to represent a variety of events found in battery fires: one 0D isochoric auto-ignition and four 1D premixed laminar flame speed simulations at various equivalence ratios[2] and temperatures (300 K and 1000 K). After the reduction, 24 species and 93 reactions remained and showed a 5.5 fold reduction in computational time for a stoichiometric laminar flame in comparison to the source mechanism. The authors then used the reduced mechanism to run a 3D LES simulation of the combustion of vented gases using the CFD solver AVBP. For the model, they used the gas composition and parameters from a NMC Li-ion cell obtained by Golubkov *et al.* [34] as boundary conditions. Venting is only modelled outside the cell by injecting the gas mixture into the surrounding environment by using a mass flow inlet with predefined turbulence to model the turbulent flow through the cap. The ignition was induced using tiny spheres of hot temperatures, one sphere per vent hole, located 15 mm away from their respective outlet and active during 4 ms to represent a forced ignition caused by sparks or ejected incandescent matter. Two cap configurations were investigated: a five-hole and a three-hole geometry. The overall mass flow rate remains constant ($\dot{m} = 0.506\,\mathrm{g.s^{-1}}$ [45]) across both configurations, with the total mass flow divided equally among all vents in the geometry. The results of these different venting configurations are showed in Figure 2.12a and Figure 2.12b respectively. The first presents an attached flame without residual flammable gases, whereas the second shows a flame extinguishing 20 ms after ignition and unburnt gases accumulating outside the cell. The outlet velocity for each vent for the three-hole configuration is greater than for the first configuration, which prevents the flame stabilisation near the vent. The five-hole configuration generated more amount of heat. Therefore, the number of vent holes have a significant impact on the flame stability. In addition, the amount of heat released can reduce the risk of having unburnt gas which can ignite outside the cell.

[2]Combustion parameter noted ϕ, is defined as the ratio of actual fuel-oxidant ratio to the fuel-oxidant ratio for a stoichiometric reaction

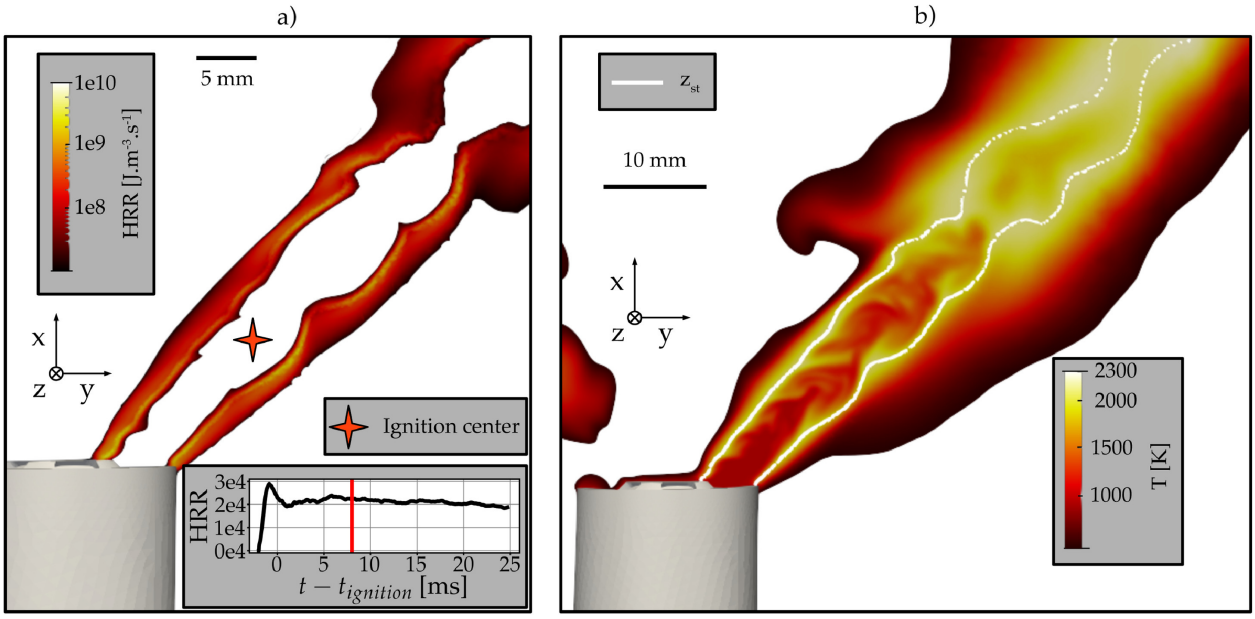

(a) Reactive flow simulation of the five holes geometry

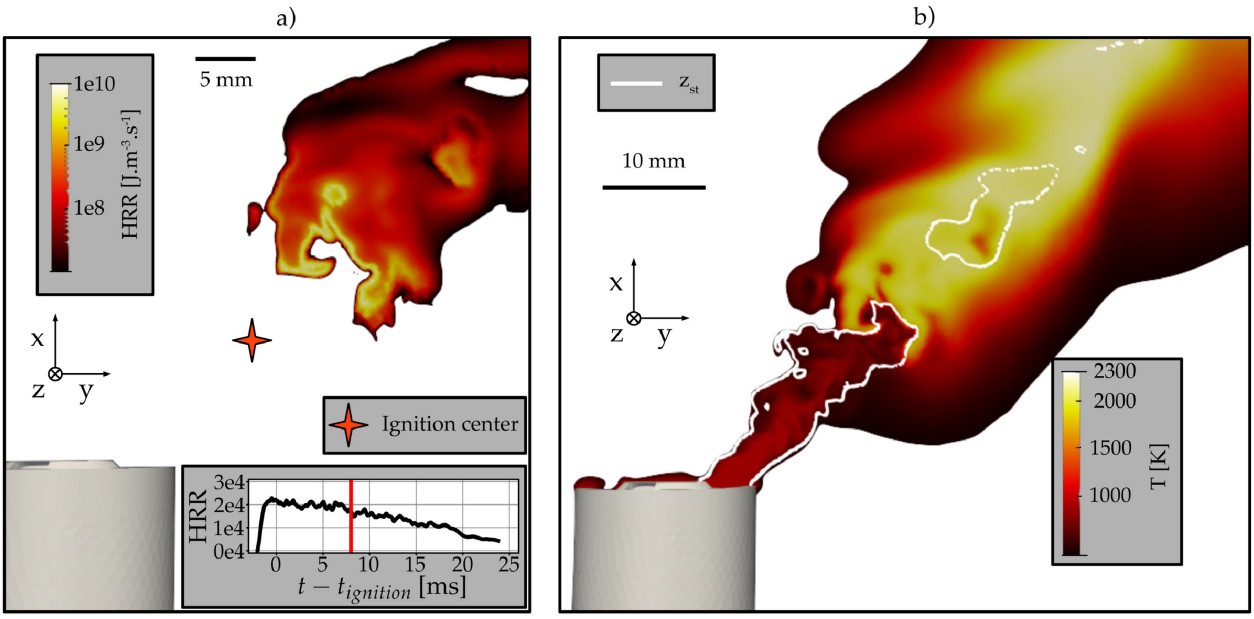

(b) Reactive flow simulation of the three holes geometry

Figure 2.12 Reactive flow simulation depending of the number of holes geometry : Cut view of the heat release rate field on the left, cut view of the temperature field on the right, reproduced from [45] with Elsevier permission

2.3 Knowledge gap and objectives of the research project

The literature review illustrates the complexity of numerical modelling of thermal runaway to study combustion reactions with turbulent flows and the ignition behaviour of the mixture emitted by a cell. The modelling is divided into three main domains : the venting phase, combustion of vented gas and the use of chemical kinetics mechanisms.

Current venting process models rely on simplified approaches, typically using the ideal gas law and isentropic flow equations through the vent. More advanced research attempts to simulate the flow dynamics through the precise geometric configuration of battery cell tops, which differ across commercial designs.

The review also highlights the need to explore the combustion models (species transport, non premixed combustion and partially premixed combustion) with RANS approach, which are available in commercial solvers. Despite each model possessing distinct advantages and limitations, a comprehensive comparative analysis of their performance in battery combustion scenarios remains unexplored. Furthermore, combustion model studies often lack comprehensive reporting of critical fire safety parameters, such as heat-release rate and specific ignition conditions.

For gas-phase combustion reactions, the literature review shows that the simplified chemical mechanism of Cellier *et al.* [45] makes it possible to concentrate on the main species released by the cell while reducing simulation costs. As the inert mixture must be taken into account for lithium metal battery modules, no study has observed the effect of an inert mixture in a module where a cell emits a flammable gas.

In light of the literature review, the aim of this thesis is to propose **a numerical model of turbulent gas-phase combustion based on geometry configuration relevant to lithium metal battery modules, and capable of studying the ignition behaviour of the mixture emitted by the cell in the presence of an inert mixture**.

Based on the main objective, the various sub-objectives are:

- Expose the differences between the numerical combustion models available in Fluent by studying the auto-ignition conditions of the gas mixture in the presence of inert species, the formation of the flame, and the resulting heat release rate.
- Conduct a sensitivity analysis using a numerical model to identify key parameters that influence the auto-ignition conditions of the mixture released from the cell.

CHAPTER 3 METHODOLOGY

This section gives the steps leading to the development of a numerical model dedicated to gas-phase combustion adapted to a LMP battery module geometry. The characteristics and assumptions of the combustion models available in Fluent are presented. The choices made regarding the solver selection and the boundary conditions applied to the model are also discussed.

3.1 Governing equations and closure models

3.1.1 RANS equations for reactive flows

Reynolds decomposition consists in decomposing any physical quantity v into a mean $\overline{v}$ and a fluctuating component v' such that $v = \overline{v} + v'$ [26]. When the density is not constant (for compressible and/or reactive mixtures), the Favre averaging method is chosen for a physical quantity v and a fluctuating component v'' by the following expression:

$$\tilde{v} = \frac{\overline{\rho v}}{\overline{\rho}} \text{ with } v = \tilde{v} + v'' \tag{3.1}$$

By analogy with the Reynolds averaging method, the quantity v is divided into a mean $\tilde{v}$ and a fluctuating component v''. The Favre averaged, mass conservation, momentum and energy equations take the following form:

$$\frac{\partial \overline{\rho}}{\partial t} + \nabla \cdot (\overline{\rho}\tilde{\boldsymbol{u}}) = 0 \tag{3.2}$$

$$\frac{\partial (\overline{\rho}\tilde{\boldsymbol{u}})}{\partial t} + \overline{\rho}(\tilde{\boldsymbol{u}} \cdot \nabla \tilde{\boldsymbol{u}}) = -\nabla \overline{p} - \overline{\rho}\boldsymbol{g} + \nabla \cdot \overline{\boldsymbol{\tau}} + \nabla \cdot (\widetilde{-\overline{\rho}\boldsymbol{u''}\boldsymbol{u''}}) \tag{3.3}$$

$$\frac{\partial \overline{\rho}}{\partial t}\left(\tilde{E} + \frac{\tilde{\boldsymbol{u}}^2}{2}\right) + \nabla \cdot \left(\overline{\rho}\tilde{\boldsymbol{u}}\left(\tilde{h} + \frac{\tilde{\boldsymbol{u}}^2}{2}\right)\right) = \overline{\rho}\tilde{\boldsymbol{u}} \cdot \boldsymbol{g} + \nabla \cdot \left((\overline{\lambda} + \lambda_T)\nabla \tilde{T} - \sum_i \tilde{h}_i \overline{\boldsymbol{J_i}}\right) \tag{3.4}$$

where ρ is the mass density, $\boldsymbol{u}$ is the velocity vector, p and T are the pressure and temperature respectively, $\rho\boldsymbol{g}$ is the gravitational body force, E is the energy. The last two terms on the right-hand side of Eq. (3.3) require modelling to achieve closure. $\boldsymbol{\tau}$ is the viscous stress tensor and the Reynolds stress tensor $-\rho\boldsymbol{u''}\boldsymbol{u''}$ is modelled by the Boussinesq hypothesis is discussed later with the turbulence model chosen [56, 57]. λ and λ_T are respectively the laminar and turbulent thermal conductivity, the latter is defined according the turbulence model used. h_i and $\boldsymbol{J_i}$ are the enthalpy and the diffusion flux of species i respectively. The diffusion flux $\boldsymbol{J_i}$ is defined as:

$$\overline{\boldsymbol{J_i}} = -\overline{\rho}\overline{D}_{i,m}\nabla \tilde{Y}_i \tag{3.5}$$

with $D_{i,m}$ the mass diffusion coefficient, Y_i the mass fraction of species i

Enthalpy is defined, using the ideal gas assumption, as:

$$h = \sum_i h_i Y_i \text{ with } h_i = h_i^0(T_{\text{ref}}) + \int_{T_{\text{ref}}}^{T} C_{p,i}\, dT \tag{3.6}$$

with $C_{p,i}$ the heat capacity at constant pressure of species i and $h_i^0(T_{\text{ref}})$ the standard enthalpy of formation of species i at the reference temperature T_{ref}.

The compressibility of the mixture is taken into account by calculating the density using the compressible formulation of the ideal gas law adapted to the Reynolds averaging method:

$$\overline{\rho} = \overline{\left(\frac{pM}{RT}\right)} \simeq \frac{\overline{p}\,\overline{M}}{R\tilde{T}} \tag{3.7}$$

where p is the static local pressure, R is the universal gas constant ($R = 8.314\,\text{J.K}^{-1}\text{.mol}^{-1}$) and M is the molecular mass of the gas mixture.

Turbulence is solved by the two-equation Realizable $k-\varepsilon$ model [58,59]. This model considers the eddy viscosity as a scalar computed as a function of the Favre-averaged turbulent kinetic energy $\tilde{k}$ and Favre-averaged turbulent kinetic energy dissipation rate $\tilde{\varepsilon}$. Therefore two additional conservation equations are solved:

$$\frac{\partial(\overline{\rho}\tilde{k})}{\partial t} + \nabla\cdot(\overline{\rho}\tilde{k}\tilde{\boldsymbol{u}}) = \nabla\cdot\left[\left(\overline{\mu} + \frac{\mu_t}{\sigma_k}\right)\nabla\tilde{k}\right] + G_k - \overline{\rho}\tilde{\varepsilon} + Y_m \tag{3.8}$$

$$\frac{\partial(\overline{\rho}\tilde{\varepsilon})}{\partial t} + \nabla\cdot(\overline{\rho}\tilde{\varepsilon}\tilde{\boldsymbol{u}}) = \nabla\cdot\left[\left(\overline{\mu} + \frac{\mu_t}{\sigma_\varepsilon}\right)\nabla\tilde{\varepsilon}\right] + \overline{\rho}C_1 S\tilde{\varepsilon} - C_2\overline{\rho}\frac{\tilde{\varepsilon}^2}{\tilde{k} + \sqrt{\nu\tilde{\varepsilon}}} \tag{3.9}$$

with

$$C_1 = \max\left[0.43, \frac{\eta}{\eta+5}\right] \text{ with } \eta = S\frac{\tilde{k}}{\tilde{\varepsilon}} \text{ and } S = \sqrt{2S_{ij}^2}\,, S_{ij} = \frac{1}{2}\left(\frac{\partial\tilde{\boldsymbol{u}}_{\boldsymbol{i}}}{\partial x_j}\frac{\partial\tilde{\boldsymbol{u}}_{\boldsymbol{j}}}{\partial x_i}\right) \tag{3.10}$$

where G_k is the production of turbulence kinetic energy due to the mean velocity gradients defined as $G_k = \mu_t S^2$, S_{ij} is the strain rate and Y_m is the contribution of the fluctuating dilatation in compressible turbulence to the overall dissipation rate modelled in the literature [60]. σ_k and σ_ε are respectively the turbulent Prandtl number for turbulent kinetic energy and turbulent kinetic energy dissipation rate. C_1 and C_2 are two constants, experimentally determined in the literature [26, 61]. μ_t is the eddy viscosity modelled by the following equation:

$$\mu_t = \overline{\rho}C_\mu\frac{\tilde{k}^2}{\tilde{\varepsilon}} \tag{3.11}$$

The Realizable $k-\varepsilon$ turbulence model has a formulation that meets the mathematical constraints of the Reynolds stresses. Indeed, the formulation allows the constant C_μ to be varied as a function of the properties of the surrounding flow. Details of the calculation of the constant and the approximations used are given in Appendix B.

Thanks to the modelling of the eddy viscosity, specific terms can be closed in equation (3.3) like the viscosity stress tensor $\overline{\boldsymbol{\tau}}$ and the Reynolds stresses tensor $-\overline{\rho}\widetilde{\boldsymbol{u''u''}}$ by using the Boussinesq hypothesis:

$$\overline{\boldsymbol{\tau}} = \overline{\mu}\left[\left(\nabla\tilde{\boldsymbol{u}} + (\nabla\tilde{\boldsymbol{u}})^T\right) - \frac{2}{3}(\nabla\cdot\tilde{\boldsymbol{u}})\boldsymbol{I}\right] \tag{3.12}$$

$$-\overline{\rho}\widetilde{\boldsymbol{u''u''}} = \mu_t\left[\left(\nabla\tilde{\boldsymbol{u}} + (\nabla\tilde{\boldsymbol{u}})^T\right) - \frac{2}{3}(\nabla\cdot\tilde{\boldsymbol{u}})\boldsymbol{I}\right] - \frac{2}{3}\overline{\rho}\tilde{k}\boldsymbol{I} \tag{3.13}$$

The Favre-averaged species transport equation is solved to predict the local mass fraction Y_i of each chemical species i in fluid regions using the equation below:

$$\frac{\partial(\overline{\rho}\tilde{Y_i})}{\partial t} + \nabla\cdot(\overline{\rho}\tilde{\boldsymbol{u}}\tilde{Y_i}) = -\nabla\cdot\overline{\boldsymbol{J_i}} - \nabla\cdot(\overline{\rho}\widetilde{\boldsymbol{u''}Y_i''}) + \overline{R_i} \tag{3.14}$$

where Y_i is the mass fraction of species i, $\boldsymbol{u}$ the velocity vector of diffusing species, $\boldsymbol{J_i}$ the diffusion flux of species i (cf Eq. (3.5)). $\overline{R_i}$ represents the mean chemical source term of species i which is closed by the combustion model chosen. $\overline{\rho}\widetilde{\boldsymbol{u''}Y_i''}$ is the turbulent flux of species mass fraction modelled by a gradient-diffusion approximation:

$$\overline{\rho}\widetilde{\boldsymbol{u''}Y_i''} = -\frac{\mu_t}{Sc_t}\nabla\tilde{Y_i} \tag{3.15}$$

where $Sc_t = 0.7$ is the turbulent Schmidt number. The species transport equation (3.14) takes into account the mixing of species, diffusion phenomena and the source term of chemical reactions. The formulation of $\overline{R_i}$ depends on the choice of numerical combustion model discussed in the following section.

3.1.2 Turbulent combustion models

Three combustion models are available in Fluent to close the reaction source term $\overline{R_i}$. Table 3.1 shows the main assumptions for each of the numerical models used in this thesis. As the mixture of inert species needs to be taken into account in addition to fuel and air, the models presented below are capable of handling 3 distinct mixtures. They are organised into three main categories: Species Transport, Non Premixed Combustion and Partially Premixed Combustion.

Table 3.1 General assumptions of the main combustion models available on Fluent integrating 3 distinct mixtures

Combustion models	Main hypothesis
Species Transport - Eddy Dissipation Concept	• Combustion reactions on small turbulent scales modelled as constant pressure reactors
Non Premixed Combustion - Chemical Equilibrium[2]	• Flamelet model (thin flames) • Thermochemical composition reduced to a mixture fraction variable • Fast chemistry reaction kinetics • TCI[1] modelled by a PDF
Partially Premixed Combustion - Chemical Equilibrium[2]	• Flamelet model (thin flames) • Thermochemical composition reduced to a mixture fraction and progress variables • Fast chemistry reaction kinetics • TCI[1] modelled by a PDF

Species Transport model

This model can be used to describe multiple chemical reactions, considered as volumetric reactions, taking place simultaneously in a fluid region. One approach like the Eddy Dissipation Concept (EDC) model enables to model $\overline{R_i}$. This approach offers the benefit of integrating detailed chemical mechanisms for turbulent flows, but suffers from the shortcoming of being computationally expensive.

[1]Turbulence Chemistry Interaction

[2]Chemical reactions are considered to be faster than the other physical processes, the concentrations of the species reach a thermodynamic equilibrium, and the temperature of the system stabilises at a final value

The EDC model assumes that reaction rates are controlled by the turbulent mixing of chemical species [62]. It considers that reactions take place on small turbulent scales occupying a volume fraction noted κ. Combustion at these scales takes place in the same conditions as in a constant-pressure reactor, with the initial composition and temperature conditions given by $\widetilde{\boldsymbol{Y}}$ and $\tilde{T}$. The reactions take place on a time scale τ^* and are numerically integrated into an ODE solver. The reaction source term in Eq. (3.14) is described by the following expression:

$$\overline{R_i} = \overline{\rho}\kappa\frac{Y_i^* - \widetilde{Y_i}}{\tau^*} \tag{3.16}$$

where ρ is the mass density, Y_i^* the mass fraction of chemical species i at fine scales after a reaction time τ^*. The time integration scale τ^* is defined as:

$$\tau^* = C_\tau\sqrt{\frac{\overline{\nu}}{\tilde{\varepsilon}}} \tag{3.17}$$

where ν is the kinematic viscosity, ε the dissipation rate of turbulent kinetic energy, and C_τ a constant [63].
The EDC model defines the volume fraction of reactions at small turbulence scales as:

$$\kappa = \frac{\xi^{*2}}{1-\xi^{*3}} \text{ with } \xi^* = C_\xi(\frac{\nu\,\tilde{\varepsilon}}{\tilde{k}^2})^{1/4} \tag{3.18}$$

with ξ^* the length scale, k the turbulent kinetic energy and C_ξ a constant [63].

The EDC Partially Stirred Reactor model is a variant of the standard EDC model [64, 65]. It defines the volume fraction κ and the time scale τ^* by:

$$\kappa = \frac{t_\text{c}}{t_\text{c}+t_\text{mix}} \text{ with } t_\text{c} = \max\left(\frac{\overline{\rho}\tilde{Y}_i}{R_i(\widetilde{\boldsymbol{Y}},\tilde{T})}\right) \text{ and } t_\text{mix} = C_\text{mix}\frac{\tilde{k}}{\tilde{\varepsilon}} \tag{3.19}$$

$$\tau^* = \min(t_\text{c}, t_\text{mix}) \tag{3.20}$$

where t_c is the chemical time scale, t_mix is the mixing time scale where C_mix can be a constant value or dependent of the characteristics of the turbulent flow [63, 65].

Non Premixed Combustion model

The Non-Premixed Combustion (NPC) model uses the notion of mixture fraction to model the behaviour of a non-premixed flame. The model assumptions include low Mach numbers with constant thermodynamic pressure, uniform specific heat capacities across all chemical species ($C_{p,i} = C_p$). Moreover, they add equal molecular diffusivities for all species ($D_{i,m} = D$), and a Lewis number of unity indicating no preferential diffusion ($Le = \frac{\lambda}{\rho C_p D} = 1$).

Under these assumptions and the hypothesis of infinitely fast chemistry, the thermochemical characteristics are reduced to a conserved scalar called the mixture fraction, which comes from the mixing fraction of the fuel. It refers more precisely to the local fraction of burnt and unburnt elements of the fuel mixture among all the other species present in the fluid region. It is defined by the following formula:

$$f = \frac{Z_i - Z_{i,\mathrm{Ox}}}{Z_{i,\mathrm{Fuel}} - Z_{i,\mathrm{Ox}}} \tag{3.21}$$

with Z_i the elemental mass fraction for element i, the subscripts Ox and Fuel correspond to the oxidant and the fuel streams respectively [25].

This formulation avoids the need to solve the transport equation for each species in the mixture, unlike the Species Transport model. The species transport equation is reduced to a conservation equation for f. As the mixture fraction is conserved, no reaction source term is present in this equation.
Non Premixed Combustion model solves a transport equation for the mixture fraction f and its variance $\widetilde{f'^2} = \widetilde{(f - \tilde{f})^2}$:

$$\frac{\partial \overline{\rho} \tilde{f}}{\partial t} + \nabla \cdot (\overline{\rho} \tilde{\boldsymbol{u}} \tilde{f}) = \nabla \cdot \left[\left(\frac{\overline{\lambda}}{\overline{C_p}} + \frac{\mu_t}{\sigma_t} \right) \nabla \tilde{f} \right] \tag{3.22}$$

$$\frac{\partial \overline{\rho} \widetilde{f'^2}}{\partial t} + \nabla \cdot (\overline{\rho} \tilde{\boldsymbol{u}} \widetilde{f'^2}) = \nabla \cdot \left[\left(\frac{\overline{\lambda}}{\overline{C_p}} + \frac{\mu_t}{\sigma_t} \right) \nabla \widetilde{f'^2} \right] + C_g \mu_t (\nabla \tilde{f})^2 - \overline{\rho} C_d \frac{\tilde{\varepsilon}}{\tilde{k}} \widetilde{f'^2} \tag{3.23}$$

where C_p, λ and σ_t are the mixture heat specific capacity, mixture thermal conductivity and turbulent Prandtl number respectively. C_g and C_d are constants defined in the literature [66]. The variance $\widetilde{f'^2}$ is used in the closure model for the chemistry-turbulence interaction (TCI) [26].

As the inert mixture in addition to fuel and air mixtures must be considered in the work presented here, a secondary mixture fraction is introduced. The sum of the three mixture fractions (fuel, air and inert mixture considered as second stream) in the domain must follow the following equality:

$$f_{\text{fuel}} + f_{\text{ox}} + f_{\text{sec}} = 1 \tag{3.24}$$

where f_{fuel} is the fuel mixture fraction, f_{ox} is the oxidant mixture fraction and f_{sec} is the secondary mixture fraction. If the mixture fraction space is represented, it takes the form of a triangular plane as shown in Figure 3.1a. Only the points contained in this plane respect the equality (3.24). Valid values for f_{fuel} and f_{sec} are in the OBC triangle as illustrated in Figure 3.1b.

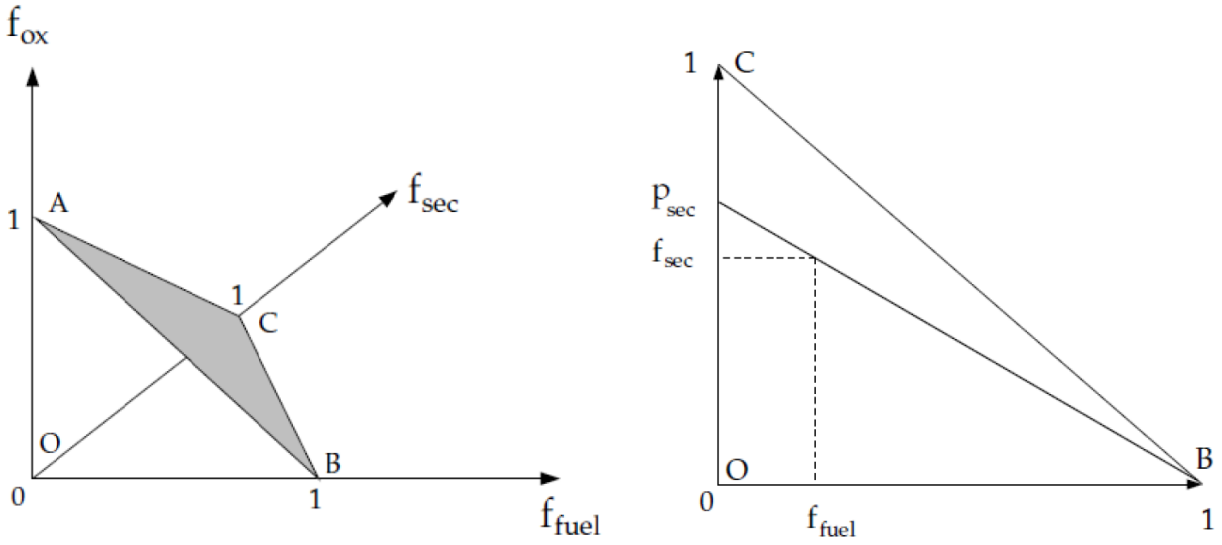

(a) Triangular validity domain in the space of mixture fractions

(b) Dependency relationship between f_{fuel} and f_{sec}

Figure 3.1 Relationship between mixtures fractions with a second stream, reproduced from [63]

Fluent allows this triangle to be discretised by considering that f_{fuel} varies between 0 and 1 and f_{sec} is deduced from the equation using the normalized secondary fraction p_{sec} [63]:

$$f_{\text{sec}} = p_{\text{sec}}(1 - f_{\text{fuel}}) \tag{3.25}$$

p_{sec} is obtained from the intersection of the straight line with the y-axis of f_{sec} as shown in Figure 3.1b. The transport equations for the secondary mixture fraction f_{sec} remain valid by substituting $\widetilde{f_{\text{sec}}}$ by $\tilde{f}$ in Eq. (3.22). $\widetilde{p_{\text{sec}}}$ is calculated in the expression (3.22) and $\widetilde{p'_{\text{sec}}{}^2}$ is computed by replacing $\widetilde{p_{\text{sec}}}$ by $\tilde{f}$ in Eq. (3.23). The calculation of the variances $\widetilde{p'_{\text{sec}}{}^2}$ and $\widetilde{f'_{\text{sec}}{}^2}$ are similar to a first approximation [63].

To apply a combustion model with three streams mentioned above, a closure of the turbulence model describing the TCI is necessary via the assumed-shape probability density function (PDF) approach. All the instantaneous thermochemical quantities (mass fraction, temperature, and density) depend on the mixture fraction f and the secondary mixture fraction f_{sec} under the assumption of chemical equilibrium. For adiabatic systems, the relationship to describe the heat loss/gain effect is given by:

$$\Phi_i = \Phi_i(f_{\text{fuel}}, f_{\text{sec}}) \tag{3.26}$$

where Φ_i refers to mass fraction, temperature or density. The PDF approach, which describes the fluctuating values of the mixture fraction in turbulent flow, is used to calculate the mean values of thermochemical quantities. Average quantities are computed as:

$$\widetilde{\Phi_i} = \int_0^1 \int_0^1 \Phi_i(f_{\text{sec}}, p_{\text{sec}}) P_1(f_{fuel}) P_2(p_{sec})\, df_{fuel}\, dp_{sec} \tag{3.27}$$

where P_1 and P_2 are the PDF functions for f_{fuel} and p_{sec} respectively. The quantities f_{fuel} and p_{sec} are assumed to be statistically independent such that $P(f_{fuel}, p_{sec}) = P_1(f_{fuel})P_2(p_{sec})$. The assumed-shapes of PDF functions P_1 and P_2 are described by a β-function computed using the mixture fractions and their variances. Calculations of these thermochemical quantities $\widetilde{\Phi_i}$ are pre-processed by Fluent and then compiled in a table [63].

Partially Premixed Combustion model

Fluent features 3 Partially Premixed Combustion (PPC) sub-models (*Chemical Equilibrium*, *Steady Diffusion Flamelets* and *Flamelet Generated Manifold*) [63]. As for the Non Premixed Combustion model, only the Chemical Equilibrium sub-model allows a second stream to be modelled with its mixture fraction f_{sec}. The main assumptions of this model are that the premixed flame front is infinitely thin, with burnt products behind and unburnt reactants in front of the flame front. The composition of the products consumed is modelled on the assumption of chemical equilibrium. The flame front is indicated by the reaction progress variable c varying between 0 (position of the unburnt fuel/oxidant mixture) and 1 (position of the burnt products) [25]. It is defined as a normalized sum of the product species mass fractions:

$$c = \frac{\sum_k \alpha_k (Y_k - Y_k^u)}{\sum_k \alpha_k (Y_k^{eq} - Y_k^u)} = \frac{Y_c}{Y_c^{eq}} \tag{3.28}$$

where α_k are constants chosen to increase c gradually in the flame front. The subscripts u correspond to the unburnt reactants and eq to the chemical equilibrium. In addition to solving the transport equations for the mixture fraction and its variance, this model solves a transport equation for the mean reaction progress variable $\tilde{c}$ to determine the position of the flame front [67] in the non-normalized expression:

$$\frac{\partial \overline{\rho} \widetilde{Y_c}}{\partial t} + \nabla \cdot (\overline{\rho} \tilde{\boldsymbol{u}} \widetilde{Y_c}) = \nabla \cdot \left[\left(\frac{\overline{\lambda}}{\overline{C_p}} + \frac{\mu_t}{\sigma_t} \right) \nabla \widetilde{Y_c} \right] + \overline{S_{Y_c}} \tag{3.29}$$

where S_{Y_c} is a source term modelled in a flamelet library [63]. Similar to the Non Premixed Combustion model, mean thermochemical quantities $\widetilde{\Phi}$ are computed by considering the PDF of the reaction progress variable and those of the two mixture fractions f_{fuel} and p_{sec}:

$$\widetilde{\Phi} = \int_0^1 \int_0^1 \int_0^1 \Phi_i(f_{\text{fuel}}, p_{\text{sec}}, \tilde{c}) P(f_{\text{fuel}}, p_{\text{sec}}, \tilde{c}) \, df_{\text{fuel}} \, dp_{\text{sec}} \, dc \tag{3.30}$$

In the thin flame front approximation, this equation becomes:

$$\widetilde{\Phi} = \tilde{c} \int_0^1 \Phi_b(f_{\text{fuel}}, p_{\text{sec}}) P(f_{\text{fuel}}, p_{\text{sec}}) \, df_{\text{fuel}} \, dp_{\text{sec}} \tag{3.31}$$

$$+(1 - \tilde{c}) \int_0^1 \Phi_u(f_{\text{fuel}}, p_{\text{sec}}) P(f_{\text{fuel}}, p_{\text{sec}}) \, df_{\text{fuel}} \, dp_{\text{sec}} \tag{3.32}$$

where Φ_b and Φ_u refer to functions of burnt and unburnt mixtures respectively. The scalar Φ_b is calculated from the reaction involving the three mixture fractions (f_{fuel}, f_{ox} and f_{sec}) whereas Φ_u is computed from the same mixture without reacting it [63].

3.2 Module configuration and setup

3.2.1 Geometry description

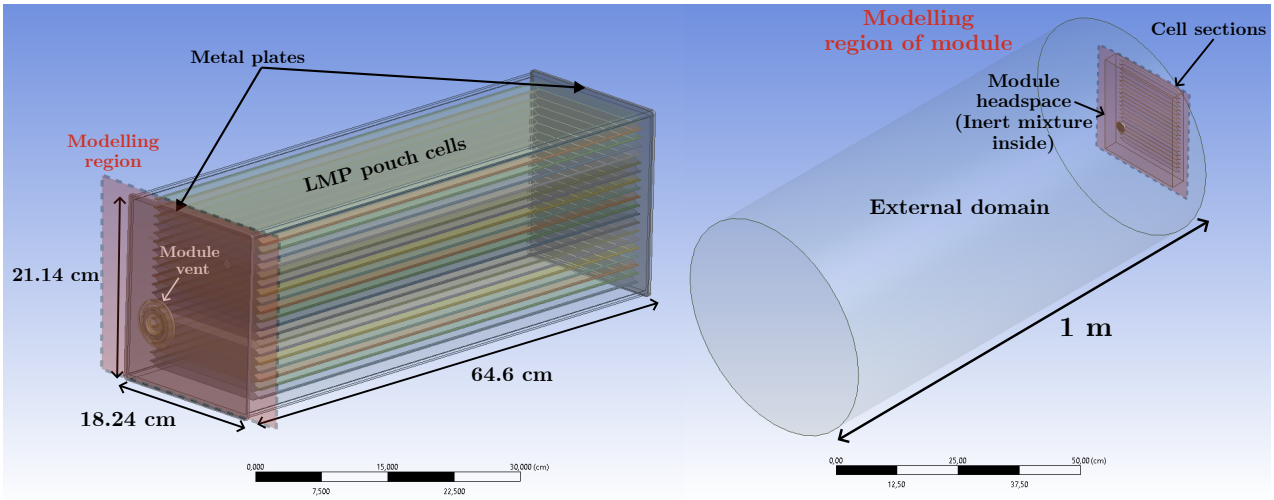

Figure 3.2 Dimensions of the 3D geometry of the battery module with the 20 pouch cells (**left**) and 3D modelling of the upper part of the module and the external domain (**right**)

One of the objectives of the numerical model is to describe reactive gas flow behaviour which is vented by a cell for a given module geometry. This geometry features 20 solid-electrolyte LMP® pouch cells contained in a metallic casing made of aluminium as shown by Figure 3.2.

Given that the objective of the model is to study only gas-phase combustion, the modelling of the condensed phase within the cells is not performed and the internal volume of the cells is not taken into account. For the development of the numerical model, the modelling focuses on the headspace of the module between the cells and the vent module, using the normal surface area of each pouch cell as shown by the red plane in the right Figure 3.2. The key area for studying gas-phase combustion is around the vent outlet. The module vent is modelled by a cylinder at the junction between the internal domain of the module and the external domain. Dimensions like height and diameter of the original vent are kept in the simplified version.

Moreover, solid parts (module metallic plates, aluminium casing, and metal parts of the vent cap) were subtracted from the global computational domain, leaving only the fluid region. One of the assumptions of the simplified model for modelling cell outgassing is that venting takes place uniformly along the normal surface and across the entire width of the cell.

To simulate the interaction between the gas mixture from the module and the surrounding air-filled environment, an additional cylindrical region has been added to describe the gas-phase combustion reactions of the fuel mixture in contact with air. The boundary conditions and dimensions of the computational domain are discussed in the next section.

3.2.2 Boundary conditions of the numerical model

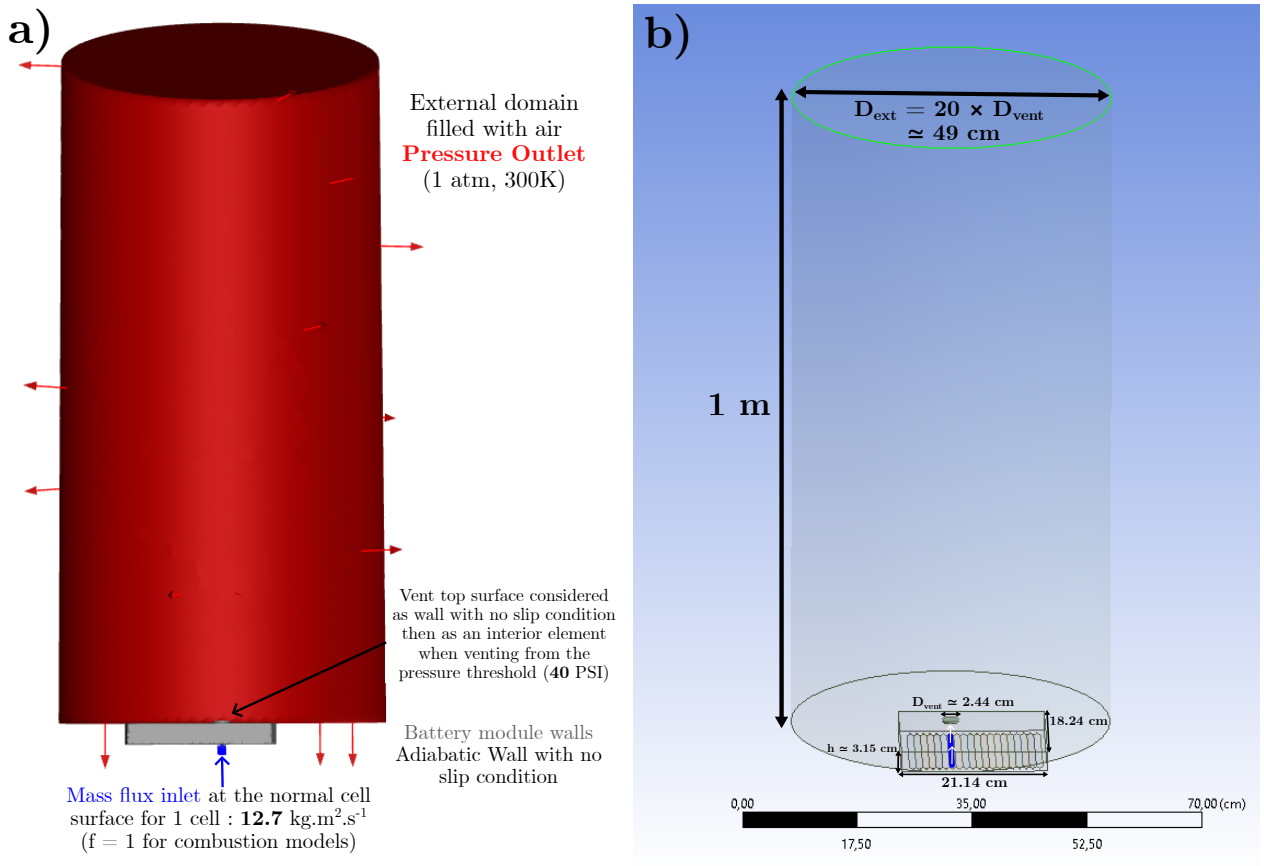

Figure 3.3 Boundary Conditions (**a**) and computational domain (**b**) for RANS simulations which represent the upper part of module and the external domain

Figure 3.3 shows the dimensions of the computational domain. Adiabatic walls with no slip condition have been assigned to the vent surfaces and module walls. Only the top surface of the vent changes its boundary condition, from no slip wall to an interior element, when the module's internal pressure reaches 40 PSI ($\simeq$ 2.76 bar). To model the cell venting, a gaseous mixture at high temperature (T_{inlet} = 950 K [45] and T_{inlet} = 1150 K [68] based on the literature) is added via a mass flux inlet located at the normal section of the cell. In the absence of experimental data for battery module, the idea is to have a mean outlet velocity from the cell similar ($v_{\text{outlet}} \approx 36\,\text{m.s}^{-1}$) to that of a Li-ion cell used in the article of Cellier [45]. This configuration is selected because it represents the most advanced numerical model in the literature for simulating the combustion of gases emitted by a Li-ion cell. For the cell degassing, the same mass flux per inlet area as used by Cellier *et al.* [45] is applied.

The configuration for each combustion model is presented below:

- **Species Transport** Model, the Stiff Chemistry solver is chosen. The backflow with pressure outlet condition is considered to be air at ambient temperature and pressure (300 K, 1 atm).

- **Non Premixed Combustion** model with Chemical Equilibrium, all physical quantities are computed into a PDF table. The fuel mixture fraction f_{fuel} is set to 1 at the mass flux inlet condition and 0 for the backflow condition. As the inert mixture is initially present in the module, the secondary mixture fraction f_{sec} is set to 1 in the module for initial conditions.

- **Partially Premixed Combustion** model with Chemical Equilibrium uses also the same conditions as the Non Premixed Combustion model. The progress variable c is set at 0 for the mass flux inlet condition.

The chemical composition of the mixture and the choice of chemical mechanism are discussed in the following section.

3.2.3 Gas phase chemical reactions model

Due to the lack of data specific to solid-state batteries with lithium metal anodes, the gas composition released from an LMP cell is estimated based on average gas mixture compositions experimentally measured from cylindrical LFP cells by Golubkov *et al.* [34, 35]. Following the study by Cellier *et al.* [45], a reduced chemical mechanism is chosen to limit the number of chemical species and reactions considered to concentrate on the main species (CO_2, CO, H_2, CH_4, and C_2H_4) in the gas mixture vented by the cell. This mechanism has the advantage of reducing the computational time required to solve the species transport equations. Given the initial presence of an inert mixture of argon and helium in the module, these two species are added to the mechanism. As Cellier *et al.* [45] developed their mechanism from the San Diego mechanism [55], which included these inert species, the reduced mechanism maintained their original physicochemical properties. A verification is made with Cantera to ensure that the reduced mechanism including the inert mixture worked correctly by comparing it with the original San Diego mechanism. For this comparison, two opposing jets of the gas mixture and the inert mixture are placed at low mass flow rates to allow sufficient time for the reactions to take place. This test allows a check to be made that there is no rise in temperature on contact with the two jets. The mechanism verification tests are available in Appendix C.

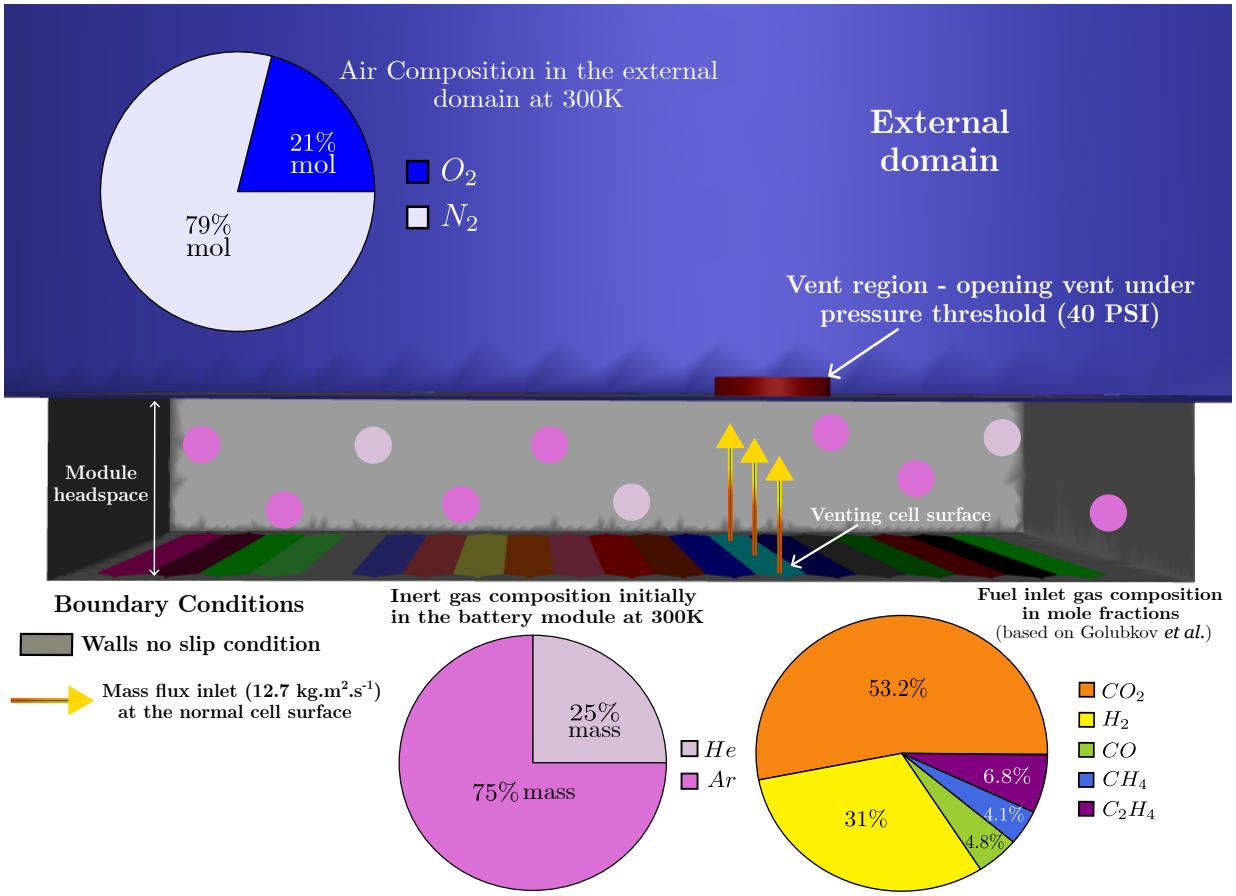

Figure 3.4 Chemical composition in the different fluid regions of the domain and boundary conditions

The chemical composition as boundary conditions is chosen about the venting of the gas mixture from the cell [35,45]. The inert mixture is initially added to the module in the above composition as shown in Figure 3.4.

3.2.4 Solver selection

CFD RANS simulations have been performed on ANSYS Fluent (release 2023 R2 and 2024 R2) [63, 69]. The CFD model, based on the finite volume method, solves the equations governing the turbulent flow of a compressible fluid through a vent. The pressure-based solver with a coupled pressure-velocity algorithm is used to improve the stability and accuracy of results. Realizable $k-\varepsilon$ turbulent model with scalable wall functions approach for the near-wall modelling is used. Recommended solver settings from the $k-\varepsilon$ model were used on Fluent to solve a compressible and turbulent flow through a vent [63]. An implicit second-order transient formulation is used to enhance stability and default values for spatial discretization are kept: first-order for the turbulent kinetic energy and turbulent dissipation rate, second order for momentum, density, pressure, energy, and the mean mixture fraction.

To reduce computational costs, the time-step size is adjustable. The initial time step size is set to 0.5 ms during the pressure build-up within the module, then switched to 10^{-4} s when the vent is opened until the internal pressure in the module returns to 120 kPa, then the time step is set to 10^{-3} s during the combustion process. Time step management and the venting with the boundary conditions change of the vent top surface are handled by a scheme implemented in Fluent and executed at every time step.

3.2.5 Mesh selection and mesh convergence analysis

The unstructured mesh approach with polyhedral elements was chosen for the numerical model. The mesh is generated using the ANSYS Workbench mesh utility. Polyhedral meshes are obtained by converting the tetrahedral into polyhedral elements using the mesh conversion option in ANSYS Fluent.

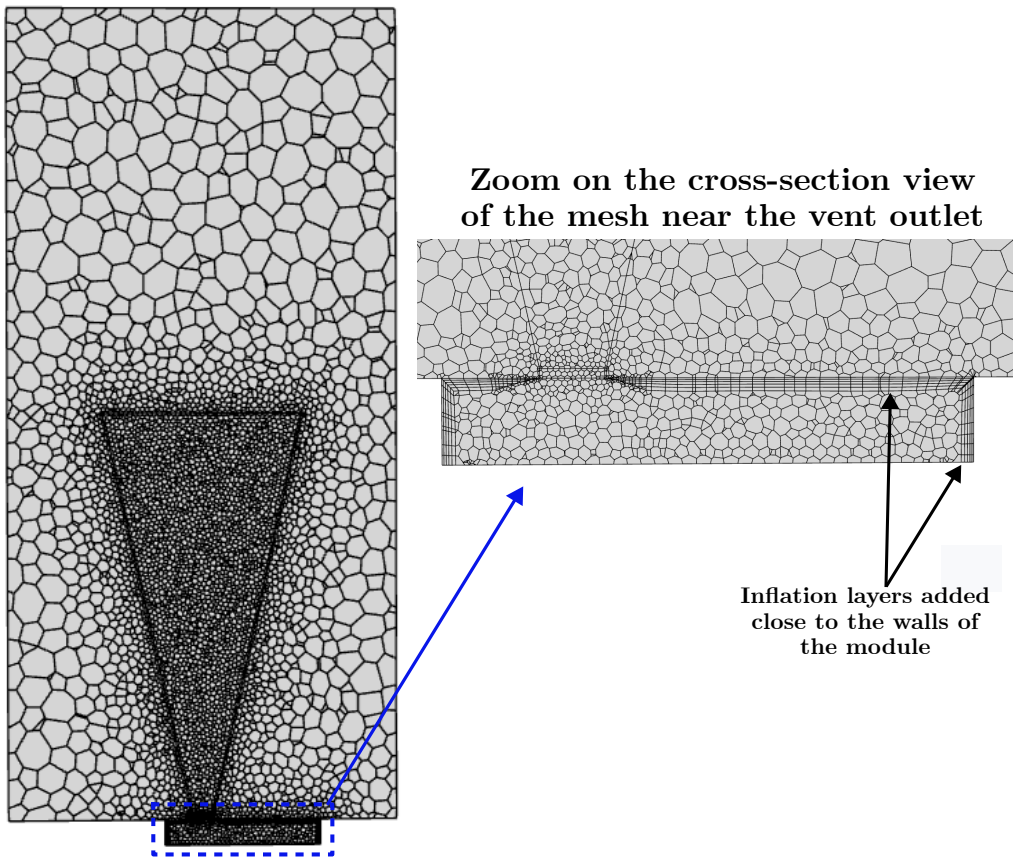

Figure 3.5 Mesh of the global computational domain with a cone-shaped vent outlet including the external domain and the upper part of the module

Polyhedral meshes have been chosen for the numerical model because they offer a number of advantages over tetrahedral meshes, according to the mesh sensitivity study by Li *et al.* [24]. Polyhedral elements have a lower overall number of meshes during mesh generation, faster convergence and better approximation of the gradients of physical quantities across the elements. In addition, polyhedral elements are less sensitive to mesh stretching and distortions than other meshing elements, which improves the numerical stability of the results obtained [47].

Mesh refinement was applied around the vent outlet region of the module as shown in Figure 3.5. A good discretisation of the mesh must be achieved in the regions close to the vent outlet where jet turbulence is present in order to obtain good convergence of the results. According to the mesh sensitivity analysis by Li *et al.* [24], a cone-type mesh at the vent outlet is useful in the external domain in order to obtain more information on the combustion reactions in the gas phase close to the vent.

A mesh convergence analysis was carried out for a coarse ($\approx 1.19 \times 10^5$), intermediate ($\approx 7.43 \times 10^5$), and fine meshes ($\approx 1.35 \times 10^6$) with polyhedral elements. The Non Premixed Combustion with Chemical Equilibrium model is used for this mesh convergence. In these simulations, the quality of the mesh on the Fluent meshing utility was checked by setting a minimum orthogonal quality value of 0.2 and a growth rate of 1.2. The venting temperature is set at $T_{inlet} = 1150$ K [68] to induce the ignition of the mixture while maintaining all other boundary conditions (cf. Figures 3.3, 3.4) and the time step is set at 1 ms for this mesh convergence. The analysis is based on the measurement of the maximum temperature in the external domain, the average vent outlet velocity measured on the upper section of the vent and the average internal pressure of the module.

Figures 3.6 and 3.7 show temporal evolutions in temperature, mean velocity and mean internal pressure for the three mesh grids.

The results of the three meshes show a low sensitivity for the evolution of the internal pressure of the module. For the evolution of the average outlet velocity, the sensitivity is more visible with the coarse mesh. The intermediate and fine meshes converge towards the same value.

Variations in external temperatures show a small sensitivity to the different meshes tested, but this remains low as shown in Figure 3.7. The maximum external temperature, when the steady state regime is reached ($t \geq 0.3$ s), has a variation of less than 4% between the highest and lowest values for the three meshes.

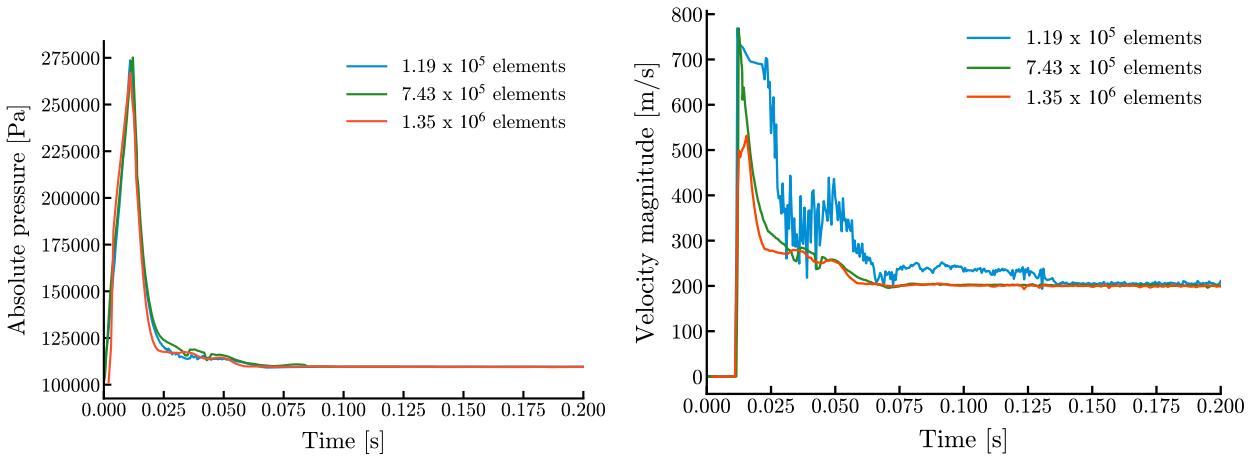

(a) Temporal evolution of the mean internal pressure of the module

(b) Temporal evolution of mean vent outlet velocity

Figure 3.6 Mesh convergence achieved for the three mesh grids on the evolution of internal module pressure and vent outlet velocity

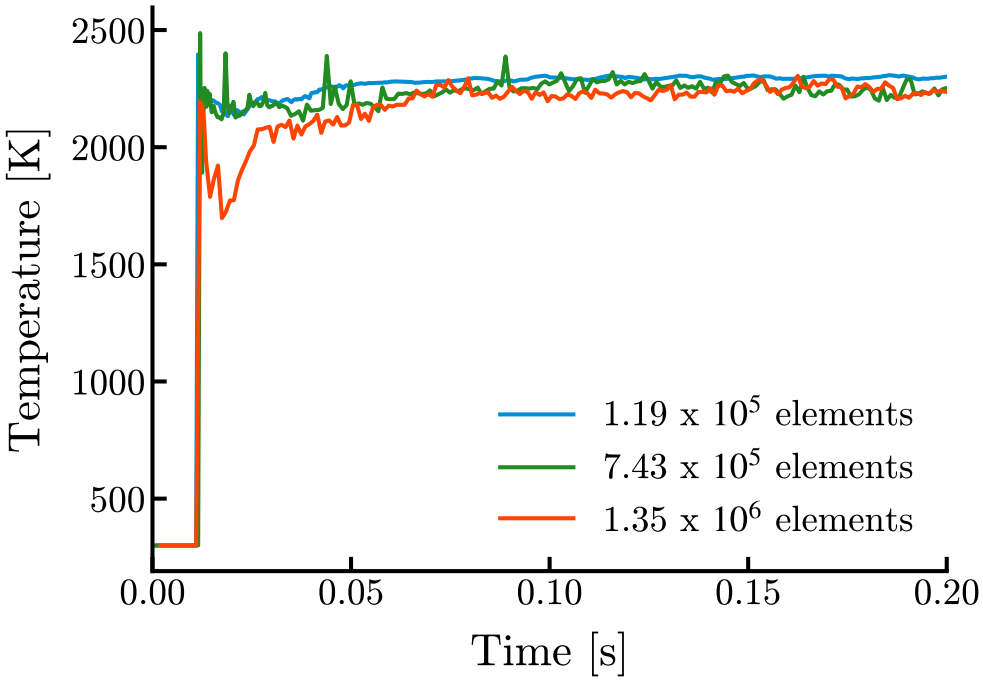

Figure 3.7 Mesh convergence achieved for the three mesh grids on the temporal evolution of maximum temperature in the external domain

3.3 Summary

In this section, the choice of modelling assumptions and the boundary conditions of the methodology are summarised. A critical analysis of these choices is presented here.

Firstly, the simplification of the vent geometry into a cylindrical shape facilitates the generation of the mesh of the fluid domain close to the vent. Indeed, the metal parts of the vent in the original geometry are not useful at first and generate small mesh sizes that can lead to convergence problems for the vent outlet velocity during venting. This also avoids significant computational costs with too many elements in the vent outlet region.

Table 3.2 summarises the various input parameters chosen for the numerical modelling. Regarding the boundary conditions, the chemical composition and constant mass flux rate are based on literature data. Choosing a constant outgassing mass flux does not represent a real case of venting cell, but it does simplify the modelling approach. Moreover, the assumption to keep the inlet temperature constant greatly simplifies the model. Cellier's chemical mechanism [45] works well for a gas mixture from a liquid electrolyte cell, but it will have to be adapted to the composition of the gases emitted by a solid electrolyte cell. Experimental data of LMP cells under thermal runaway are therefore required to optimise the boundary conditions of the numerical model.

In the absence of data on the composition of gases emitted by all-solid-state batteries, the boundary conditions are based mainly on gas composition data from models for cylindrical LiB cells in the literature. The aim is to be able to adjust the boundary conditions based on experimental data quickly, making the numerical model more accurate.

In the fluid domain, the flow diagram, shown in Figure 3.8, describes the coupling between the vent opening condition above a pressure threshold, turbulence, and combustion reactions in the gas phase. For each numerical model, each step is solved by the corresponding equations. Model output values include standard CFD physical parameters such as velocity, pressure, and temperature, as well as parameters specific to combustion models such as mixture fraction and heat release rate.

Table 3.2 List of various input parameters implemented for the numerical model

Parameter	Value	Reference
Mass flux rate	12.7 $kg.m^2.s^{-1}$	[45]
Venting temperature T_{inlet}	950 K or 1150 K	[45] for 950 K and [68] for 1150 K
Argon in the module	75 % mass.	Industrial partner
Helium in the module	25 % mass.	Industrial partner
Chemical composition of fuel mixture		
CO_2	53.2 % mol.	[35, 45]
H_2	31 % mol.	[35, 45]
C_2H_4	6.8 % mol.	[35, 45]
CO	4.8 % mol.	[35, 45]
CH_4	4.1 % mol.	[35, 45]

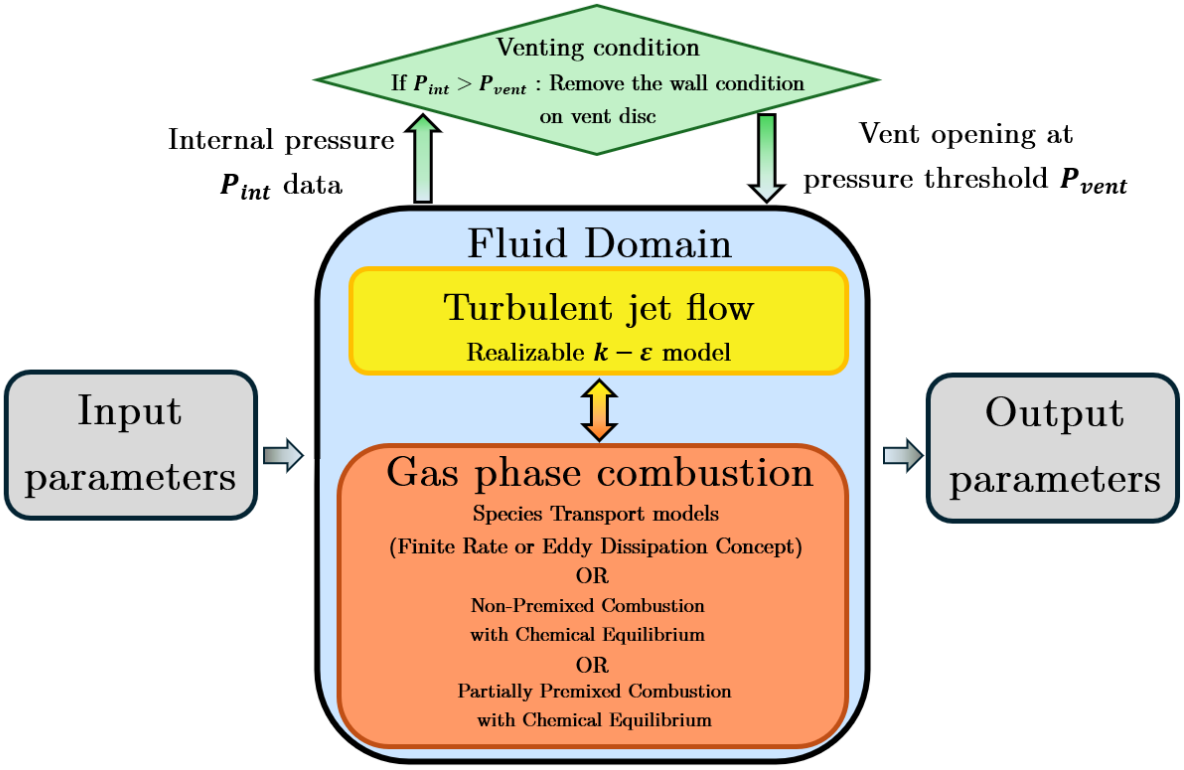

Figure 3.8 Flow chart for modelling turbulent combustion in the gas phase, including the venting phase

CHAPTER 4 RESULTS AND DISCUSSION

In this chapter, the results obtained with the three combustion models investigated will be compared. Then, a sensitivity analysis will be performed to highlight the effect of the input parameters that can influence the auto-ignition conditions of the gas mixture.

4.1 Comparison between turbulent combustion models

In this section, two venting gas temperatures obtained from articles by Cellier *et al.* ($T_{inlet,1} =$ **950** K [45]) and by Liao *et al.* ($T_{inlet,2} =$ **1150** K [68]) will be used as input to evaluate three different combustion models (EDC model with Species Transport, Non Premixed Combustion with Chemical Equilibrium (NPC) and Partially Premixed Combustion with Chemical Equilibrium (PPC)). This comparison is conducted on a mesh with 1.35×10^6 polyhedral elements. The goal is to compare the main differences obtained between the numerical models on the auto-ignition conditions of the gas mixture in the presence of inert species in the module. The analysis will focus on the auto-ignition delay and the shape of the flame, if present. The heat release rate for each model will be studied to see the auto-ignition behaviour of the gas mixture. In addition, a comparison of performance in terms of calculation time will be presented.

4.1.1 Pressure build-up in the module and venting condition

Figure 4.1 shows the temporal evolution of the internal pressure of the module and the mean outlet velocity at 1150 K for each model. The three models show a similar evolution in the mean internal pressure of the module as a function of time. The pressure profiles for the three models remain similar in the steady state regime ($t \geq 0.3$ s) with less than 2% variation between the curves. For the Non-Premixed Combustion and Partially Premixed Combustion models, the vent tends to open earlier than for the EDC model. This can be explained by variations in the handling of gas transport and mixing effects between the models. Due to their incorporation of diffusion and fluid interaction phenomena, the NPC and PPC models can simulate temporary gas accumulation, resulting in a more rapid pressure peak compared to the EDC model. The EDC model facilitates fast mixing and redistribution of injected gases throughout the module, which mitigates localized pressure concentrations and consequently shifts vent opening.

The build-up of internal pressure in the module has an influence on the venting conditions, especially on the evolution of the gas velocity at the vent outlet. Figure 4.1b shows the

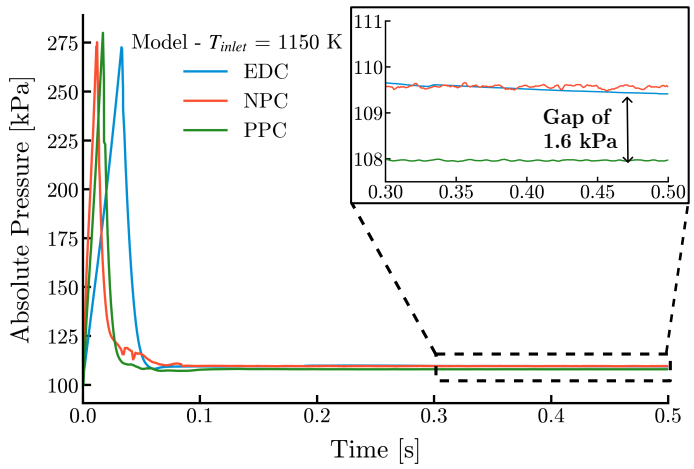

(a) Internal pressure in the module

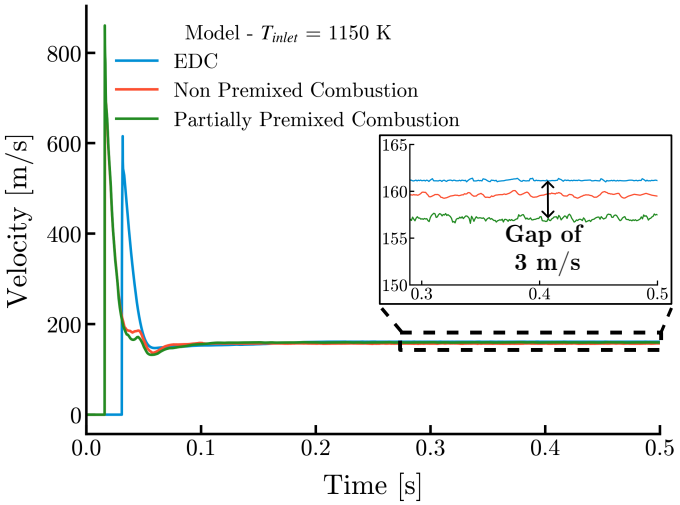

(b) Mean outlet velocity

Figure 4.1 Comparison of the temporal evolution of the mean internal pressure in the module and the mean outlet velocity for an inlet temperature at 1150 K for each model

evolution of the mean outlet velocity at the vent for the models. This value is measured by taking the average value over the top section of the vent. The three models show a similar evolution in the average outlet velocity with a peak indicating the vent opening under the pressure threshold. The difference of 3% in velocity profiles in the steady state regime between the models is due to their different approaches to turbulence-chemistry interaction. The NPC and PPC models feature enhanced diffusion effects as they depend on molecular mixing of fuel and oxidizer prior to reaction. Additionally, these models are constrained by the rate of fuel-oxidizer mixing, leading to reduced velocities compared to the EDC model, which is primarily governed by turbulent dissipation. A similar study for mean internal pressure and outlet velocity has been conducted for the inlet temperature at 950 K and is available in Appendix D. Similar conclusions can be drawn for the temporal evolution of mean outlet velocity and mean internal pressure for each model at T_{inlet} = 950 K.

4.1.2 Auto-ignition

Figure 4.2 shows the evolution of maximum external temperature for both inlet venting temperatures according to the three numerical models. The EDC Standard model clearly illustrates an auto-ignition case for the gas mixture, with the difference between the two outgassing temperature curves in Figure 4.2. Auto-ignition can be seen by a rise in external temperature at $T_{inlet} = 1150$ K, whereas it is absent at $T_{inlet} = 950$ K.

The two combustion (NPC and PPC) models based on the chemical equilibrium assumption, show a similar evolution, leading to a rise in temperature in the external domain for both inlet temperatures chosen. The maximum temperatures reached by the Non Premixed and Partially Premixed combustion models are higher than those obtained in the EDC model in Figure 4.2. For $T_{inlet} = 950$ K, the EDC model shows no ignition, with the mean value of the maximum temperature remaining in the steady state regime while it tends towards 2150 K for the NPC and PPC combustion models. For $T_{inlet} = 1150$ K, the differences in temperature evolution between the models result from the modelling of the coupling between turbulence and combustion. The EDC model shows a more gradual rise in temperature, due to an initial phase of mixing and accumulation of reactants in the external domain. This explains why combustion does not start instantaneously, unlike the NPC and PPC models. The maximum temperature curves in the steady state regime tend towards 2000 K, 2200 K and 2100 K, respectively for the EDC, Non Premixed Combustion and Partially Premixed Combustion models. The NPC model reaches a higher temperature because it concentrates combustion in a localized region, while the lower temperature of the PPC model results from increased diffusion effects and partial premixing of reactants before ignition. The EDC model maintains temperatures around 2000 K due to its distinct approach to balancing turbulence effects with chemical reactions and heat generation.

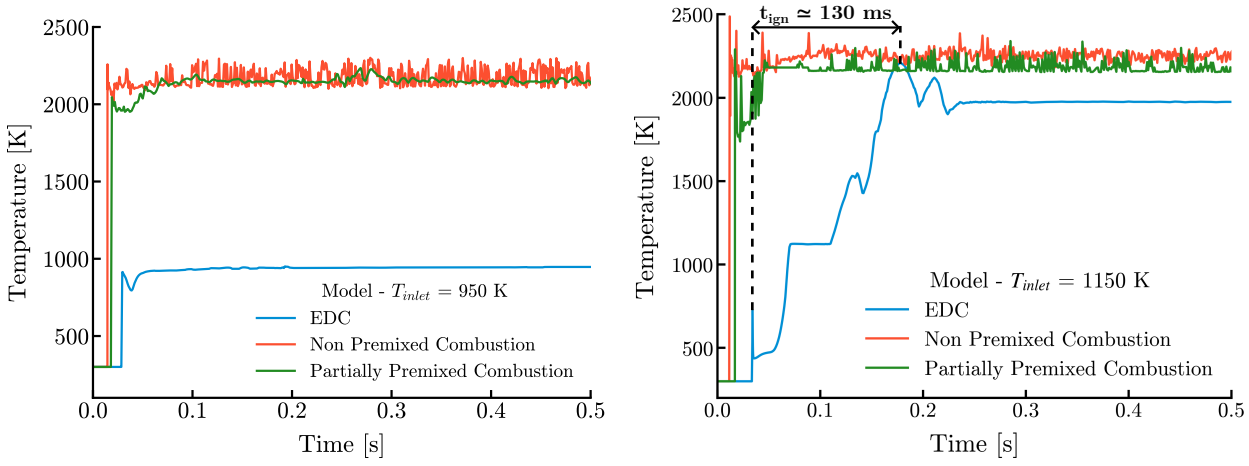

(a) Inlet temperature at 950 K

(b) Inlet temperature at 1150 K

Figure 4.2 Comparison of the temporal evolution of the maximum temperature in the external domain for two inlet temperatures according to the three numerical models

Auto-ignition delay

According to Figure 4.2, an auto-ignition delay of the gas mixture is roughly estimated around 130 ms since the venting phase for the EDC model for $T_{inlet} = 1150$ K, whereas for the NPC and PPC models, the rise in temperature is almost instantaneous when the vent is opened. For NPC and PPC models, it is not possible to correctly detect an auto-ignition delay due to model assumptions that do not take reaction kinetics into account. These models assume that the species in the gas mixture react infinitely fast on contact with air.

Figure 4.3 shows the evolution of the auto-ignition delay of the fuel mixture without inert species calculated with Cantera as a function of mixture fraction for both inlet temperatures. The auto-ignition delay in Cantera is calculated by identifying the maximum temperature gradient for each mixture fraction value to determine the time after which the mixture reaches its maximum temperature. As the inlet temperature increases, the auto-ignition delay of the gas mixture decreases and reaches its minimum for a mixture fraction value close to 1. The higher the temperature of the mixture, the faster the energetic barrier for exothermic combustion reactions is reached, and reducing the time it takes for the mixture to ignite. According to Figure 4.3, the auto-ignition delay for $T_{inlet} = 950$ K is of the order of 200 ms while it is approximately equal to 3 ms for $T_{inlet} = 1150$ K. For the NPC and PPC models, no shift was observed in the temperature rise curve for the two inlet temperatures. A shift in the maximum temperature curve is to be expected in the case of auto-ignition, particularly for $T_{inlet} = 950$ K where the auto-ignition time is different for the two inlet temperatures. It illustrates that these two combustion models cannot correctly describe auto-ignition situations.

For the EDC model at $T_{inlet} = 1150$ K, a significant difference exists between the estimate based on the temperature rise around 130 ms and that provided by Cantera ($\simeq 3.5$ ms) as shown in Figure 4.4. Although Cantera's calculations on auto-ignition delay differ from Fluent's results, this discrepancy occurs because Cantera does not consider the effects of turbulence and the dilution of fuel by inert species.

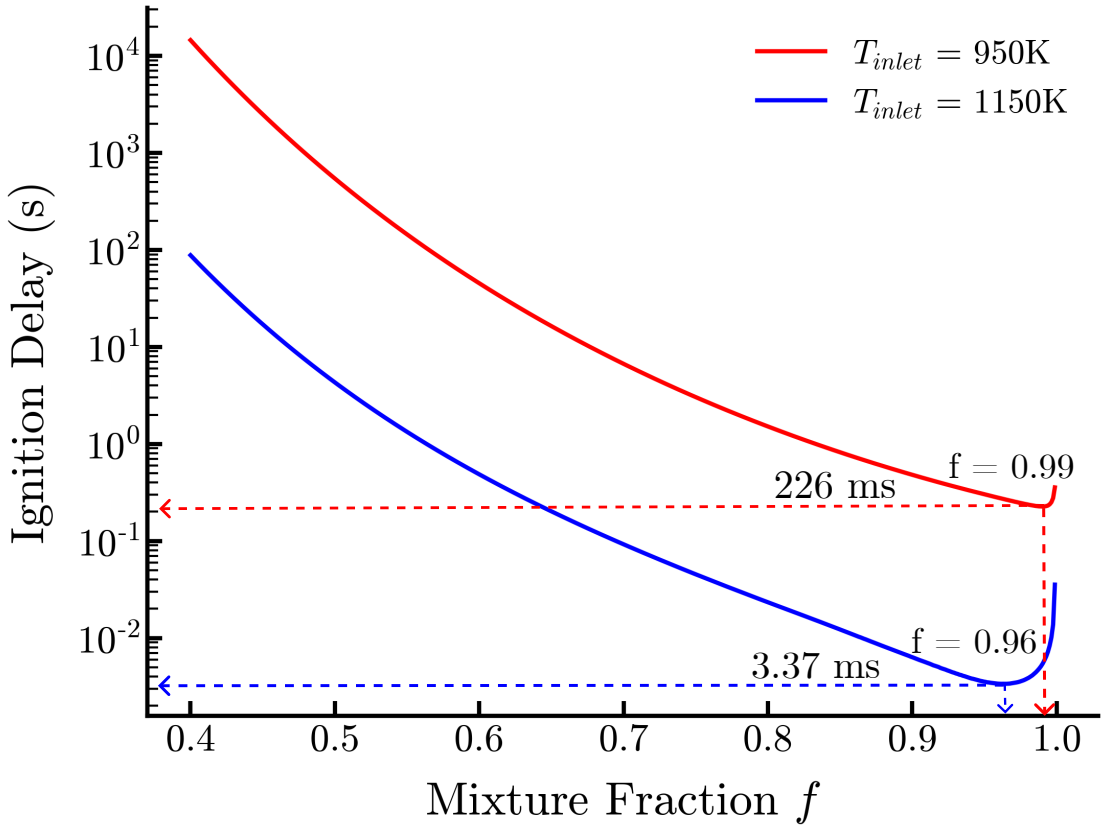

Figure 4.3 Estimation of auto-ignition delay time on Cantera as a function of mixture fraction

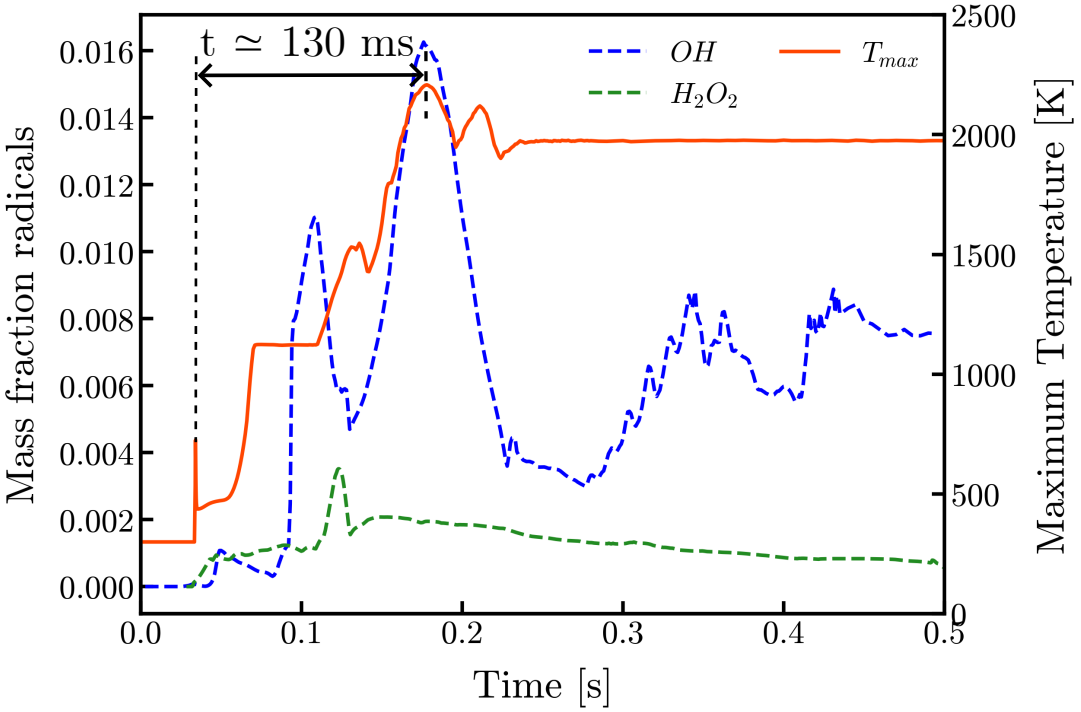

Figure 4.4 Temporal evolution of the maximum temperature and mass fractions of radicals OH and H_2O_2

Flame structure

The flame structure during steady state regime will be compared for each selected model. Temperature values were averaged in this regime, when the flame is stabilized in the domain, over 500 time-data ranging from $t = 0.5$ et $t = 1$ s.

The flame height can be estimated by taking different temperature iso-contours in the external domain. In Figure 4.5, two temperature iso-contours at 1800 K and 2000 K are chosen to distinguish the temperature regions. These temperature regions are plotted at the same simulation time ($t = 1$ s) for each model. A similar flame height of approximately 60 cm from the vent outlet is estimated for each model as shown in Figure 4.5.

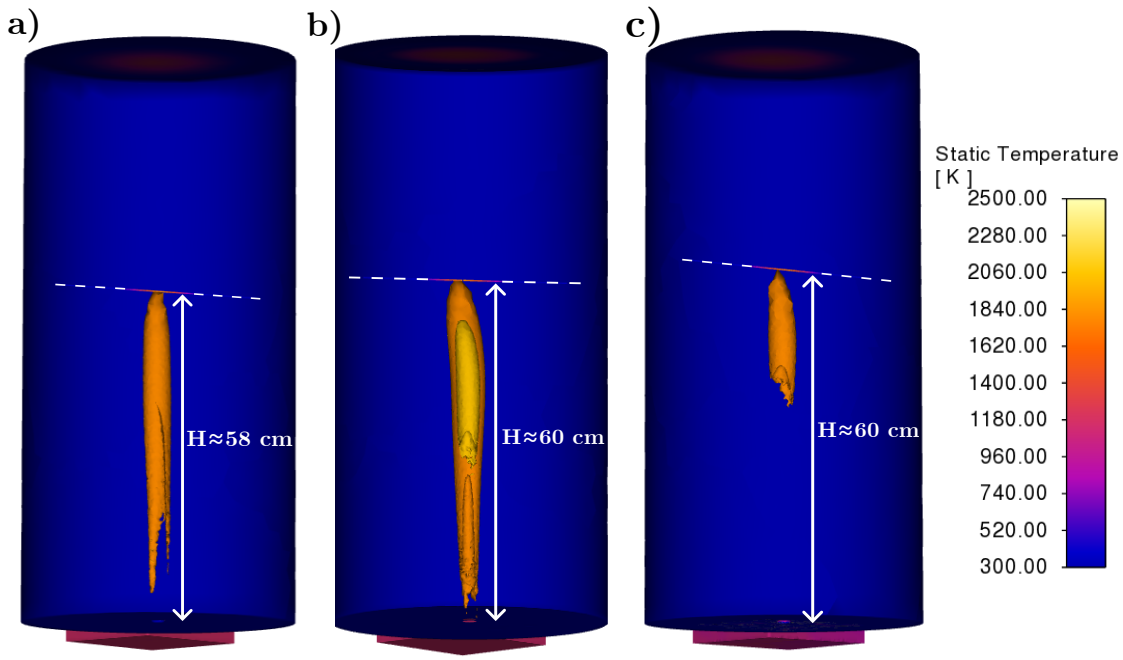

Figure 4.5 Estimation of flame height from temperature isocontours at 1800 K and 2000 K for the three models obtained on Fluent : EDC (**a**), NPC (**b**) and PPC (**c**)

To complete this analysis, another method to identify the high-temperature region is to calculate the average circumferential temperature at different cross-sections of the external domain, for the EDC model as shown in Figure 4.6. It enables measuring the average temperature across different circular cross-sections by using the central position of the vent as the circle's centre, thereby tracking temperature variations with respect to the radius at each domain section.

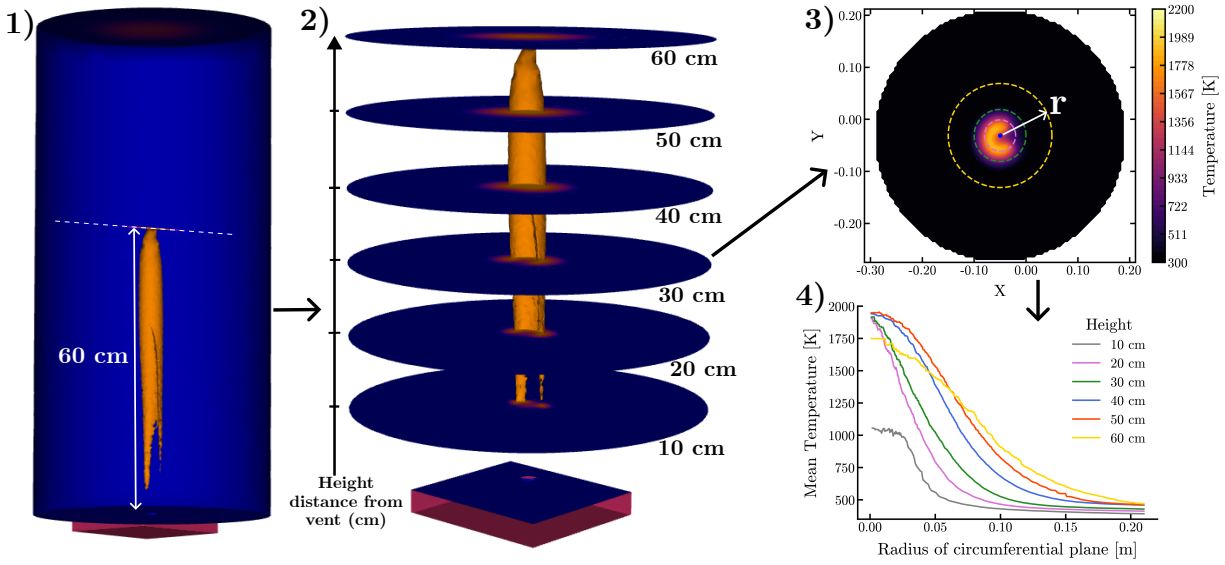

Figure 4.6 Circumferential mean external temperature for different cross-sectional planes for the EDC model in four steps: cross-sectional planes on the isocontours plotted made in the external domain (**1** & **2**), average circumferential temperature calculated for various circle radii values (**3**) and obtaining data for each plane (**4**)

For the three models, the mean circumferential temperature were obtained according to the different cross-sectional planes of the domain as shown in Figure 4.7. Average maximum temperatures are reached for a small radius near the central vent position at $r = 0$ m for the three models. In each case, the mean radial temperature decreases exponentially with distance from the central position of the vent. The central zone ($r \leq 0.02$ m) shows marked differences between the models at 30 cm and 40 cm, but these differences diminish with height. Differences between models are more pronounced at 30 cm but gradually decrease with height, suggesting thermal homogenization due to turbulence and heat diffusion at 50 cm. Only the temperature profiles for the 40 and 50 cm planes respectively reach the highest temperature values close to the center compared to the values for the other section planes. It indicates that the maximum circumferential temperature is reached on average at a height between 40 and 50 cm from the vent outlet.

This can be verified by examining the average temperature along the vent's central axis, as shown in Figure 4.8. Other graphs with the standard deviations for each model are available in Appendix E. The EDC and PPC models reach a similar peak mean temperature along the centerline at 1863 K and 1904 K respectively, while the NPC model reaches the highest temperature at 2180 K. The peak reaches respectively 43 cm from the vent in the NPC model, 45 cm in the EDC model, and 51 cm in the PPC model. The positions of the maximum axial temperatures are located within the same range of $z \in [0.4, 0.55]$ m.

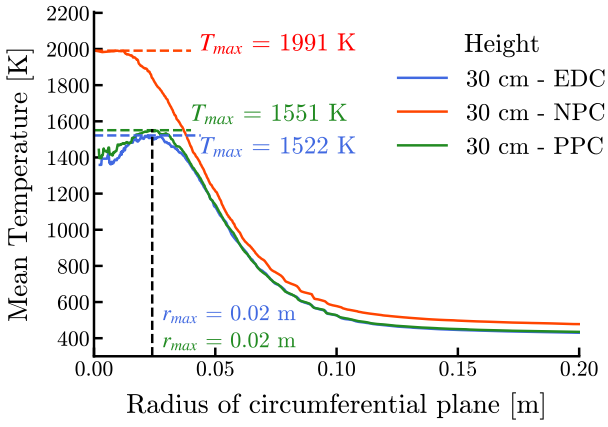

(a) Height plane at 30 cm

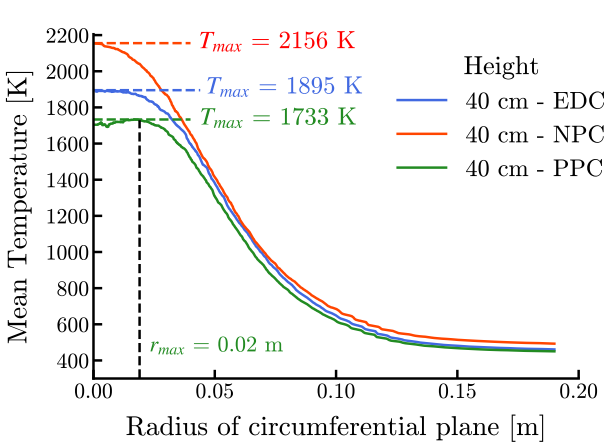

(b) Height plane at 40 cm

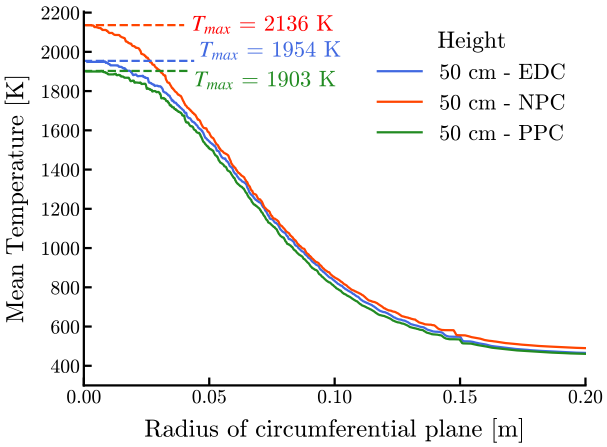

(c) Height plane at 50 cm

Figure 4.7 Comparison of the evolution of mean circumferential temperature as a function of circle radii according to the EDC, NPC and PPC models for three cross-sectional planes (30 cm (**a**), 40 cm (**b**) and 50 cm (**c**))

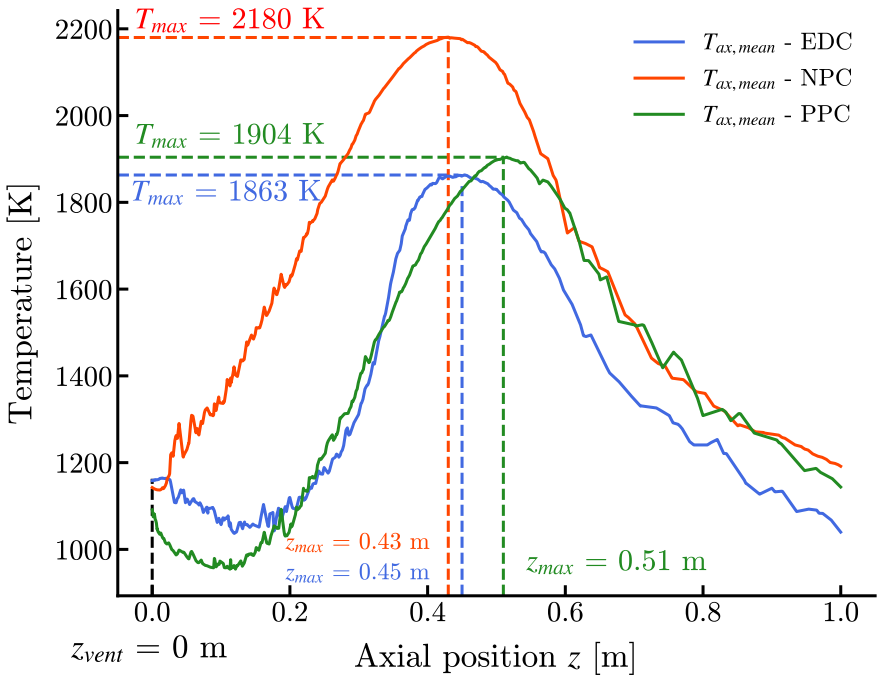

Figure 4.8 Evolution of axial temperature along the vent axis for the three different models (EDC, NPC and PPC)

4.1.3 Heat release rate

When the gas mixture auto-ignites on contact with the air, a large amount of heat is released into the external domain. Each numerical model can be used to calculate the heat release rate either by the heat produced from the chemical reactions (EDC model) or by the PDF table of thermochemical values pre-processed by Fluent (Non Premixed and Partially Premixed Combustion models). According to the nomenclature from Ansys [63], the heat release rate is defined as:

$$\mathrm{HRR} = -\sum_i \overline{R_i} \frac{h_i^0}{M_i} \tag{4.1}$$

with $\overline{R_i}$ the mean reaction source term from the species transport equation (3.14), h_i^0 and M_i are the specific enthalpy and the molar mass of species i respectively.

For each inlet temperature, the evolution of the HRR decreases towards a negative value before the venting phase, followed by a rapid increase, reaching a steady state value at 175 kW and 150 kW respectively for the NPC and PPC models. The increase in HRR is consistent with the rise in external temperature observed for both combustion models in Figure 4.2. For the EDC model, no changes in HRR are observed for $T_{inlet} = 950$ K with the absence of ignition, while for $T_{inlet} = 1150$ K, a rise is observed which tends towards a steady state value at 150 kW. The Low-Heating Value[1] (LHV) of the gas mixture is estimated at approximately 143 kW for an inlet temperature of 1150 K, which is similar in order of magnitude to the value obtained in Fluent. This evolution of HRR is also consistent with the maximum temperature rise observed for $T_{inlet} = 1150$ K with the EDC model. The difference between the curves for the three models at the two inlet temperatures of 175 kW at 950 K and 25 kW at 1150 K respectively.

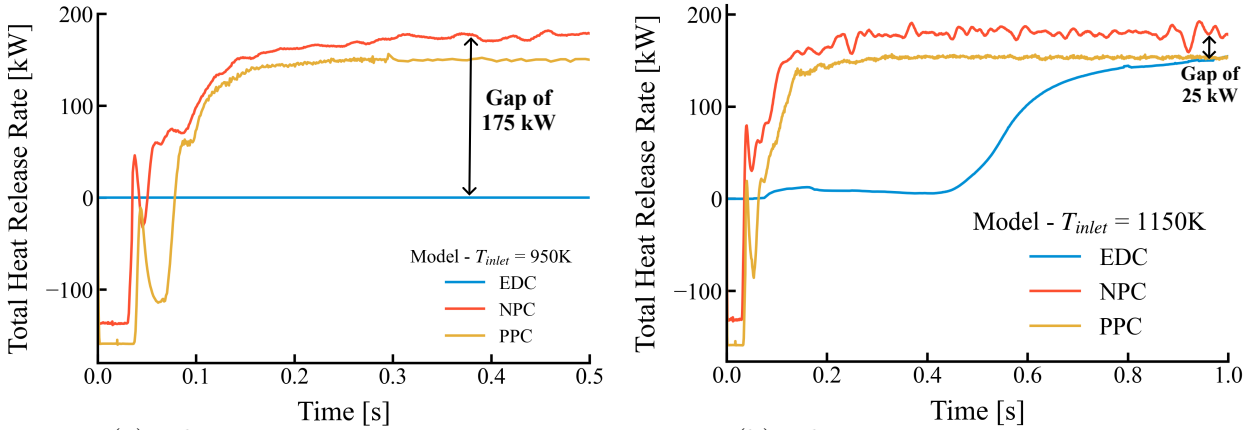

(a) Inlet temperature at 950 K (b) Inlet temperature at 1150 K

Figure 4.9 Temporal evolution of the heat release rate in the external domain for two inlet temperatures according to the three models (EDC, NPC and PPC)

[1]Theoretical value of the power released by the fuel completely consumed without taking into account the condensation of water

All previous HRR graphs were obtained using Fluent version 2024R2, but negative HRR values were detected for the EDC model using the version 2023R2. The analysis of negative values achieves mesh and time step independence using the EDC model on a fine mesh with 1.35×10^6 elements. Furthermore, research is conducted with both NPC and PPC models, employing the same mesh and test conditions as those used with the EDC model. In addition, two versions of ANSYS Fluent (2023R2 and the latest release 2024R2) were compared to see the influence of optimisations between software versions on HRR values. Details of the comparison between the two versions are available in Appendix F. The results of these analyses reveal several points about HRR values. Using the Fluent 2023R2 version, the negative HRR values are observed regardless of the combustion model. These values are sensitive to the time step size for the EDC model while they are independent of the time step size used for NPC and PPC models. Mesh refinement does not impact the negative values regardless of the combustion model used. The various solvers for chemical reactions tested with EDC model do not fully solve the presence of negative HRR values.

The latest 2024R2 version eliminates the negative HRR values that were present with the EDC model in the 2023R2 version. This correction of HRR values applies across all the solvers tested with the EDC model, reflecting the latest solver optimizations implemented by ANSYS [69,70]. Furthermore, the 2024R2 version still shows negative HRR values when using NPC and PPC models, suggesting the root cause remains unidentified. Further comparisons with future versions of ANSYS Fluent will need to be performed for both NPC and PPC models to identify the origin of the negative HRR values.

4.1.4 Critical review

The various models studied in this section have their advantages and drawbacks which are summarized in Table 4.1.

The EDC model offers a number of benefits as a candidate for sensitivity analysis, in particular for auto-ignition threshold detection. It also detects the mixture auto-ignition delay compared with the NPC and PPC combustion models, where mixture ignition occurs instantaneously on contact with air. As the RANS numerical approach is still limited in terms of precision for studying flame structure compared with more direct and computationally expensive approaches such as LES and DNS, it provides rapid diagnostic tools for observing an ignition region.

Table 4.1 Benefits and limitations of each model for the simulation of turbulent combustion of vented gases

	Benefits	**Limitations**
EDC	Possible detection of mixture auto-ignition delay Taking turbulence effects into account in reactions	Large computational times HRR negative values only detected with 2023R2 version
Reduced order models (NPC & PPC)	Short computational times Taking turbulence effects into account in reactions	Auto-ignition delay detection not available HRR negative values detected with 2023R2 and 2024R2 versions

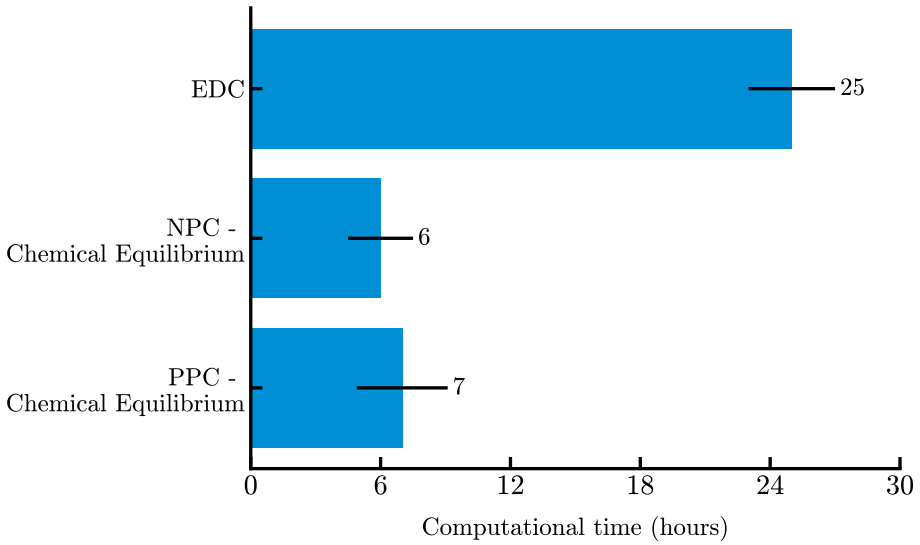

Figure 4.10 Comparison of computational time for 500 timesteps for each numerical model on 16 computing cores

The choice of a numerical model also depends on its ability to perform a complex simulation in the shortest computational time. Figure 4.10 summarizes the time required to compute each model studied for a number of 500 timesteps. The EDC model is by far the most time-consuming of the three models presented here. This is mainly due to the number of equations to be solved for the transport of chemical species which are significantly reduced for the NPC and PPC models.

As the EDC model offers a particular advantage for the study of mixture auto-ignition within turbulent flows corresponding to the main objective of the project, it is chosen for the sensitivity analysis discussed in the next section.

4.2 Sensitivity analysis with respect to module parameters

For the sensitivity analysis, the Species Transport EDC model is chosen with the Fluent 2023R2 version. Table 4.2 gives a summary of the input parameters (inlet temperature, mass flow rate, vent opening under pressure threshold, chemical composition) which will be used for the sensitivity analysis. The behaviour of the gas mixture during ignition can be analysed through the identification of key influential parameters.

Table 4.2 Test matrix to determine the parameters influencing the numerical model on the mixture's auto-ignition conditions

Influencing input parameters	Baseline Reference	**Test 1**	**Test 2**
Inlet Temperature T_{inlet}	1150 K	1150 K	1150 K
Pressure threshold	40 PSI	**50** PSI	40 PSI
Number of venting cells	1	1	**2 at the same time**
Mass flux rate ($kg.m^2.s^{-1}$)	12.7	12.7	**25.4**
Chemical composition of gas mixture	Golubkov *et al.* [35]	Golubkov *et al.* [35]	Golubkov *et al.* [35]

The baseline case is defined according to the boundary conditions defined in the Methodology part (see *Boundary conditions* in section 3.3 and Figure 3.4). Two input parameters will be studied, namely the pressure threshold for the first test and the mass flux rate which is doubled with two venting cells in the second test. The project's industrial partner has indicated that the module's vent can open at a pressure between 40 and 50 PSI. For this first test, the venting condition is modified to 50 PSI ($\approx$ 345 kPa or 3.45 bar). For the second test, the cell adjacent to the reference cell was chosen for venting as described in Figure 4.11. This choice is motivated by the fact that thermal runaway for one cell can propagate to adjacent cells in a Li-ion module from the literature review articles [20, 47]. The venting conditions are identical for the second cell, with a similar chemical composition for the mixture of gases emitted.

The various parameters studied in the sensitivity analysis will be:

- Temporal evolution of maximum temperature in the external domain
- Analysis of ignition region and flame structure if present
- Heat Release Rate (HRR)

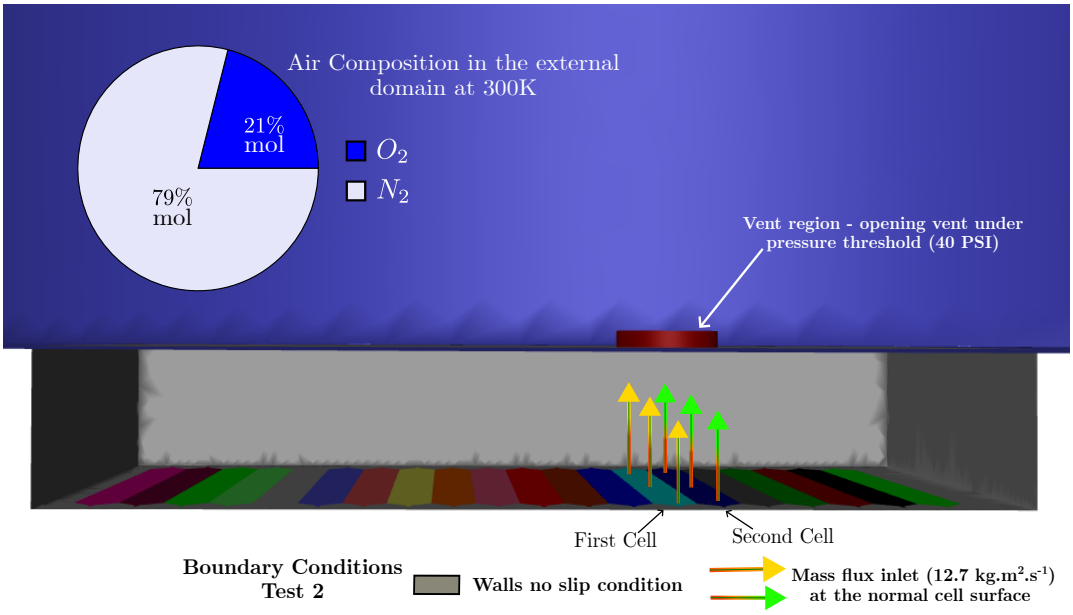

Figure 4.11 Boundary conditions for Test 2 with a second venting cell

4.2.1 Auto-ignition

Figure 4.12 shows the time evolution of maximum temperature in the external domain for each test, which is compared with the reference case. A rise in external temperature is obtained when the opening pressure is at 50 PSI. Both venting conditions lead to a similar rise in external temperature, as shown in the curves in Figure 4.12a. For Test 2 with the venting flow rate doubled, a rise in temperature was observed and the maximum temperature fails to reach a stable value over time unlike the other two tests.

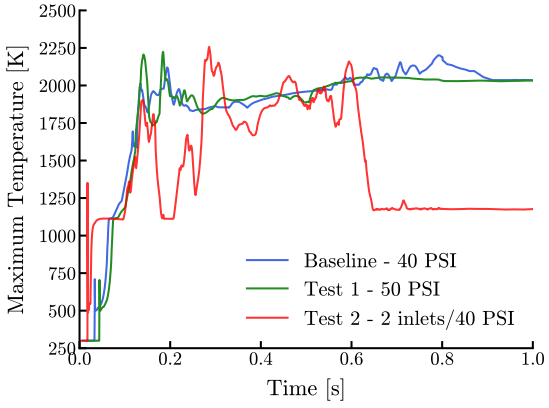

(a) Temporal evolution of the maximum temperature for each test

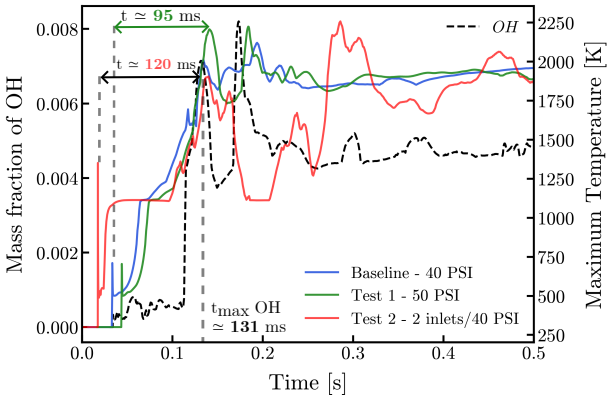

(b) Estimation of the auto-ignition delay time using the emission peak of OH radical

Figure 4.12 Temporal evolution of the maximum temperature and OH mass fraction to determine the auto-ignition delay of the mixture for each test by comparing it with the reference test

Concerning the auto-ignition delay of the mixture, the method for determining the maximum production of OH radical species gives an estimate of around 95 ms from the venting phase for Test 1 at 50 PSI. In Test 2, venting occurs earlier ($t \approx 17$ ms) than in the other two tests ($t \approx 34$ ms for the reference case and 40 ms for Test 1), which is consistent with the faster increase in internal pressure with two degassing sources. An auto-ignition delay is estimated at $\tau_{ign} \approx 120$ ms between the venting phase and the first temperature peak coinciding with the generation peak of OH radical at $t \approx 131$ ms according to Figure 4.12b. The auto-ignition delay values remain close between Test 1 and the reference test, which is approximately equal to 100 ms according to the previous section. For Test 2, the estimated auto-ignition time is longer than for the other two tests and requires further analysis to interpret this delay. It may be due to a large species dissipation rate in the external domain associated with the higher vent outlet velocity.

The ignition region is studied by the shape of the flame stabilised in the external domain, supplemented by a study of the axial temperature along the axis of the vent as described in the section.

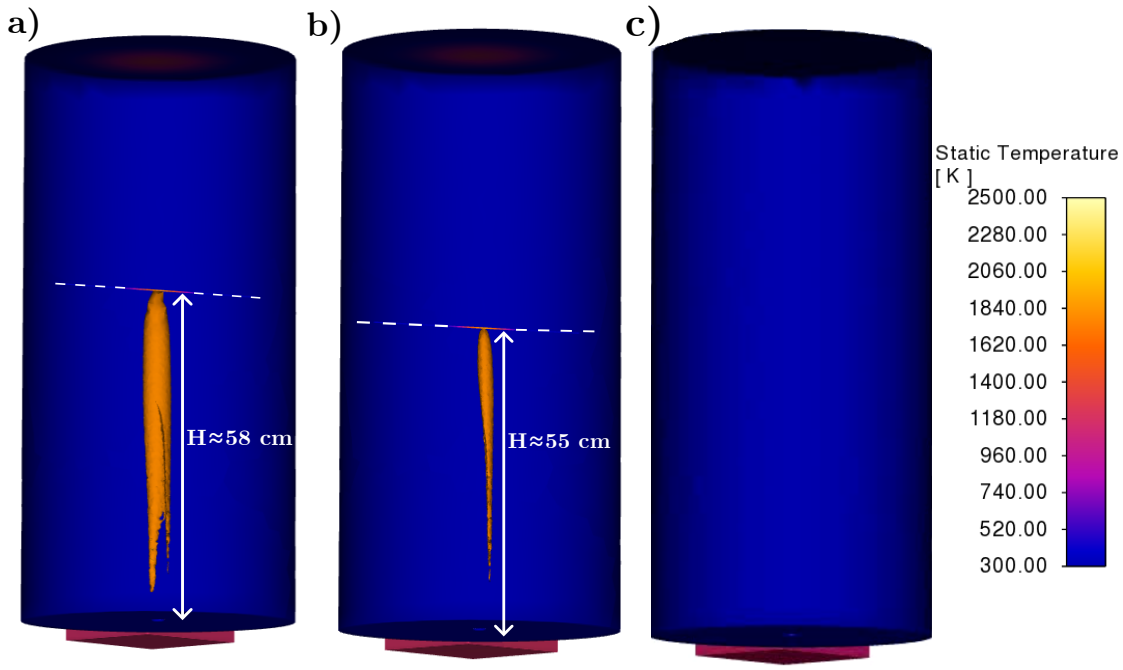

Figure 4.13 Estimation of flame height from temperature isocontours at 1800 K and 2000 K for the three models obtained on Fluent : Baseline reference (**a**), Test 1 (**b**) and Test 2 (**c**)

The isotherms at 1800 K and 2000 K are used to determine the ignition region and to indicate the presence or absence of a high temperature zone in the external domain. The flame height for Test 1 is similar with a value of around 55 cm compared to the reference case as shown in Figure 4.13. Unlike the reference case and Test 1, no flame stabilised in the external domain for Test 2 in the steady state regime as shown in Figures 4.12a and 4.13.

The position of the ignition region is verified by using the mean axial temperature with the corresponding standard deviation over a series of 500 time data points for each test. Figure 4.14 illustrates the evolution of the mean axial temperature along the axis of the vent.

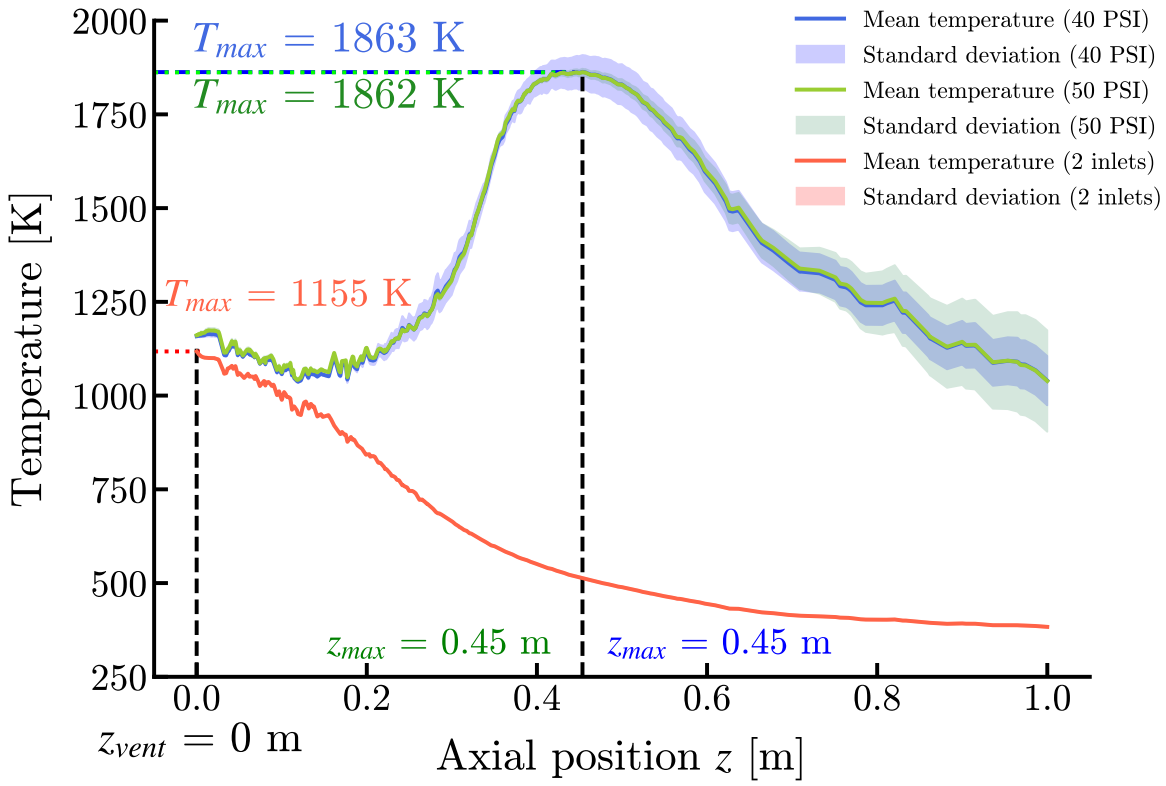

Figure 4.14 Evolution of the mean axial temperature with the related standard deviation along the vent axis for the different tests studied for the EDC model

The maximum mean axial temperature for Test 1 ($T_{max} \approx 1862$ K) is similar to that obtained for the reference test. Furthermore, this value is obtained for an identical position at the distance $z_{max} \approx 0.45$ m for both tests. As previously noted with the absence of the ignition region for Test 2, there is no axial mean temperature peak in the external domain as indicated by the red curve in Figure 4.14. The maximum mean axial temperature is reached at the vent outlet position and continues to decrease with increasing distance from the vent.

4.2.2 Heat release rate

Figure 4.15 illustrates the temporal evolution of the HRR for each test.

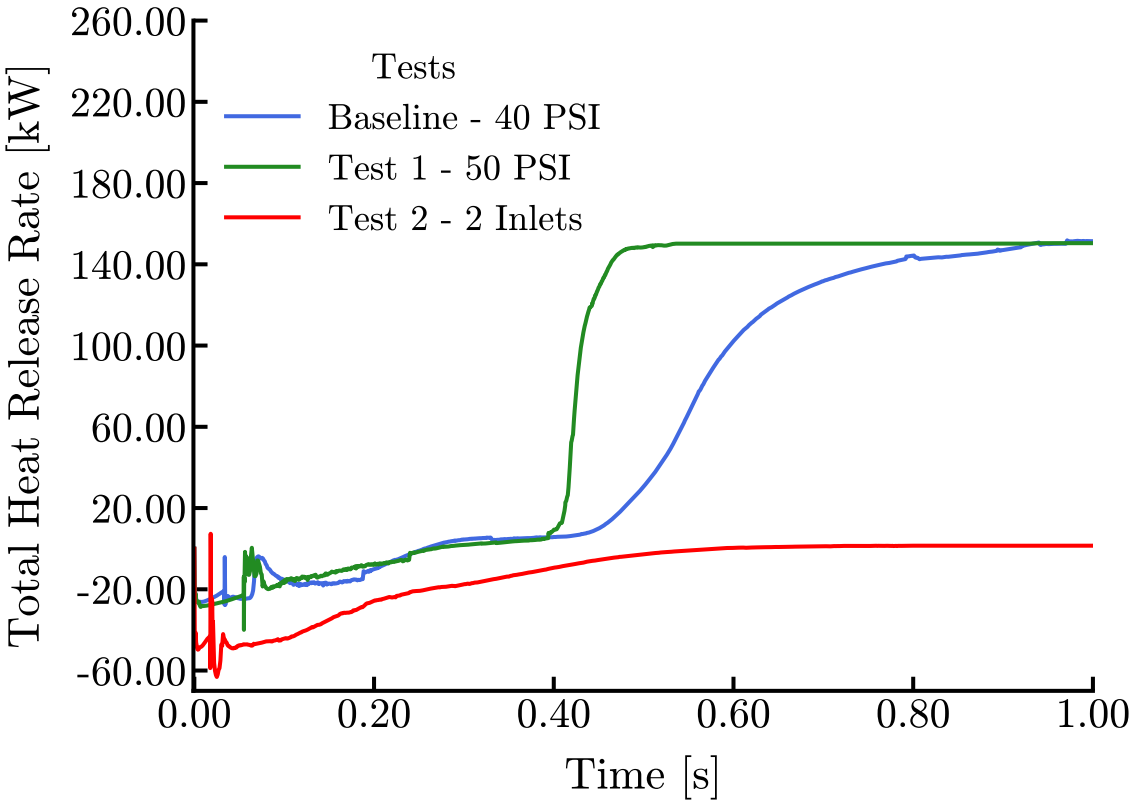

Figure 4.15 Temporal evolution of Heat Release Rate in the external domain for each test

The evolution of HRR for Test 1 tends towards a steady-state value close to the reference test around 150 kW. The increase in HRR confirms the hypothesis of the presence of an ignition region observed for these two tests in the previous section. A vent opening threshold with a higher internal pressure like 50 PSI improves mixing between the different species. This leads to a more rapid release of energy from the reactions compared with the reference case. For Test 2, the HRR trend shows a small increase compared to the other two tests.

For all three tests, the evolution of the HRR starts with a decrease towards negative values over a short period at the beginning of the simulation, as it was also observed in the previous section on the comparisons between the models. A more detailed analysis with the recent 2024R2 Fluent version is required to determine the origin of these negative HRR values.

4.2.3 Critical review

The new venting condition at 50 PSI has a minor effect on the mixture's auto-ignition conditions compared with the reference case, particularly for the auto-ignition delay values and the maximum axial temperature value in the external domain. In the case of Test 2 with two degassing sources, an increase in external temperature is observed but the ignition conditions are not maintained over time. It can be explained by the larger strain rate of the flame in the external domain linked to the higher outlet jet velocity. Beyond a given strain rate, the combustion reactions can no longer compensate for the heat losses, leading to the local extinction of the flame. This hypothesis needs to be experimentally verified in future studies.

For this sensitivity analysis study, two influencing factors were analysed, namely the vent opening pressure and the number of venting sources influencing the venting rate. Other parameters could of course be studied, such as the position of the outgassing cell, a greater number of outgassing cells, a different chemical composition of the mixture, and a variable flow rate as a function of time. However, in the absence of experimental data, a large number of combinations of these parameters could be tested in order to observe their influence on auto-ignition conditions of the gas mixture. Once the experimental conditions are known, the model will have to be verified and validated against the experimental data acquired.

CHAPTER 5 CONCLUSION

5.1 Summary of works

Throughout this thesis, the various characteristics of the numerical models available on the solver ANSYS Fluent CFD dedicated to turbulent combustion in the gas phase have been compared. Using the knowledge available in the literature, simplified boundary conditions for venting have been adapted, taking into account the geometry of the LMP® cells. A coupling between the different phenomena of venting, turbulence and combustion reactions in the gas phase was implemented for each model. Prediction tools for the ignition conditions of the gas mixture were applied when comparing the numerical models, such as the estimation of the auto-ignition delay by the radical emission peak, and the circumferential and axial mean temperature. Detecting the ignition of the mixture represents the main complexity in modelling gas-phase combustion reactions in a turbulent flow for a RANS numerical approach.

The various models have their advantages and shortcomings in terms of taking into account the interaction between chemical kinetics and turbulence, computational time and the prediction of gas mixture ignition conditions. Reduced-order combustion models (NPC & PPC) allow rapid analysis of the ignition context of the mixture, with the advantage of reducing calculation costs, but the significant disadvantage of not being able to accurately estimate an auto-ignition delay. Models with species transport, such as EDC, have the advantage of predicting ignition conditions, but their drawbacks are in the calculation time required to solve the equations for each of the species in a mechanism. A suitable trade-off has to be found between the model's calculation performance and its ability to predict the mixture's auto-ignition conditions.

For the sensitivity analysis, the EDC model was chosen for its ability to detect an ignition region and a mixture auto-ignition delay, despite its significant computational cost. The sensitivity analysis was performed on two different venting configurations, in particular to illustrate the influence of certain parameters on mixture ignition conditions. Vent opening conditions at a higher pressure like 50 PSI have little influence on auto-ignition conditions. The number of degassing sources within the module has more influence on the spontaneous combustion conditions of the mixture. Due to the higher vent outlet velocity, the strain rate of the flame is presumably larger, which could lead to local flame extinction and potentially prevent the ignition region from being maintained. This assumption requires experimental verification in future work.

5.2 Limitations

The numerical modelling proposed in this work has limitations that can be improved in several aspects: in-depth study of the combustion models, numerical optimisation, choice of boundary conditions adapted to the experimental values and addition of other physical phenomena.

The study of numerical models on Fluent focuses on the influence of the parameters in each approach on the accuracy of the results. The use of three distinct mixtures (fuel, inert species and air) limits the choice of models supported by Fluent, but the selection of other combustion models such as the Transport PDF approach may offer a useful alternative for comparison with other existing models. Finally, the origin of the presence of negative HRR values for NPC and PPC models remains unidentified and requires further investigation with the recent Fluent version 2024R2. Another limitation is the use of a commercial solver like ANSYS, whose source code for the models is not directly accessible. This prevents the precise identification of the cause of these negative values and thus limits our understanding of the behaviour of the different models.

The numerical optimisation focuses on the influence of the small time step and mesh refinement on the evolution of the external temperature or the HRR in order to describe more precisely the auto-ignition conditions of the gas mixture. In addition, dynamic methods of adaptive mesh refinement or time step size as a function of the temperature gradient in the external domain can improve the accuracy of the calculations obtained. Knowing the limitations of the accuracy of the RANS numerical approach compared with that of LES and DNS, it would be interesting to see whether LES modelling could be implemented for turbulent combustion in the gas phase to increase numerical accuracy.

The assumptions chosen for the boundary conditions are based on literature. The model is intended to be simplified by the choice of boundary conditions (constant and uniform outgassing at the normal cell surface, constant venting temperature, chemical composition from an LFP liquid electrolyte cell [35]). However, each input parameter must be adapted with appropriate experimental data. This is because, in the absence of reference data on the precise degassing conditions of the LMP® cell subjected to thermal runaway, many input parameters may need to be tested.

In this modelling, only the gas phase is considered in the fluid region, but a two-phase approach with the ejection of solid particles coupled to the release of gas can be included in the modelling of the fluid domain. Other physical phenomena specific to thermal runaway, such as heat generation, radiation, internal reactions in the solid phase and thermal conduction, are not taken into account here and will have to be set up to model a complete thermal runaway process in a cell. These physical phenomena can be modelled using existing Fluent modules or by creating user functions.

5.3 Future research and perspectives

This numerical modelling work is intended as a first step towards providing the industrial partner with numerical tools for predicting the detection of an ignition region. The benefit of this modelling is that it can be made flexible by modifying the boundary conditions (mass flow rate, temperature, chemical composition). It would be useful to continue the modelling using the latest versions of ANSYS Fluent and even to apply it with other commercial solvers like StarCMM+ in order to compare the numerical results. Once the experimental data can be acquired in-house, these boundary conditions will have to be implemented in the model in order to validate the numerical results. Once the modelling in the fluid phase has been verified and validated, coupling with the internal reactions in the solid phase within the battery can be implemented, particularly for heat and gas generation.

Few studies in the literature have investigated the coupled modelling between the fluid and solid phases of thermal runaway in solid electrolyte cells. The main challenge will be to determine a chemical mechanism that can include both the degradation reactions of the internal components of the battery in the solid phase and the combustion reactions in the gas phase.

Other physical phenomena such as radiation or thermal conduction between cells could also be added to model thermal runaway propagation through the various cells. In the long-term, the idea is to combine all the different physical phenomena, including thermal runaway in the cell, to create a predicting tool for the risk of thermal runaway propagation in a battery module.

REFERENCES

[1] D. Stampatori, P. P. Raimondi, and M. Noussan, "Li-Ion Batteries: A Review of a Key Technology for Transport Decarbonization," *Energies*, vol. 13, no. 10, p. 2638, Jan. 2020, publisher: Multidisciplinary Digital Publishing Institute. [Online]. Available: https://www.mdpi.com/1996-1073/13/10/2638

[2] X. Zhang *et al.*, "A review on thermal management of lithium-ion batteries for electric vehicles," *Energy*, vol. 238, p. 121652, Jan. 2022. [Online]. Available: https://www.sciencedirect.com/science/article/pii/S0360544221019009

[3] A. Masias, J. Marcicki, and W. A. Paxton, "Opportunities and Challenges of Lithium Ion Batteries in Automotive Applications," *ACS Energy Letters*, vol. 6, no. 2, pp. 621–630, Feb. 2021, publisher: American Chemical Society. [Online]. Available: https://doi.org/10.1021/acsenergylett.0c02584

[4] S. Xie *et al.*, "Research progress and prospects on thermal safety of lithium-ion batteries in aviation low-temperature and low-pressure environments," *Journal of Energy Storage*, vol. 83, p. 110734, Apr. 2024. [Online]. Available: https://www.sciencedirect.com/science/article/pii/S2352152X24003189

[5] A. Nagy, "Electric aircraft - present and future," *Production Engineering Archives*, vol. 23, no. 23, pp. 36–40, Jun. 2019. [Online]. Available: https://sciendo.com/article/10.30657/pea.2019.23.06

[6] F. C. Krause *et al.*, "Performance of Commercial Li-Ion Cells for Future NASA Missions and Aerospace Applications," *Journal of The Electrochemical Society*, vol. 168, no. 4, p. 040504, Apr. 2021, publisher: IOP Publishing. [Online]. Available: https://dx.doi.org/10.1149/1945-7111/abf05f

[7] I. P. on Climate Change (IPCC) *et al.*, "Chapter 10 transport in climate change 2022: Mitigation of climate change. contribution of working group iii to the sixth assessment report of the intergovernmental panel on climate change," IPCC, Cambridge and New York, Tech. Rep., 2023. [Online]. Available: https://www.ipcc.ch/report/ar6/wg3/chapter/chapter-10/

[8] T. P. Barrera *et al.*, "Next-Generation Aviation Li-Ion Battery Technologies—Enabling Electrified Aircraft," *The Electrochemical Society Interface*, vol. 31, no. 3,

pp. 69–74, Sep. 2022, publisher: IOP Publishing. [Online]. Available: https://iopscience.iop.org/article/10.1149/2.F10223IF/meta

[9] I. E. Agency, "Net Zero by 2050 – Analysis," International Energy Agency, Paris, Tech. Rep., May 2021. [Online]. Available: https://www.iea.org/reports/net-zero-by-2050

[10] A. Yoshino, K. Sanechika, and T. Nakajima, "Li-ion Secondary Battery Patent," Japan Patent US4 668 595A, May, 1987. [Online]. Available: https://patents.google.com/patent/US4668595A/en

[11] J. Robert and J. Alzieu, "Accumulateurs au lithium," *Techniques de l'ingénieur Conversion de l'énergie électrique*, vol. base documentaire : TIP301WEB., no. ref. article : d3354, p. 15, 2005, publisher: Editions T.I. Type: base documentaire _eprint: base documentaire : TIP301WEB. [Online]. Available: https://www.techniques-ingenieur.fr/base-documentaire/energies-th4/accumulateurs-d-energie-42243210/accumulateurs-d3354/

[12] A. Yoshino, "The Birth of the Lithium-Ion Battery," *Angewandte Chemie International Edition*, vol. 51, no. 24, pp. 5798–5800, Jan. 2012, _eprint: https://onlinelibrary.wiley.com/doi/pdf/10.1002/anie.201105006. [Online]. Available: https://onlinelibrary.wiley.com/doi/abs/10.1002/anie.201105006

[13] C. Schultz *et al.*, "Investigation of the decomposition of organic solvent-based lithium ion battery electrolytes with liquid chromatography-mass spectrometry," *Spectroscopy Europe/World*, vol. 28, no. 5, p. 4, 2016, publisher: IM Publications Open LLP. [Online]. Available: https://www.spectroscopyeurope.com/article/investigation-decomposition-organic-solvent-based-lithium-ion-battery-electrolytes-liquid

[14] Q. Wang *et al.*, "A review of lithium ion battery failure mechanisms and fire prevention strategies," *Progress in Energy and Combustion Science*, vol. 73, pp. 95–131, Jul. 2019. [Online]. Available: https://www.sciencedirect.com/science/article/pii/S0360128518301801

[15] J. B. Goodenough and K.-S. Park, "The li-ion rechargeable battery: A perspective," *Journal of the American Chemical Society*, vol. 135, no. 4, pp. 1167–1176, 2013, pMID: 23294028. [Online]. Available: https://doi.org/10.1021/ja3091438

[16] IEA, "Batteries and secure energy transitions – analysis," IEA, Tech. Rep., 2024. [Online]. Available: https://www.iea.org/reports/batteries-and-secure-energy-transitions

[17] Q. Wang *et al.*, "Thermal runaway caused fire and explosion of lithium ion battery," *Journal of Power Sources*, vol. 208, pp. 210–224, Jun. 2012. [Online]. Available: https://www.sciencedirect.com/science/article/pii/S0378775312003989

[18] R. Srinivasan *et al.*, "Preventing Cell-to-Cell Propagation of Thermal Runaway in Lithium-Ion Batteries," *Journal of The Electrochemical Society*, vol. 167, no. 2, p. 020559, Feb. 2020, publisher: IOP Publishing. [Online]. Available: https://dx.doi.org/10.1149/1945-7111/ab6ff0

[19] J. Lamb *et al.*, "Failure propagation in multi-cell lithium ion batteries," *Journal of Power Sources*, vol. 283, pp. 517–523, Jun. 2015. [Online]. Available: https://www.sciencedirect.com/science/article/pii/S0378775314016905

[20] J. Kim *et al.*, "Modeling cell venting and gas-phase reactions in 18650 lithium ion batteries during thermal runaway," *Journal of Power Sources*, vol. 489, p. 229496, Mar. 2021. [Online]. Available: https://www.sciencedirect.com/science/article/pii/S0378775321000458

[21] OACI, "Dangerous Good Panel 29th Meeting," OACI, Montreal, Tech. Rep. DGP/29-IP/9, Sep. 2023. [Online]. Available: https://www.iata.org/en/programs/cargo/dgr/download/

[22] IATA, "Dangerous Goods Documentation IATA Addendum 2024," IATA, Tech. Rep. 65th Edition, Apr. 2024. [Online]. Available: https://www.iata.org/en/programs/cargo/dgr/download/

[23] R. Zhao *et al.*, "Development of a coupled model of heat generation and jet flow of lithium-ion batteries during thermal runaway," *Journal of Energy Storage*, vol. 63, p. 107048, Jul. 2023. [Online]. Available: https://www.sciencedirect.com/science/article/pii/S2352152X23004450

[24] W. Li *et al.*, "High Resolution 3-D Simulations of Venting in 18650 Lithium-Ion Cells," *Frontiers in Energy Research*, vol. 9, Dec. 2021, publisher: Frontiers. [Online]. Available: https://www.frontiersin.org/journals/energy-research/articles/10.3389/fenrg.2021.788239/full

[25] D. Veynante and L. Vervisch, "Turbulent combustion modeling," *Progress in Energy and Combustion Science*, vol. 28, no. 3, pp. 193–266, 2002. [Online]. Available: https://www.sciencedirect.com/science/article/pii/S036012850100017X

[26] T. Poinsot and D. Veynante, *Theoretical and Numerical Combustion*. R.T. Edwards, Inc., May 2022, google-Books-ID: cqFDkeVABYoC.

[27] J. Janek and W. G. Zeier, "A solid future for battery development," *Nature Energy*, vol. 1, no. 9, pp. 1–4, Sep. 2016, publisher: Nature Publishing Group. [Online]. Available: https://www.nature.com/articles/nenergy2016141

[28] L. Kong *et al.*, "Configuring solid-state batteries to power electric vehicles: a deliberation on technology, chemistry and energy," *Chemical Communications*, vol. 57, no. 94, pp. 12 587–12 594, Nov. 2021, publisher: The Royal Society of Chemistry. [Online]. Available: https://pubs.rsc.org/en/content/articlelanding/2021/cc/d1cc04368d

[29] M.-C. Pang *et al.*, "Interactions are important: Linking multi-physics mechanisms to the performance and degradation of solid-state batteries," *Materials Today*, vol. 49, pp. 145–183, Oct. 2021. [Online]. Available: https://www.sciencedirect.com/science/article/pii/S1369702121000572

[30] T. Dussart, "Batterie lithium tout solide : augmentation de la densité de courant critique et procédé innovant de fabrication," phdthesis, Sorbonne Université, Oct. 2021. [Online]. Available: https://theses.hal.science/tel-03681942

[31] I. Lucas and A. Gajan, "La réactivité du lithium à l'origine de performances électriques extraordinaires," Feb. 2021. [Online]. Available: https://culturesciences.chimie.ens.fr/thematiques/chimie-physique/electrochimie/la-reactivite-du-lithium-a-l-origine-de-performances

[32] B. Solutions, "Blue Solutions - Battery technology," 2024. [Online]. Available: https://www.blue-solutions.com/en/battery-technology

[33] Q. Wang, J. Sun, and G. Chu, "Lithium Ion Battery Fire And Explosion," *Fire Safety Science*, vol. 8, pp. 375–382, 2005. [Online]. Available: http://www.iafss.org/publications/fss/8/375

[34] Golubkov, Andrey W. and Fuchs, David and Wagner, Julian and Wiltsche, Helmar and Stangl, Christoph and Fauler, Gisela and Voitic, Gernot and Thaler, Alexander and Hacker, Viktor, "Thermal-runaway experiments on consumer Li-ion batteries with metal-oxide and olivin-type cathodes," *RSC Advances*, vol. 4, no. 7, pp. 3633–3642, Dec. 2013, publisher: The Royal Society of Chemistry. [Online]. Available: https://pubs.rsc.org/en/content/articlelanding/2014/ra/c3ra45748f

[35] A. W. Golubkov *et al.*, "Thermal runaway of commercial 18650 Li-ion batteries with LFP and NCA cathodes – impact of state of charge and overcharge," *RSC Advances*, vol. 5, no. 70, pp. 57 171–57 186, Jun. 2015, publisher: The Royal Society of Chemistry. [Online]. Available: https://pubs.rsc.org/en/content/articlelanding/2015/ra/c5ra05897j

[36] H. Joachin *et al.*, "Electrochemical and Thermal Studies of Carbon-Coated LiFePO4 Cathode," *Journal of The Electrochemical Society*, vol. 156, no. 6, p. A401, Apr. 2009, publisher: IOP Publishing. [Online]. Available: https://iopscience.iop.org/article/10.1149/1.3106121/meta

[37] T. Rappsilber *et al.*, "Meta-analysis of heat release and smoke gas emission during thermal runaway of lithium-ion batteries," *Journal of Energy Storage*, vol. 60, p. 106579, Apr. 2023. [Online]. Available: https://www.sciencedirect.com/science/article/pii/S2352152X22025683

[38] S. J. Harris, A. Timmons, and W. J. Pitz, "A combustion chemistry analysis of carbonate solvents used in Li-ion batteries," *Journal of Power Sources*, vol. 193, no. 2, pp. 855–858, Sep. 2009. [Online]. Available: https://www.sciencedirect.com/science/article/pii/S0378775309007162

[39] V. Goupil *et al.*, "Effect of the heating rate on the degassing and combustion of cylindrical li-ion cells," *Fire Safety Journal*, vol. 133, p. 103648, 2022. [Online]. Available: https://www.sciencedirect.com/science/article/pii/S0379711222001254

[40] E. P. Roth, "Thermal Response and Flammability of Li-Ion Cells for HEV and PHEV Applications," *SAE Mobilus*, Apr. 2008, publisher: SAE International. [Online]. Available: https://saemobilus.sae.org/articles/thermal-response-flammability-li-ion-cells-hev-phev-applications-2008-01-0400

[41] P. Huang *et al.*, "Experimental and modeling analysis of thermal runaway propagation over the large format energy storage battery module with Li4Ti5O12 anode," *Applied Energy*, vol. 183, pp. 659–673, Dec. 2016. [Online]. Available: https://www.sciencedirect.com/science/article/pii/S0306261916312697

[42] P. Ping *et al.*, "Study of the fire behavior of high-energy lithium-ion batteries with full-scale burning test," *Journal of Power Sources*, vol. 285, pp. 80–89, Jul. 2015. [Online]. Available: https://www.sciencedirect.com/science/article/pii/S0378775315004516

[43] Huang, Peifeng and Wang, Qingsong and Li, Ke and Ping, Ping and Sun, Jinhua, "The combustion behavior of large scale lithium titanate battery," *Scientific Reports*, vol. 5,

no. 1, p. 7788, Jan. 2015, publisher: Nature Publishing Group. [Online]. Available: https://www.nature.com/articles/srep07788

[44] CERFACS, "AVBP Website," 2002. [Online]. Available: https://www.cerfacs.fr/avbp7x

[45] A. Cellier *et al.*, "An analytically reduced chemistry scheme for large eddy simulation of lithium-ion battery fires," *Combustion and Flame*, vol. 250, p. 112648, Apr. 2023. [Online]. Available: https://www.sciencedirect.com/science/article/pii/S0010218023000330

[46] J. K. Ostanek *et al.*, "Simulating onset and evolution of thermal runaway in Li-ion cells using a coupled thermal and venting model," *Applied Energy*, vol. 268, p. 114972, Jun. 2020. [Online]. Available: https://www.sciencedirect.com/science/article/pii/S0306261920304840

[47] D. Mishra, P. Zhao, and A. Jain, "Thermal Runaway Propagation in Li-ion Battery Packs Due to Combustion of Vent Gases," *Journal of The Electrochemical Society*, vol. 169, no. 10, p. 100520, Oct. 2022, publisher: IOP Publishing. [Online]. Available: https://dx.doi.org/10.1149/1945-7111/ac91a7

[48] S. Abada, "Compréhension et modélisation de l'emballement thermique de batteries Li-ion neuves et vieillies." PhD Thesis, Université Pierre et Marie Curie (Paris VI), Dec. 2016. [Online]. Available: https://theses.hal.science/tel-01610218

[49] C. Chanson, "Li-Ion Batteries Safety," Agoria, Jun. 2013.

[50] N. Guillet, "Les risques liés aux batteries Li-ion," in *Journée technique : Risques Électriques - Quelle prévention en entreprise ?*, Paris, France, Jan. 2019. [Online]. Available: https://hal.science/hal-03215270

[51] B. Lei *et al.*, "Experimental Analysis of Thermal Runaway in 18650 Cylindrical Li-Ion Cells Using an Accelerating Rate Calorimeter," *Batteries*, vol. 3, no. 2, p. 14, Jun. 2017, number: 2 Publisher: Multidisciplinary Digital Publishing Institute. [Online]. Available: https://www.mdpi.com/2313-0105/3/2/14

[52] C. D. Argyropoulos and N. C. Markatos, "Recent advances on the numerical modelling of turbulent flows," *Applied Mathematical Modelling*, vol. 39, no. 2, pp. 693–732, Jan. 2015. [Online]. Available: https://www.sciencedirect.com/science/article/pii/S0307904X14003448

[53] D. Kong *et al.*, "A coupled conjugate heat transfer and CFD model for the thermal runaway evolution and jet fire of 18650 lithium-ion battery under thermal abuse," *eTransportation*, vol. 12, p. 100157, May 2022. [Online]. Available: https://www.sciencedirect.com/science/article/pii/S2590116822000030

[54] OpenCFD, "OpenFOAM Website," 2024. [Online]. Available: https://www.openfoam.com/documentation/overview

[55] Combustion Research Group San Diego, "Chemical-Kinetic Mechanisms for Combustion Applications: Combustion Research Group at UC San Diego," Dec. 2016. [Online]. Available: https://web.eng.ucsd.edu/mae/groups/combustion/mechanism.html

[56] J. O. Hinze, *Turbulence*. McGraw-Hill, 1975.

[57] S. B. Pope, *Turbulent Flows*. Cambridge University Press, Aug. 2000. [Online]. Available: https://www.cambridge.org/highereducation/books/turbulent-flows/C58EFF59AF9B81AE6CFAC9ED16486B3A

[58] Z. Yang and T. H. Shih, "New time scale based $k-\varepsilon$ model for near-wall turbulence," *AIAA Journal*, vol. 31, no. 7, pp. 1191–1198, Jul. 1993, publisher: American Institute of Aeronautics and Astronautics. [Online]. Available: https://arc.aiaa.org/doi/10.2514/3.11752

[59] T.-H. Shih *et al.*, "A new $k-\varepsilon$ eddy viscosity model for high reynolds number turbulent flows," *Computers & Fluids*, vol. 24, no. 3, pp. 227–238, Mar. 1995. [Online]. Available: https://www.sciencedirect.com/science/article/pii/004579309400032T

[60] S. Sarkar and B. Lakshmanan, "Application of a Reynolds stress turbulence model to the compressible shear layer," *AIAA Journal*, vol. 29, no. 5, pp. 743–749, 1991, publisher: American Institute of Aeronautics and Astronautics. [Online]. Available: https://arc.aiaa.org/doi/10.2514/3.10649

[61] B. E. B. E. Launder and D. B. D. B. Spalding, *Lectures in mathematical models of turbulence*. London: Academic Press, 1972.

[62] B. F. Magnussen and B. H. Hjertager, "On mathematical modeling of turbulent combustion with special emphasis on soot formation and combustion," *Symposium (International) on Combustion*, vol. 16, no. 1, pp. 719–729, Jan. 1977. [Online]. Available: https://www.sciencedirect.com/science/article/pii/S0082078477803664

[63] Ansys Inc, "Ansys Theory and User's Guide Release 24.1," 2024.

[64] M. T. Lewandowski and I. S. Ertesvåg, "Analysis of the Eddy Dissipation Concept formulation for MILD combustion modelling," *Fuel*, vol. 224, pp. 687–700, Jul. 2018. [Online]. Available: https://www.sciencedirect.com/science/article/pii/S0016236118305180

[65] M. Ferrarotti, Z. Li, and A. Parente, "On the role of mixing models in the simulation of MILD combustion using finite-rate chemistry combustion models," *Proceedings of the Combustion Institute*, vol. 37, no. 4, pp. 4531–4538, 2019. [Online]. Available: https://www.sciencedirect.com/science/article/pii/S1540748918304619

[66] W. P. Jones and J. H. Whitelaw, "Calculation methods for reacting turbulent flows: A review," *Combustion and Flame*, vol. 48, pp. 1–26, Jan. 1982. [Online]. Available: https://www.sciencedirect.com/science/article/pii/0010218082901122

[67] K. Bray, P. Domingo, and L. Vervisch, "Role of the progress variable in models for partially premixed turbulent combustion," *Combustion and Flame*, vol. 141, no. 4, pp. 431–437, 2005. [Online]. Available: https://www.sciencedirect.com/science/article/pii/S0010218005000520

[68] Z. Liao *et al.*, "Hazard analysis of thermally abused lithium-ion batteries at different state of charges," *Journal of Energy Storage*, vol. 27, p. 101065, Feb. 2020. [Online]. Available: https://www.sciencedirect.com/science/article/pii/S2352152X19305213

[69] Ansys Inc, "ANSYS 2024 R2 delivers innovation across industries and domains." [Online]. Available: https://www.ansys.com/news-center/press-releases/7-23-24-r2-innovates-across-industries-and-domains

[70] ANSYS Inc, "Unleashing the full power of GPUs for ansys fluent software, part 3," Dec. 2024. [Online]. Available: https://www.ansys.com/blog/unleashing-full-power-gpus-ansys-fluent-software-part-3

[71] G. McCafferty, S. Jiang, and Y. Yang, "Chemical warehouse explodes in China," Apr. 2016. [Online]. Available: https://www.cnn.com/2016/04/22/asia/china-chemical-warehouse-explosion/index.html

[72] Federal Aviation Administration, "Lithium Battery Incidents | Federal Aviation Administration," 2024. [Online]. Available: https://www.faa.gov/hazmat/resources/lithium_batteries/incidents

[73] Y. Min-sik and C. Jeong-yoon, “Deadly fire ravages battery plant,” Jun. 2024, section: Social affairs. [Online]. Available: https://www.koreaherald.com/view.php?ud=20240624050742

[74] ICI Radio-Canada, “Risque d’incendie des batteries au lithium : tous les services d’incendie s’inquiètent,” Sep 2024, publisher: Radio-Canada.ca. [Online]. Available: https://ici.radio-canada.ca/nouvelle/2108292/batteries-lithium-feu-transport-entreposage

APPENDIX A LIST OF RECENT ACCIDENTS CAUSED BY LI-ION CELLS

Table A.1 List of different types of accidents caused by Li-ion cells over recent years

Incident date	Incident type	Causes
May 2016	Explosion of a Li-ion cell storage centre in China [71]	Thermal runaway and auto-ignition of 100% charged battery cells
August 2016	Explosion of a Samsung Note 7 phone [14]	Insufficient space between the internal components and the battery resulting in a short-circuit
January 2018	Fire in a Tesla S electric car in China [14]	Thermal runaway of the battery pack
August 2021	Thermal runaway of an iPad during a flight South Corea - San Francisco [72]	Thermal overheating of the internal battery when charging the tablet
May 2023	Overheating of a mobile phone that has fallen to the ground between two passenger seats on an aircraft [72]	Mechanical pressure on the damaged phone causing internal short circuits in the battery
February 2024	Smoke and flames emitted by a cargo plane carrying Li-ion battery packs discovered by ground handling personnel before take-off [72]	Overheating and propagation of thermal runaway in the battery packs
June 2024	Smoke emission from a passenger's electronic cigarette during a flight *Delta Airlines* [72]	Overheating of the internal battery leading to the emission of gases and smoke
June 2024	Fire and smoke emission at an Li-ion battery factory in South Korea [73]	Thermal runaway in one cell then propagage to other cells in packs while workers were packaging them
September 2024	Fire and emission of white smoke from a container of Li-ion batteries near the port of Montreal [74]	Unknown cause - possible overheating of the batteries leading to thermal runaway according to experts

APPENDIX B REALIZABLE $k-\varepsilon$ - MODELLING THE TURBULENT VISCOSITY WITH THE CONSTANT C_μ

As the turbulent viscosity is defined in the *Methodology* part 3.1.1 as:

$$\mu_t = \overline{\rho} C_\mu \frac{\overline{k}^2}{\overline{\varepsilon}} \tag{B.1}$$

Compared to the standard $k-\varepsilon$ model, C_μ is not constant in the Realizable $k-\varepsilon$ model. It depends of the turbulence fields, the angular velocity and the mean rotation and strain rates [63] :

$$C_\mu = \frac{1}{A_0 + A_S \times \frac{kU^*}{\varepsilon}} \tag{B.2}$$

with

$$U^* \equiv \sqrt{\widetilde{\Omega_{ij}}\,\widetilde{\Omega_{ij}} + S_{ij}S_{ij}} \tag{B.3}$$

$$\widetilde{\Omega_{ij}} = \Omega_{ij} - 2\varepsilon_{ijk}\omega_k \tag{B.4}$$

$$\Omega_{ij} = \overline{\Omega_{ij}} - 2\varepsilon_{ijk}\omega_k \tag{B.5}$$

where $\overline{\Omega_{ij}}$ is the mean tensor of rotation observed in a moving reference frame with the angular velocity ω_k. A_0 and A_S are two constants defined as:

$$A_0 = 4.04 \text{ and } A_S = \sqrt{6}\cos(\phi) \tag{B.6}$$

where

$$\phi = \frac{1}{3}\cos\left(\sqrt{6}W\right)^{-1},\ W = \frac{S_{ij}S_{jk}S_{ki}}{\tilde{S}^3}, \tilde{S} = \sqrt{S_{ij}S_{ij}} \text{ with } S_{ij} = \frac{1}{2}\left(\frac{\partial \boldsymbol{u_i}}{\partial x_j}\frac{\partial \boldsymbol{u_j}}{\partial x_i}\right) \tag{B.7}$$

APPENDIX C VERIFICATION TESTS ABOUT 1D FLAME TEMPERATURE EVOLUTION ON CANTERA BETWEEN TWO MECHANISMS

For this comparison, two opposing jets of the gas mixture and the inert mixture are placed at low mass flow rates to allow sufficient time for the reactions to take place. Figure C.1 shows the evolution of temperature between the two opposing jets. This test allows a check to be made that there is no rise in temperature on contact with the two jets.

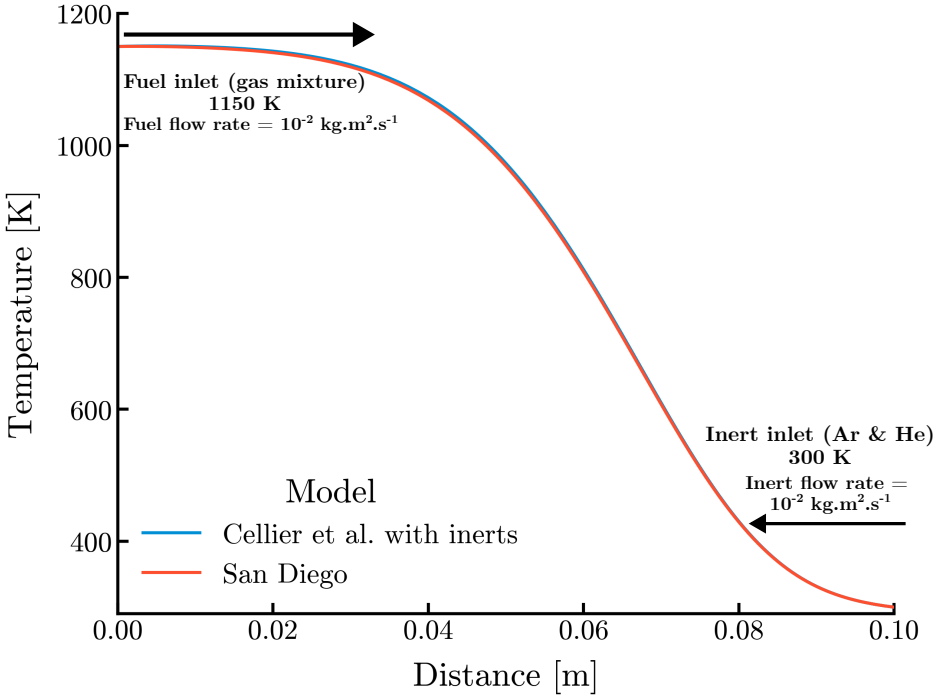

Figure C.1 Comparison of 1D flame temperature evolution on Cantera using the CounterFlowDiffusion flame module with two opposed streams of fuel and inert mixtures to compare the reduced mechanism modified with inert species and the San Diego mechanism

In this test, a similar configuration is used with two opposing jets, replacing the mixture of inert species with air (21% O_2 and 79% N_2 in mole fractions) and at ambient temperature and pressure (300 K, 1 atm). We also take a low outgassing rate for both jets as the configuration with the inert mixture. We compare the evolution of the flame temperature for the reduced mechanism taken from Cellier's study [45] and San Diego mechanism [55]. A rise in temperature is to be expected as the presence of oxygen in contact with the fuel gives rise to exothermic combustion reactions.

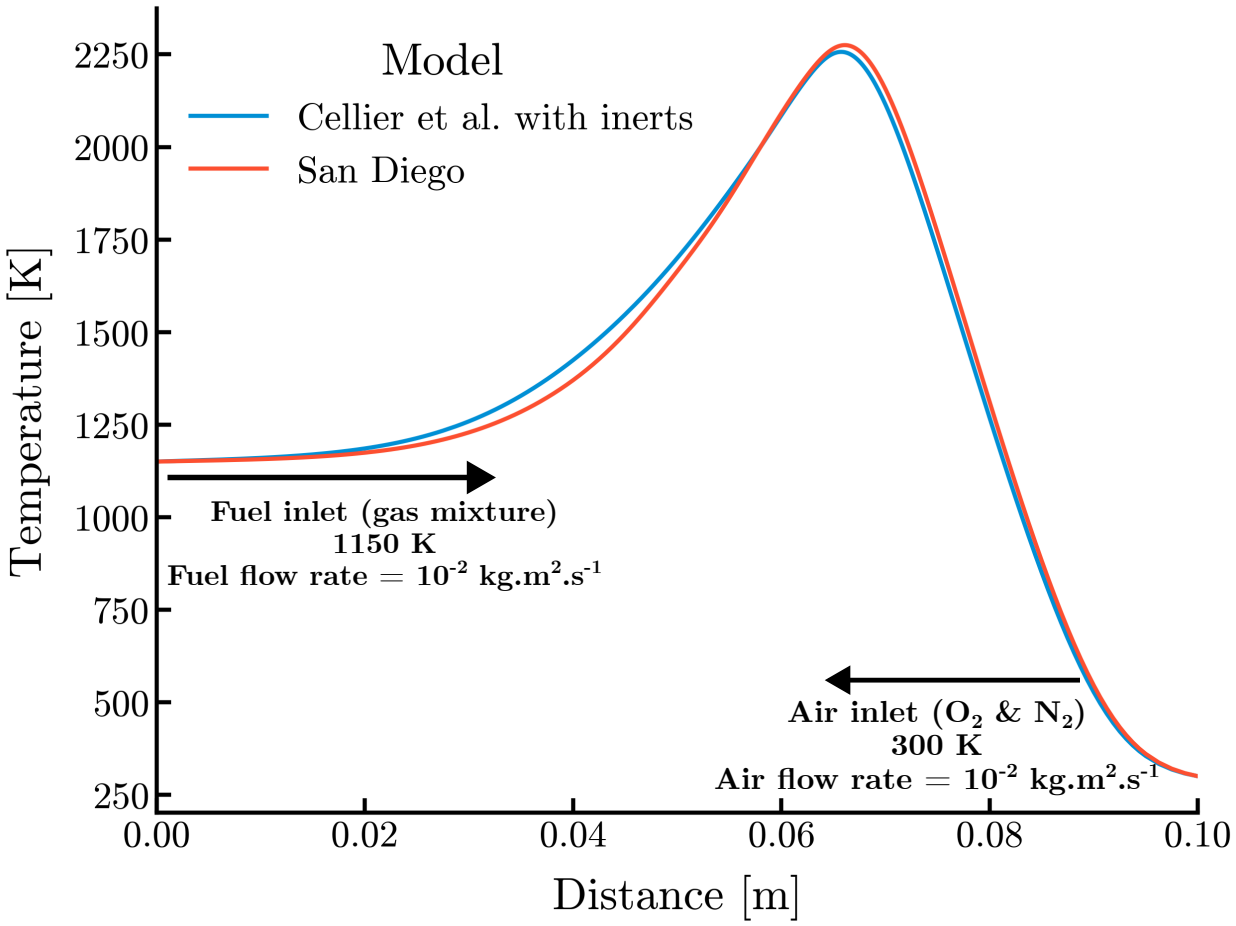

Figure C.2 Comparison of 1D flame temperature evolution on Cantera using the Counter-FlowDiffusion flame module with two opposed streams of fuel and air mixtures to compare the two mechanisms

APPENDIX D STUDY OF THE EVOLUTION OF INTERNAL PRESSURE AND OUTLET VELOCITY FOR AN INLET TEMPERATURE AT 950 K

A similar study to that proposed with the inlet temperature at 1150 K is made on the same mesh for the inlet temperature of the mixture at 950 K, maintaining the other boundary conditions of the model. Figure D.1 shows the temporal evolution of the internal pressure of the module and the average vent outlet velocity for T_{inlet} = 950 K for the EDC, NPC and PPC models.

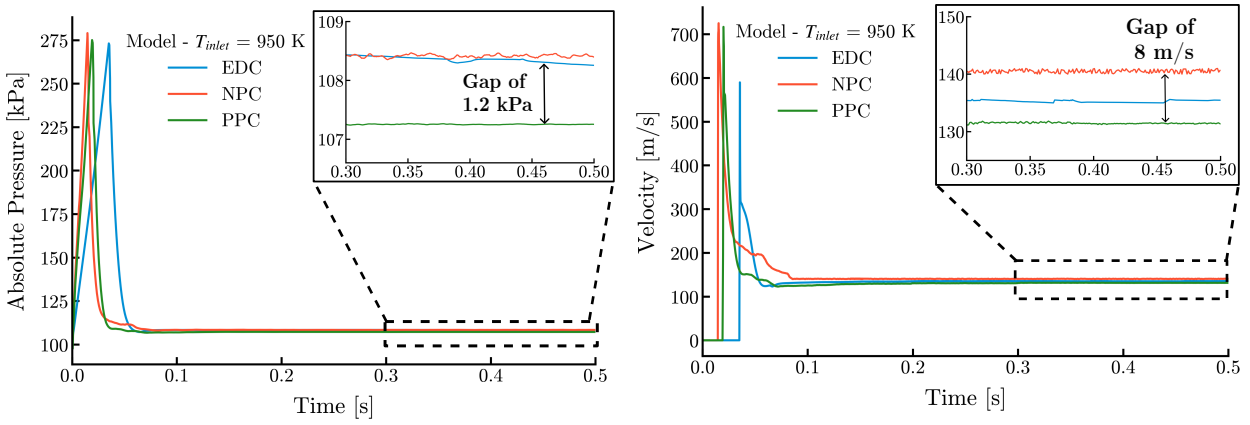

(a) Mean internal pressure in the module

(b) Mean vent outlet velocity

Figure D.1 Comparison of the temporal evolution of the mean internal pressure in the module for the inlet temperature at 950 K according to the three numerical models

In analogy with the inlet temperature at 1150 K, the evolution of the mean internal pressure of the module is similar for each of the models studied. The pressure profiles for the three models remain similar in the steady state regime ($t \geq 0.3$ s) with less than 1% variation between the curves. A shift in the internal pressure rise before venting is observed for the EDC model at this inlet temperature compared with the other two models, NPC and PPC. This can be explained by the presence of internal reactions in the module before venting for the EDC model. According to Figure D.1b, the mean vent outlet velocity profiles remain close for the three models. In a similar way to the internal pressure profiles, a shift in the peak outlet velocity is also visible due to the internal reactions for the EDC model compared to the other two models.

APPENDIX E AVERAGE AXIAL TEMPERATURE DATA FOR EACH MODEL STUDIED

For each numerical model, the mean axial temperature with its standard deviation is plot on the same graph. Axial temperature data are acquired every millisecond between $t = 0.5$ s and $t = 1$ s, i.e. 500 data files for each model.

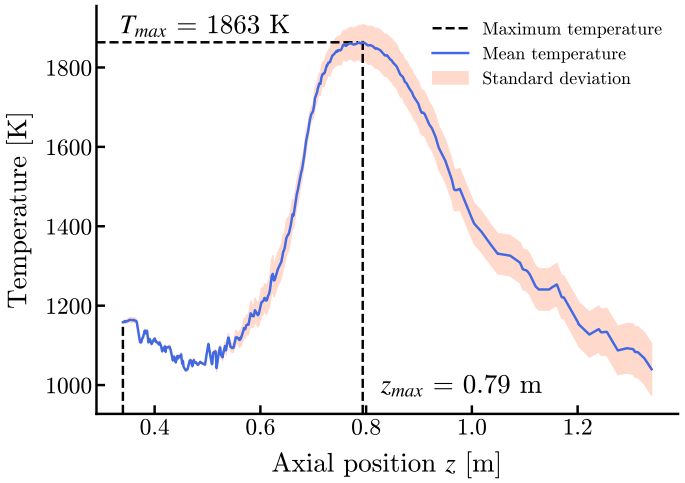

(a) Eddy Dissipation Concept

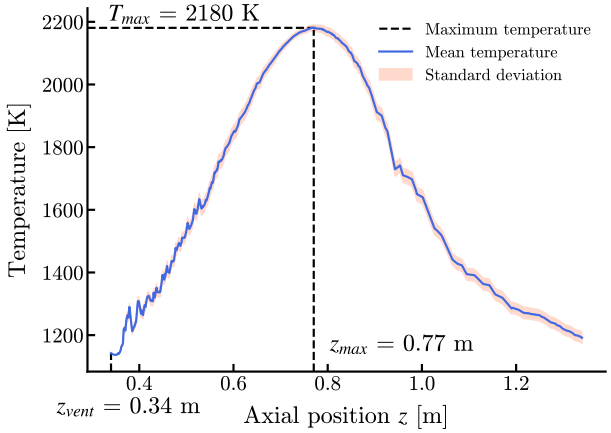

(b) Non Premixed Combustion

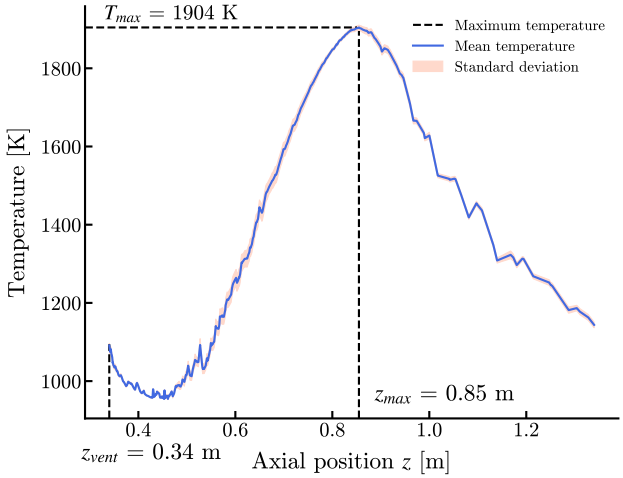

(c) Partially Premixed Combustion

Figure E.1 Evolution of mean axial temperature with associated standard deviation for each numerical model (EDC (**a**), NPC (**b**) and PPC (**c**))

Table E.1 Values of maximum mean axial temperatures and associated standard deviation for each model

Models	Maximum axial temperature average T_{max}	Standard deviation associated
EDC	1863.428 K	$\pm$ 44.686
NPC	2180.776 K	$\pm$ 10.017
PPC	1904.435 K	$\pm$ 6.227

APPENDIX F ANALYSIS OF HRR NEGATIVE VALUES

Firstly, a mesh and time step independence study is conducted for the three combustion models (EDC, NPC and PPC) with the 2023R2 version used for this thesis. It focuses mainly on the phase before the vent opens. A comparison between various solvers compatible with the EDC model is performed. Finally, the latest version of Fluent 2024R2 is compared with version 2023R2 for both combustion models.

Mesh and time step independence study with 2023R2 version

EDC model

The independence of the time-step size is investigated by reducing the time step on negative HRR values for the EDC model. The study is performed with the fine mesh at 1.35×10^6 elements over a simulation time equal to 1 ms, and three time steps are chosen: 10^{-4}, 10^{-5} s and 10^{-6} s. The inlet temperature is set at 1150 K and the module vent is initially closed to observe the HRR evolution before the venting phase. The temporal evolution of HRR for each time step is shown in Figure F.1a. Negative HRR values decrease as the time step is reduced and they are sensitive to the time step chosen.

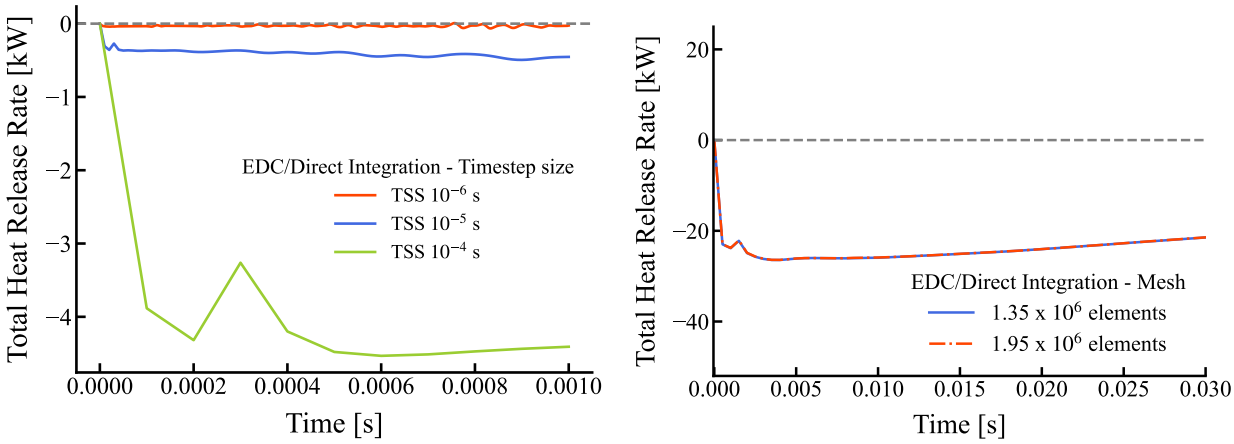

(a) Timestep size study (b) Mesh independence

Figure F.1 Study of the influence of time step and mesh size on negative HRR values for the EDC model

In addition, mesh independence is performed on fine meshes (1.35×10^6 and 1.95×10^6 elements) with a timestep $\Delta t = 10^{-4}$ s over a simulation time equal to 30 ms in Figure F.1b. Negative HRR values are not sensitive to the mesh refinement according to overlaid curves.

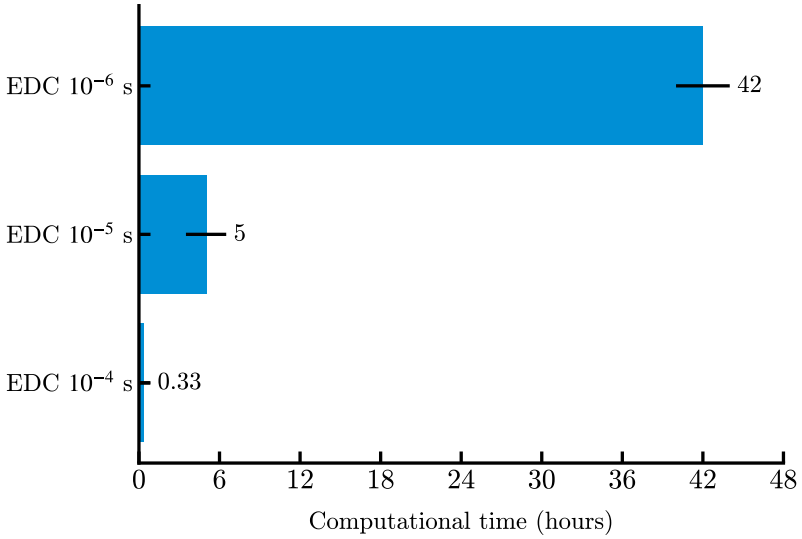

Figure F.2 Computational time for each selected time-step for the EDC model

Choosing a time step of 10^{-6} s reduces the negative values, however this is not viable in terms of computational cost for a simulation run over 1 ms as shown in the bar chart F.2. Furthermore, reducing the time step does not fully resolve the problem of the negative HRR values obtained in Figure F.1a, indicating that the reasons for these values are not clearly identified for the 2023R2 version.

NPC and PPC models

A similar study of time-step and mesh independence for both NPC and PPC models is performed by choosing the same previous parameters with the EDC model. According to Figures F.3 and F.4, the negative values are not sensitive to refined meshes. Concerning the influence of time step size (TSS), the negative HRR values become more visible as the time step decreases for both models.

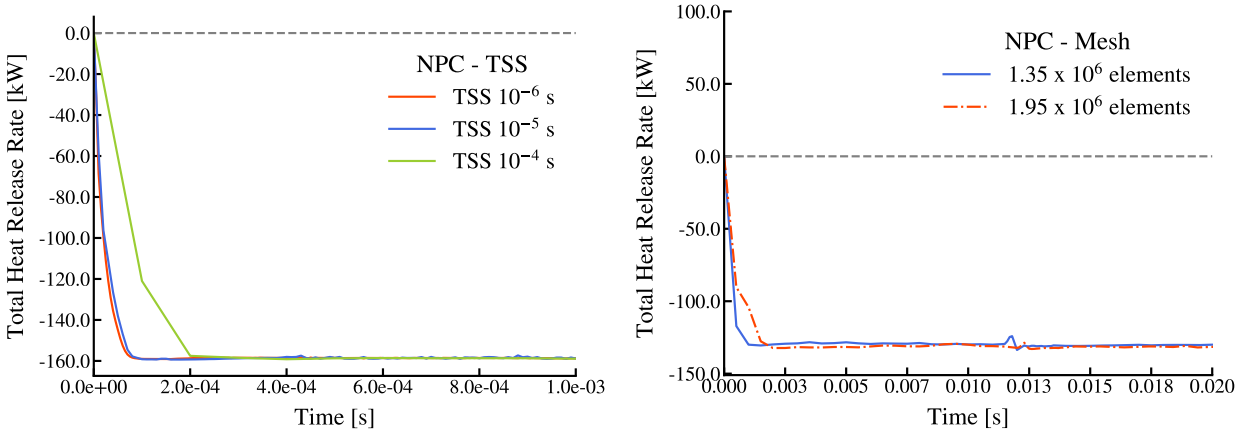

(a) Timestep size study (b) Mesh independence

Figure F.3 Study of the influence of time step and mesh size on negative HRR values for the NPC model

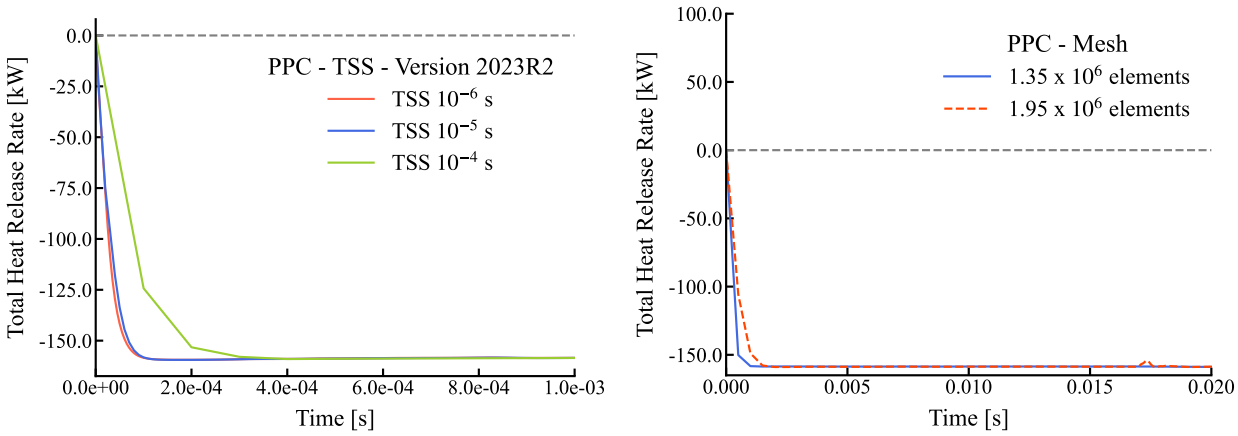

(a) Timestep size study (b) Mesh independence

Figure F.4 Study of the influence of time step and mesh size on negative HRR values for the PPC model

Comparison between solvers for EDC model

A comparison between different solvers handling reaction equation systems is conducted with EDC model with the 2023R2 version. Two main solvers for chemical reactions are available with this model: Stiff Chemistry and CHEMKIN solver.

The Stiff Chemistry Solver solves ODEs with implicit schemes to guarantee stability and accuracy in reaction rate calculations. When coupled with the EDC model, it first determines the characteristics of the turbulent field (mixing time, size of fine structures), then solves the kinetic equations within these zones, taking into account turbulence constraints.

The CHEMKIN solver solves chemical reaction equations based on kinetic constants and thermo-chemical parameters of the mechanism. This solver can be coupled with the ISAT (In-Situ Adaptative Tabulation) method to accelerate calculations by storing solutions for given chemical states in a table. When a new reaction state is encountered, the solver compares it with the stored values: if it has already been evaluated, it interpolates the solution, otherwise it calculates the solution and adds it to the table for later use. This technique reduces computational costs while maintaining good accuracy for reaction rates and heat release rate (HRR).

Figure F.5 shows the effect of the time step on the HRR values for the two solvers. For this study, an error tolerance of 10^{-20} is chosen, sufficiently low to reduce the propagation of numerical errors in solving systems of equations (ODE). Three time steps size (TSS) are chosen (10^{-4} s, 10^{-5} s and 10^{-6} s) for a simulation duration of 1 ms. Two configurations were tested: Stiff Chemistry with Direct integration, CHEMKIN with ISAT Table.

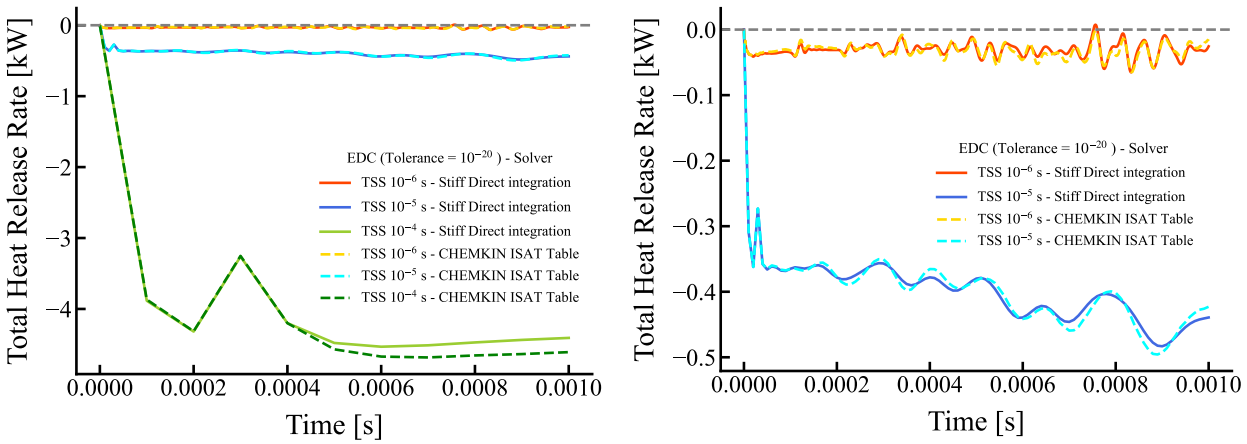

(a) Temporal evolution of HRR

(b) Zoom on curves with small time steps

Figure F.5 Temporal evolution of HRR using the CHEMKIN and Stiff Chemistry solvers for three time steps

Negative HRR values are observed for both solvers for the three time steps chosen. Although the tolerance error is small, the negative values are independent of the choice of solver and time step, as illustrated by the overlaid curves. In addition, Figure F.5b illustrates that the negative values are also obtained for the smallest time step at 1μs. This analysis indicates that a small time-step size does not fully resolve the presence of negative values.

Comparison between the two Fluent versions 2023R2 and 2024R2

A recent analysis of negative values was performed on the latest version of Fluent 2024R2. Two similar solver configurations with the EDC model are used: Stiff Chemistry with Direct Integration and CHEMKIN Solver with ISAT Table. This comparison between the two versions is conducted on the same mesh (1.35 $\times 10^6$ elements) with the time step fixed at 10^{-5} s. The inlet temperature is set at 1150 K and the module vent remains closed prior to the venting phase.

For each of the solvers tested, no negative HRR values were observed for the latest version 2024R2 compared with the version used for this thesis. This comparison illustrates that the issue of negative values has been corrected in the latest release as a result of the corrections made to the chemical solvers according to the latest ANSYS reports [69, 70].

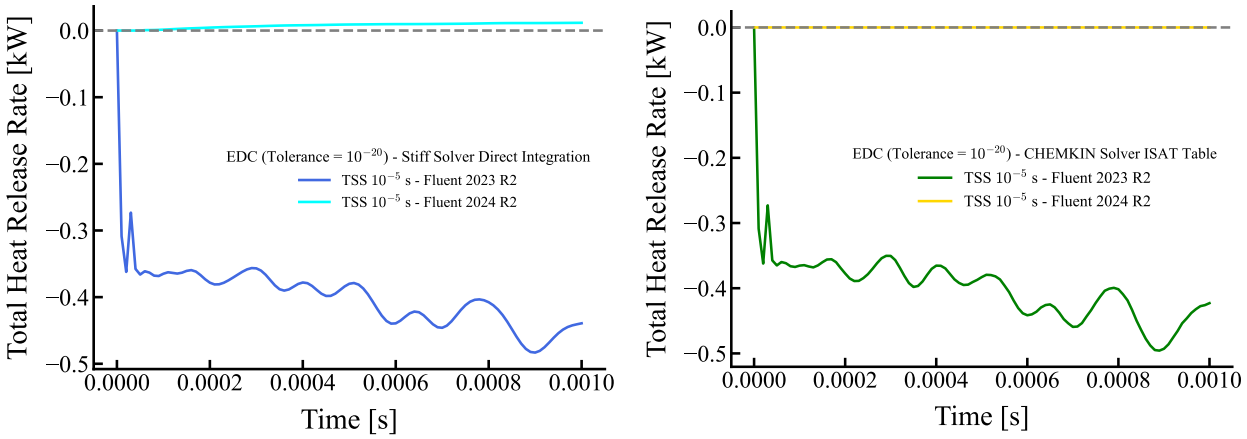

(a) HRR evolution with Stiff Chemistry solver (b) HRR evolution with CHEMKIN Solver

Figure F.6 Temporal evolution of HRR using the Stiff Chemistry (fig. **a**) and Chemkin (fig. **b**) solvers between two versions of Fluent (**2023**R2) and the recently release (**2024**R2)

A comparison between the two versions of Fluent was also conducted with the NPC and PPC models. Similar test conditions, such as a time step fixed at 10^{-5} s, were maintained for the analysis. Figures F.7 and F.8 show the temporal evolution of the HRR for the two versions over a simulation time of 1 ms. The new version of Fluent also shows negative HRR values, which indicates that the origin of the presence of these values cannot be clearly explained. Further studies with the next Fluent versions provided by Ansys will have to be made with both NPC and PPC models.

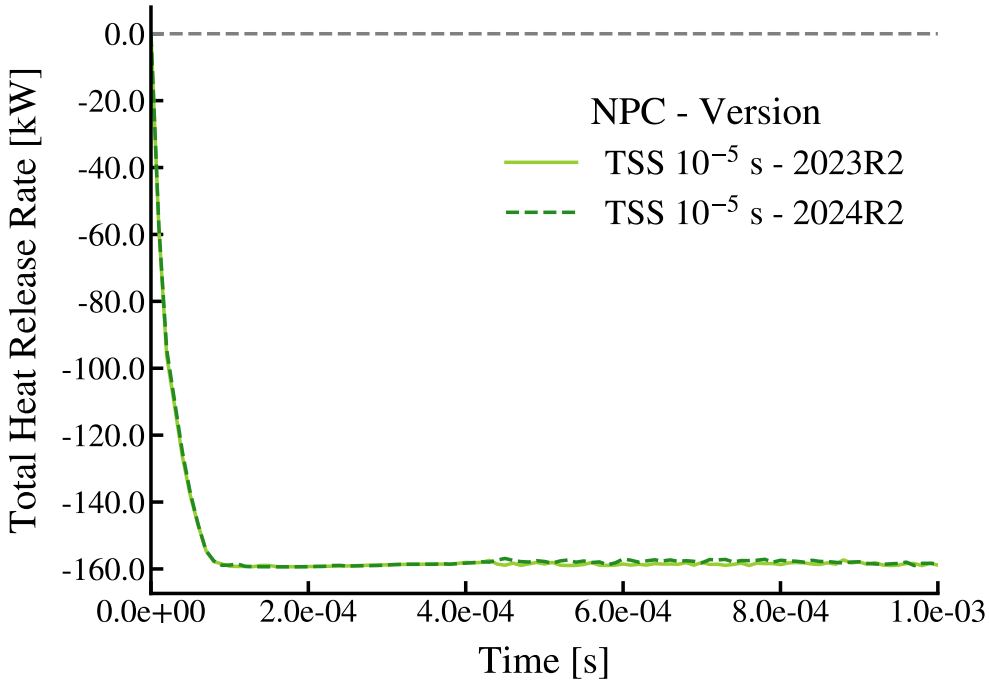

Figure F.7 Comparison of temporal evolution of HRR values for NPC model between two Fluent versions (**2023**R2 and **2024**R2)

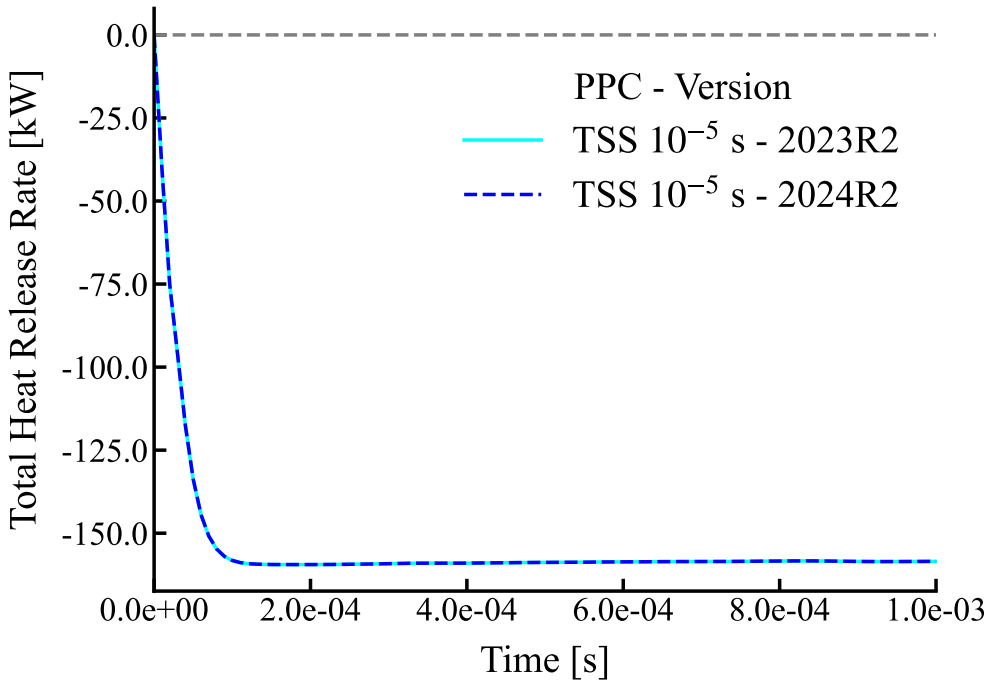

Figure F.8 Comparison of temporal evolution of HRR values for PPC model between two Fluent versions (**2023**R2 and **2024**R2)